Lateral Epitaxial Growth of Ge films on Si via a Vapor-Liquid-Solid Mechanism

Weizhen Wang

Department of Mining and Materials Engineering

Faculty of Engineering

McGill University

Montreal QC Canada

June 19, 2018

A thesis submitted to McGill University in partial fulfilment of the requirements of the degree of Doctor of Philosophy

Abstract

In recent years, there has been an increasing interest in developing alternative semiconductor materials since traditional Si-based devices have approached their physical limits. Given that Si has many advantages over other materials as substrate, the use of Si wafer is expected to continue. It is therefore important to grow high-quality semiconductor materials, e.g., thin films or nanowires, epitaxially on Si. The past thirty years have seen rapid advances in the field of heteroepitaxial Ge growth on Si because Ge-based devices can add functionality to Si chips and may be the key to enable next-generation computer systems or solar cells. The direct growth of Ge on Si, however, suffers from high-density threading dislocations that are formed during the growth process; these defects act as scattering and recombination centers that degrade the device performance.

In this thesis, a novel growth approach, metal-catalyzed, lateral epitaxial growth, is demonstrated to grow Ge films on Si with reduced threading dislocation density (TDD). In contrast to the traditional blanketed film growth on Si, this technique starts with a small crystal nucleation at a specific position on Si followed by a Ge lateral growth in the horizontal direction. It has been hypothesized that during the lateral growth process the lattice mismatch between Si and Ge can be accommodated by the extension of the preexisting misfit dislocations from the initial growth region or the nucleation of dislocations from the film sidewalls instead of generating additional threading dislocations from the film surface.

In this thesis, SEM and TEM were two primary characterization techniques to study the film morphologies, the growth process, and the relaxation mechanisms. One important finding was that the first nucleation areas of the films often have a higher Si concentration or may be thinner compared to the lateral overgrowth areas. This is important because such differences made it possible to figure out where the first growth occurred in electron microscopy. From here we could compare the dislocation morphologies in different areas. In plan-view and cross-sectional

TEM micrographs, high-density threading dislocations were found to be present in the initial growth areas while the lateral overgrowth areas demonstrated substantially reduced TDD or even defect-free areas. Moreover, the XRD results showed that the Ge films were almost fully relaxed with little Si incorporation. Given that the growth occurred at a low temperature, 375-500 ℃, we suggest the presence of new relaxation mechanism since the previous mechanism, dislocation nucleation and glide, would require a much higher temperature to fully relax the lattice mismatch strain. Therefore, we hypothesize that the strain induced by the lattice mismatch can be relaxed by extending the preexisting misfit dislocations and that lateral growth can "build in" dislocations as it grows.

Furthermore, this thesis proposes a simple model to describe the relation between the catalyst (Au) area and the area of the film in plan-view SEM; a film's size can thus be estimated by the size and shape of the Au catalyst. It has been found that a large Au catalyst can absorb more Ge due to its larger vapor-liquid interface, but more Ge is required to saturate the Au. This thesis also presents a study of the optimum growth condition of Ge lateral growth. The results show that high temperature and high GeH_4 partial pressure can boost the growth rate and thus increase the film size within a specified period of time. However, high growth rate can cause more uncatalyzed, vapor-solid Ge growth on Si as well. A relatively lower growth rate and a longer growth time are thus required to simultaneously increase the size of the films and reduce the uncatalyzed growth.

Sommaire

Au cours des dernières années il y a eu un intérêt croissant dans le développement de matériaux semi-conducteurs alternatifs dans la mesure où les dispositifs traditionnels à base de Si ont atteints leurs limites physiques. Le Si présentant de nombreux avantages par rapport aux autres matériaux en tant que substrat, l'utilisation de supports en Si devrait se poursuivre. Il est donc important de développer des matériaux semiconducteurs de haute qualité, comme par exemple des films minces ou des fils nanométriques, par épitaxie sur Si. Les trente dernières années ont vu des progrès importants dans le domaine de la croissance hétéro-épitaxiale du Ge sur Si, car les dispositifs basés sur le Ge peuvent ajouter une fonctionnalité aux puces au Si et peuvent être la clé pour développer la prochaine génération de systèmes informatiques ou de cellules solaires. Toutefois, la croissance directe de Ge sur le Si est impactée par une forte densité de dislocations vis qui se forment au cours du processus de croissance. Ces défauts agissent comme des centres de diffusion et de recombinaison qui dégradent les performances du dispositif.

Dans ce manuscrit, une nouvelle approche de croissance, la croissance épitaxiale latérale, catalysée par un métal, est démontrée pour la culture des films de Ge sur Si avec une densité de dislocations vis (DDV) réduite. Contrairement à la croissance traditionnelle du film recouvert de Si, cette technique débute par une légère nucléation cristalline à une position spécifique sur le Si suivie par la croissance latérale du Ge dans la direction horizontale. Il est supposé que durant le processus de croissance latérale, la différence entre les paramètres de maille du Si et du Ge peut être compensée par l'extension des dislocations préexistantes de la région de croissance initiale ou par la nucléation de dislocations des parois latérales du film au lieu de générer des dislocations vis supplémentaires à la surface du film.

Dans ce manuscrit, les techniques de caractérisation par microscopie électronique à balayage (MEB) et par transmission (MET) ont été utilisées pour étudier les morphologies du film, le processus de croissance et les mécanismes de relaxation. Il a été démontré que les premières

zones de nucléation des films avaient souvent une concentration de Si plus élevée ou pouvaient être plus minces par rapport aux zones de surcroissance latérale. Ces observations sont importantes car de telles différences ont permis de localiser, par microscopie électronique, la région où la croissance a débuté. À partir de cela, nous avons pu comparer les morphologies des dislocations dans différentes zones. Dans les images prises en MET en vue plan et en coupe, une forte densité de dislocations vis s'est avérée être présente dans les zones de croissance initiale alors que les zones de surcroissance latérale présentaient des zones de DDV sensiblement réduites ou même exemptes de défauts. De plus, les résultats obtenus par Diffraction des rayon X (DRX) ont montré que les films de Ge étaient presque complètement relaxés avec une faible incorporation de Si. Étant donné que la croissance s'est produite à basse température, 375-500 °C, nous suggérons la présence d'un nouveau mécanisme de relaxation puisque le mécanisme précédent, c'est-à-dire la nucléation et le glissement des dislocations, nécessiterait une température beaucoup plus élevée pour relaxer complètement l'élongation du réseau. Par conséquent, nous émettons l'hypothèse que la déformation induite par la différence de mailles peut être relâchée en étendant les dislocations préexistantes et que la croissance latérale peut "générer" des dislocations au fur et à mesure de sa croissance.

De plus, cette thèse propose un modèle simple pour décrire la relation entre la zone du catalyseur (Au) et la surface du film en vue plan par MEB ; la taille d'un film peut ainsi être estimée par la taille et la forme du catalyseur d'or. Il a été constaté qu'un catalyseur d'or de grande taille peut absorber plus de Ge en raison de sa plus grande interface vapeur-liquide, mais qu'une plus grande quantité de Ge est nécessaire pour saturer l'or. Cette thèse présente également une étude des conditions optimales pour la croissance latérale du Ge. Les résultats montrent qu'une température et une pression partielle élevées de GeH_4 peuvent augmenter le taux de croissance et ainsi augmenter la taille du film dans une période de temps spécifiée. Cependant, un taux de croissance élevé peut également provoquer une croissance vapeur-solide non catalysée de Ge sur le Si. Un taux de croissance relativement plus faible et un temps de croissance plus long sont donc nécessaires pour augmenter simultanément la taille des films et réduire la croissance non catalysée.

Acknowledgments

Firstly, I would like to thank my supervisor Prof. Nate Quitoriano for his continuous support for my PhD study and the research work, for his patience, motivation, and immense knowledge. His guidance helped me all the time during the doctorate study period.

Besides my advisor, I would like to sincerely thank all my research group colleagues, Jerome LeBoeuf, Alexandre Horth, Andrew O'Reilly, Jun Wang, Han Wang, and Moshen Keshavarz, for their important and useful discussion on research, support, and encouragement. My special thanks go to Jerome LeBoeuf, who designed and developed a micro-fabrication process for micro-crucible, and who trained me on the use of the equipment in the McGill Nanotools Microfab.

My sincere thanks also go to Prof. Oussama Moutanabbir, Samik Mukherjee, Simone Assali, and Nima Nateghi, who provided me an opportunity to join their team, and who allowed me to use their MOCVD system and other research facilities. Without their support, it would not be possible to carry out this research.

I also would thank the staff at the McGill Nanotools Microfab, Don Berry, John Li, Sasa Ristic, Zhao Lu, Peng Yang, Alireza Hajhosseini Mesgar, for their advice, support, and knowledge. I also would like to thank David Liu, Nicolas Brodusch, and Frédéric Voisard for their help in electron microscopy.

I would like to thank McGill University and NSERC for funding this project.

Last but not the least, I would like to thank my family: my parents, Zisheng Wang and Min Qin, for supporting me spiritually throughout writing this thesis and my life in general.

Table of Contents

List of Figures

List of Tables

List of Acronyms

AFM	**A**tomic **F**orce **M**icroscopy
BSE	**B**ack**s**cattered **E**lectrons
CMOS	**C**omplementary **M**etal-**O**xide-**S**emiconductor
CMP	**C**hemical **M**echanical **P**olishing
CVD	**C**hemical-**V**apor **D**eposition
EDS	**E**nergy **D**ispersive **S**pectroscopy
ELO	**E**pitaxial **L**ayer **O**vergrowth
FM	**F**rank-van der **M**erwe
HT	**H**igh **T**emperature
LT	**L**ow **T**emperature
MD	**M**isfit **D**islocation
MOSFET	**M**etal-**O**xide-**S**emiconductor **F**ield-**E**ffect **T**ransistor
PECVD	**P**lasma-**e**nhanced **C**hemical **V**apor **D**eposition
PR	**P**hoto**r**esist
PV	**P**hoto**v**oltaic
RIE	**R**eactive-**i**on **E**tching
SEM	**S**canning **E**lectron **M**icroscopy
SK	**S**transki-**K**rastanov
TEM	**T**ransmission **E**lectron **M**icroscopy
TD	**T**hreading **D**islocation
TDD	**T**hreading **D**islocation **D**ensity
XRD	**X**-**R**ay **D**iffraction
VLS	**V**apour-**L**iquid-**S**olid
VLSI	**V**ery-**L**arge-**S**cale **I**ntegration
VW	**V**olmer-**W**eber

Statement of Originality

To the best of my knowledge and belief, the thesis reports for the first time the theoretical and experimental results of lateral Ge film growths on Si using a vapor-liquid-solid mechanism. The original contributions are listed as following:

1. Previous studies have reported the lateral growth of Ge films on amorphous substrate by using epitaxial layer overgrowth or rapid-melting-crystallization. These techniques cannot be used to grow Ge directly on Si and sacrifice the epitaxial connection between the film and the underlying substrate. It has been reported that metal-catalyzed Ge nanowires can be grown laterally on Si to reduce the defect density. This thesis adapted this technique for the first time to laterally grow micron-scale Ge thin films directly on Si.
2. This thesis presents an unreported study with respect to the comparison of dislocation morphology within the first growth areas and the lateral overgrowth areas of the laterally grown Ge-on-Si films in plan-view and cross-sectional TEM. In addition, the composition and relaxation of the films were characterized by XRD. These results showed that some lateral overgrowth areas, which were found to be defect-free, were nearly pure Ge and fully relaxed. Based on these results, we hypothesized two relaxation mechanisms that enable low-TDD, laterally grown Ge on Si. These new concepts may contribute to high-quality, lattice-mismatched growth on a substrate.
3. This thesis presents an unreported study of the metal-catalyzed, lateral epitaxial thin-film growth process. In particular, a model is established in this thesis to determine the final film size. Additionally, growth variables, e.g., growth temperature, are studied to optimize the growth conditions. Based on these results, this thesis provides some original ideals to engineer the lateral thin-film growth on a substrate.

Contribution of Authors

This thesis was written entirely by Weizhen Wang and reviewed by Nathaniel Quitoriano. The results presented in this thesis (chapter 8, chapter 9, and chapter 10) will be published in scientific journals.

The micro-fabrication process of micro-crucible was designed and developed by Jerome LeBoeuf and Weizhen Wang. Weizhen Wang fabricated the samples, designed a high-density micro-crucible photomask, performed the CVD growth experiments under different growth conditions, prepared the TEM samples, did the SEM, TEM, XRD, AFM characterization, analyzed the results and wrote the paper. Nathaniel Quitoriano prepared FIB samples for TEM, provided guidance, and co-wrote the paper.

Chapter 1

Introduction

1.1. Motivation

Decades of research have been devoted to the integration of high-quality semiconductor materials. The technological impacts of integrating these materials together would lead to a paradigm shift in the design of semiconductor devices influencing technologies for solar cells, computer processors, cell phones, and telecommunications[1,2,3,4]. While there have been some advances in materials integration to overcome the difficulties (e.g. high-density dislocations) caused by lattice mismatch[5,6,7,8,9], especially with bonding and graded buffers[6,7], a high-quality, direct-growth approach to the integration of semiconductors has always been the technology of choice; it would lead to larger impacts since bonding and graded buffers have limitations[2].

An innovative way to grow a high-quality, lattice-mismatched film directly onto a substrate, is to start with one nucleation point and laterally grow the crystal over the substrate. In this way, instead of nucleating dislocations from the surface, which is done with both planar film growth and graded buffers, dislocations can be formed and propagated as the growth front moves laterally. Therefore, dislocations remain solely at the interface between the film and substrate and extend from one end of the film to the other, since dislocations must end at a surface. In this manner, the film will be relaxed by a network of misfit dislocations (MDs) without threading dislocations (TDs) intersecting the top, device, surface.

This innovative growth method, first demonstrated here, is made possible by selective, metal-catalyzed Chemical Vapor Deposition (CVD)[10,11,12]. This technique was originally used to grow germanium (Ge) nanowires laterally on Si or SiO_2. In this thesis, it was adapted to grow high-quality Ge films laterally on a Si substrate, since Ge films on Si have more industrial and proven applications, e.g. Ge photodetectors on Si for optical communication on chip. This project provides an opportunity to advance the understanding of new relaxation mechanisms for heteroepitaxial growth. More importantly, it may contribute to the fabrication of high-performance, low-cost, Ge-based devices.

1.2. Thesis Organization

The objective of this thesis is to develop a metal catalyzed, lateral epitaxial growth technique to grow high-quality Ge films on Si.

This thesis can be divided into three parts. The first part (chapter 1-4) provides a review of literature, which is necessary for the understanding of this thesis. Chapter 1 and Chapter 2 present the motivations of this thesis: it is of interest to develop a novel growth technique (lateral epitaxial growth in this thesis) to grow high-quality Ge thin films on a Si substrate. Chapter 3 gives a brief overview of the research on Ge heteroepitaxial growth on Si and introduces the basic concepts of lateral epitaxial growth. Chapter 4 reviews the research work with respect to metal-catalyzed, lateral epitaxial growth, which is a main growth technique in

this thesis.

The second part of this thesis (chapter 5-7) is concerned with the experimental process in this study. Chapter 5 describes the fabrication process of micro-crucible and introduces the relevant micro-fabrication techniques. Chapter 6 provides a detailed description of a Metal-Organic Chemical Vapor Deposition system (the growth reactor). Chapter 7 presents an introduction of the characterization techniques used in this study.

The third part of this thesis (chapter 8-11) presents the findings of this research work, focusing on the study of thin film morphology, growth variables, dislocation morphology, and thin film composition and relaxation (chapter 8-10). Finally, chapter 11 gives a conclusion of this study and identify the areas for further research.

Chapter 2

Ge Based Semiconductor Devices

2.1. Why Ge?

Over the past decades, silicon (Si) has served as the dominant material for semiconductor manufacturing because Si can be easily oxidized to form a stable SiO_2 insulating layer which has many applications in normal semiconductor processing, e.g. the gate material in Metal-Oxide-Semiconductor Field Effect Transistors (MOSFETs)[13]. Moreover, silicon has several advantages over other semiconductor materials, such as low cost and high mechanical strength. Today, the micro-fabrication technologies for Si-based semiconductor devices are well-established, e.g. the Si-based Complementary metal–oxide–semiconductor (CMOS) process,

and the Si-CMOS technology is the mainstream technique in very-large-scale integration (VLSI). However, it was predicted that the development of the Si semiconductors may slow down or even end soon since the Si technology is approaching its physical limits[14]. The miniaturization of Si MOSFETs, for example, has already met great challenges, e.g. tunneling and dielectric breakdown, especially after the channel length was reduced to below 45 nm[15]. According to Moore's law[16], the number of transistors on a chip is expected to double approximately every two years; this trend, however, may end in the near future. In addition, the developments of other Si devices, e.g. the traditional Si Photovoltaics (PVs), are also confronted with the bottleneck due to the intrinsic properties of Si. For instance, the theoretical upper limit of the efficiency of single-junction Si PVs was reported to be 31%[17]. Moreover, difficulties arise when an attempt was made to further reduce the manufacturing cost of Si based PVs. The total manufacturing costs of first-generation PVs depends largely on the single crystalline growth of the raw materials, namely, the Si substrates and the purification process of the raw silicon[18]. However, the technologies associated with the production of Si wafers have been highly developed and can hardly be improved to further reduce the cost. As a result, Si PVs currently cannot compete with the traditional grid systems in terms of cost per watt[19].

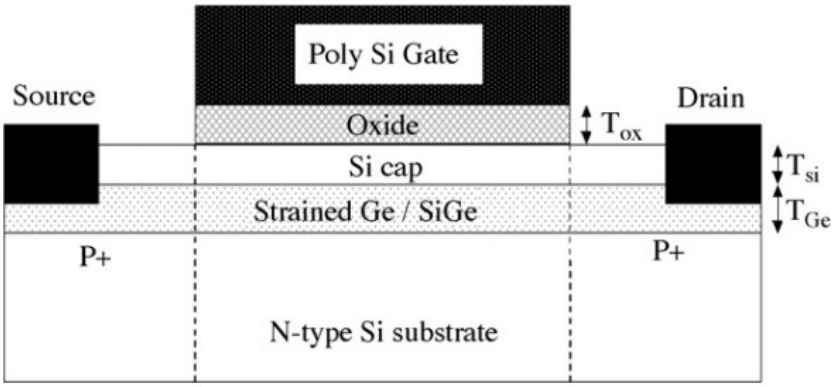

Figure 2-1. Schematic of high-performance Ge MOSFETs[15].

Since the development of the Si-based devices will go through a bottleneck period, there has been an increasing interest in using other semiconductor materials. Ge is one of the most promising alternatives that has many benefits. For example, Ge has higher electron and hole mobilities compared to Si which means that Ge is a potential channel material that can be used to fabricate high-performance MOSFETs[15,20](Figure 2-1). Since further increases in transistor

density will plateau, if further developments occur they could be through the use of high-mobility channel materials which offer increased performance, though perhaps not increased density. The recent developments of high permittivity (high-k) materials, which can passivate the surface of Ge to form high-k/Ge gate stacks, can contribute to achieving high-performance Ge-MOSFETs as well[21]. Moreover, Ge is commonly used to fabricate highly sensitive near-infrared detectors owning to its excellent short-wavelength absorption and fast responsivity[22]. What is more, Ge-based photodetector fabrication is compatible with the COMS technology, and the CMOS and waveguide integrations of Ge photodetectors have been successfully demonstrated[23,24]. Ge-on-Si photodetectors are believed to be an important component in Si photonics and play a key role in achieving the next-generation interconnects.

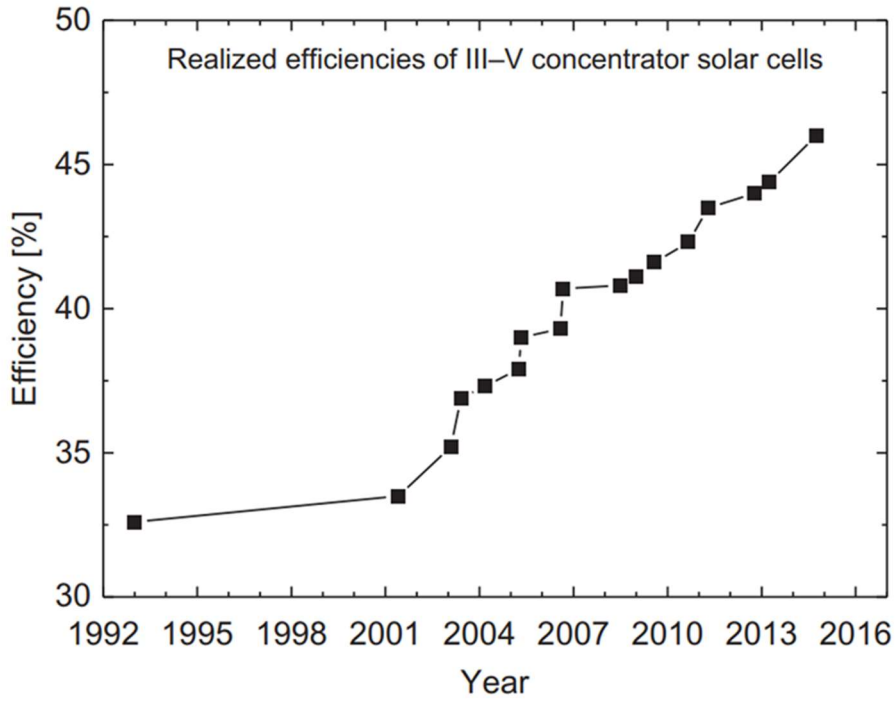

Figure 2-2. Efficiencies of III-V multijunction PVs[25].

Finally, Ge substrate provide an ideal platform for the fabrication of high-efficiency solar cells. Although the Ge band-gap (0.67eV) is far lower than the idea value (1.1eV) for single junction PVs, Ge substrates are lattice-matched with GaAs and thus can be used to grow high-quality GaAs films for the fabrication of Ge-GaAs based III-V Multi-junction PVs. In Figure 2-2, it shows that III-V multijunction concentrator solar cells can reach an efficiency of 45% and it may continue to increase.

2.2. Ge photodetector for on-chip optical interconnects

Silicon photonics is a discipline using silicon as an optical medium in a photonic system for a wide-range of applications, including optical interconnects, optoelectronic integration, biological and chemical sensors, etc[26].

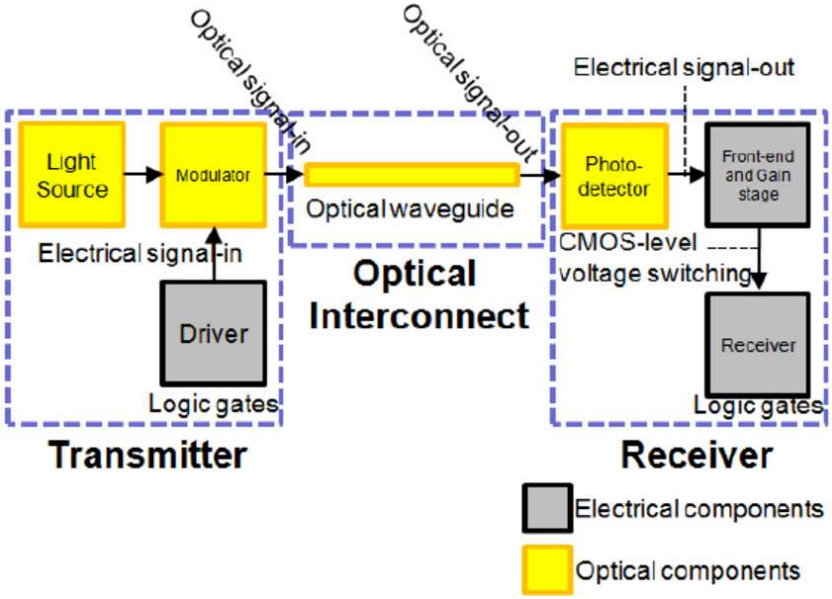

Figure 2-3. Schematic diagram of optical interconnects[27].

Today, optical interconnects is a promising area of semiconductor research due to its potential use in next-generation transmission technique, e.g., optical communication circuits can be used to manufacture extremely high-speed computers. On the other hand, the traditional electrical interconnects in integrated circuits has two major problems in practical use[28]. One is the large time delay as a result of electrical interconnects, which reduces the speed of computer systems. In addition, insulator layers must be deposited between multilayered electrical interconnections, which adds complexity to chip fabrication. Fortunately, there will no such issues involved with the use of optical interconnects. Figure 2-3 shows an example of on-chip optical interconnects. As can be seen from this figure, the optical signals are generated from the light source (e.g., multiwavelength laser sources) and transmit through an optical waveguide (e.g., Si optical fiber) and then are collected by the photodetector.

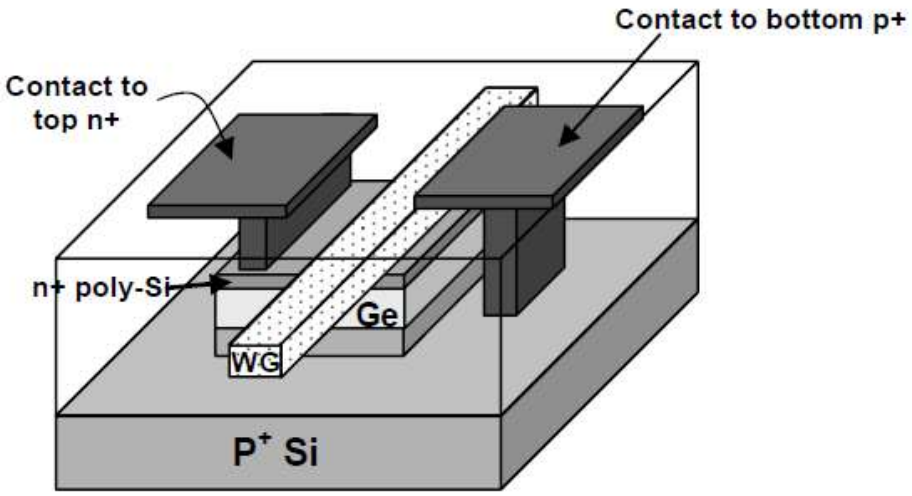

Figure 2-4. Schematic of a Ge photodetector[29].

In general, optical communication circuits are operated in the infrared because the transmission loss in silicon optical fiber is found to be minimized at the 1.3 μm and the 1.55 μm wavelength[30]. However, Si-based photodetectors are solely capable of detecting light with a wavelength from 190 nm to 1.1 μm because of the relatively large bandgap of Si[31] (the Si bandgap fails to absorb low-energy, infrared photons). On the other hand, as discussed above, Ge has shown high efficient photodetection capability within this wavelength range in terms of sensitivity and responsivity. Therefore, it is a widely held view that monolithic Ge-based photonics provides a promising option for the optical communications in Si CMOS-compatible circuitry[32]. People typically grow micron-scale or nanoscale Ge films on Si to fabricate Ge photodetectors for on-chip optical communications (Figure 2-4). However, this is not a straightforward step since the lattice mismatch between Si and Ge can introduce defects into the films that degrades the film quality. Recently, some growth techniques, e.g. graded buffers[32] and rapid melting growth[33], were reported to solve this problem and demonstrate the direct fabrication of Ge photodetector on Si; however, these technologies have their own limitations[2], e.g., graded buffer layers can be too thick. In this thesis, a metal-catalyzed, lateral epitaxial growth technique is used to grow high-quality, micron-sized Ge films on Si by using new relaxation mechanism. This technique has potential to reduce the defect density within the Ge-on-Si films and thus may contribute to the fabrication of high-performance Ge photodetector. More details with respect to the epitaxial growth of Ge on Si are presented in the next chapter.

Chapter 3

Heteroepitaxial Growth of Ge on Si

3.1. Challenges of Ge heteroepitaxial growth on Si

It has been shown that Ge has great potential in many fields, e.g. optoelectronics and integrated circuits, and may have great impact on the development of the third generation PVs. However, single-crystalline Ge wafers are known to be expensive and have poor mechanical properties, thus posing challenges for the practical use of Ge-based semiconductor devices. For example, Ge wafers dramatically increase the cost of the Ge-based multijunction PVs and make the PVs less competitive compared to the traditional power grid. To realize the wide applications of Ge devices, people propose to grow Ge thin films epitaxially on low-cost, high-strength Si

substrates. Nevertheless, direct, epitaxial growth of Ge on Si suffers from several drawbacks; the major one is the large lattice mismatch (4%) between Ge and Si that results in the generation of a high-density of dislocations within the Ge film[5]. The lattice misfit is equal to

$$f = \frac{a_s - a_o}{a_o},$$

where a_s and a_o represents for the lattice constants of Si and Ge respectively.

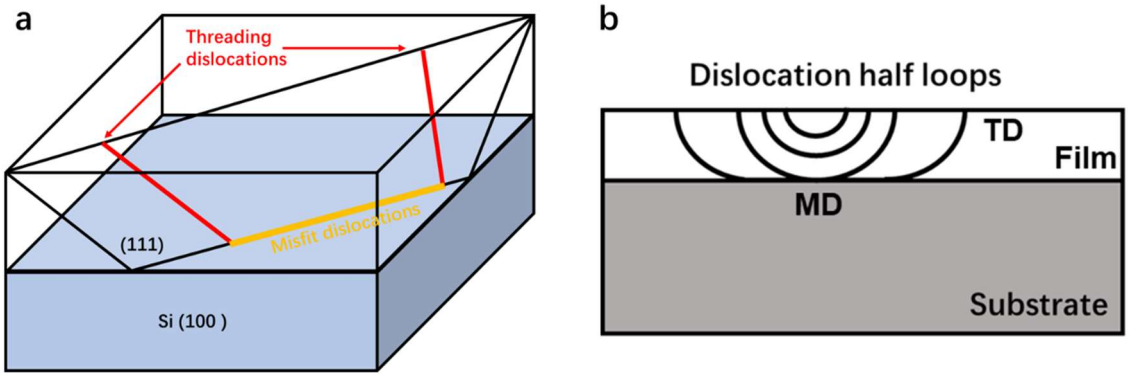

Figure 3-1. (a) Threading dislocation and misfit dislocation within a Ge film on Si substrate. (b) Schematic diagram of the relaxation mechanism strained epitaxial layer via the formation of dislocation loops from the surface.

As shown in Figure 3-1a, in general two types of dislocations, misfit dislocation (MD) and threading dislocation (TD), are present within the lattice-mismatched, epitaxial layer. Misfit dislocations reside at the substrate film interface and are necessary to relieve the lattice mismatch of the film. Threading dislocations thread up through the film lying on the (111) plane; they end on the film surface and are somewhat necessary since a dislocation must end at a free interface or grain boundary. Nevertheless, threading dislocations reduce the efficacy of electronic devices, since they act as the recombination and scattering centers for carriers and intercept the top device surface. On the other hand, misfit dislocations are less likely to affect the performance of devices because the top devices are far away from the interface. The misfit dislocations can be doped and then used solely as a conductive path[5].

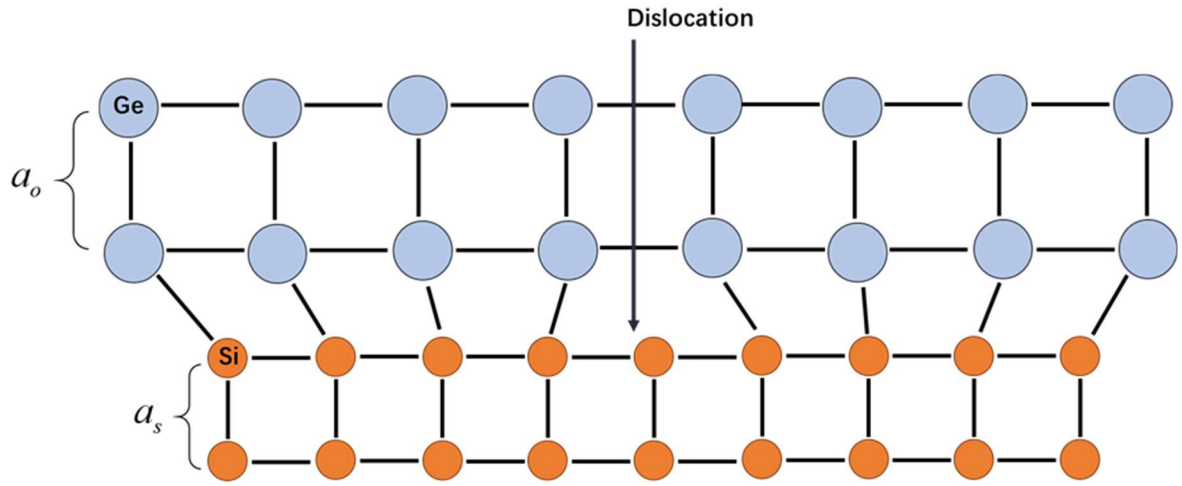

Figure 3-2. Schematic diagram of crystal lattices at the Si-Ge interface.

The main nucleation source for both misfit and threading dislocations is considered to be the generation of the surface half-loop dislocations[34,35](Figure 3-1b). In the initial stage of Ge growth on Si, the Ge film grows coherently on the underlying Si substrate (one-to-one correspondence between a Ge atom and a Si atom). As shown in Figure 3-2, the Ge lattice near the Si-Ge interface is deformed due to the elastic strain caused by the lattice mismatch. As the thickness of the Ge film increases, the elastic strain within the system increases. Beyond a critical thickness[36], the strain energy is large enough to overcome the energy barrier associated with nucleating dislocation loops from the film surface[5]. Afterwards, the dislocation loops grow and glide to the Si-Ge interface to relax the film (Figure 3-1b). More details regarding the theory of dislocations in strained epitaxial layer can be found in the paper written by Fitzgerald[5].

The lattice-mismatch between the substrate and the growth film (4% between Si and Ge) provides a large driving force to nucleate numerous surface half-loop dislocations. In most cases, high-density threading dislocations (10^6 - 10^9 cm^{-2}) are present within the Ge film grown epitaxially on a Si substrate[37]; this dislocation density is too high for most electrical devices and the most sensitive devices (minority carrier devices, like Bipolar junction transistors and lasers) require a threading dislocation density less than or equal to 10^6 cm^{-2} [38].

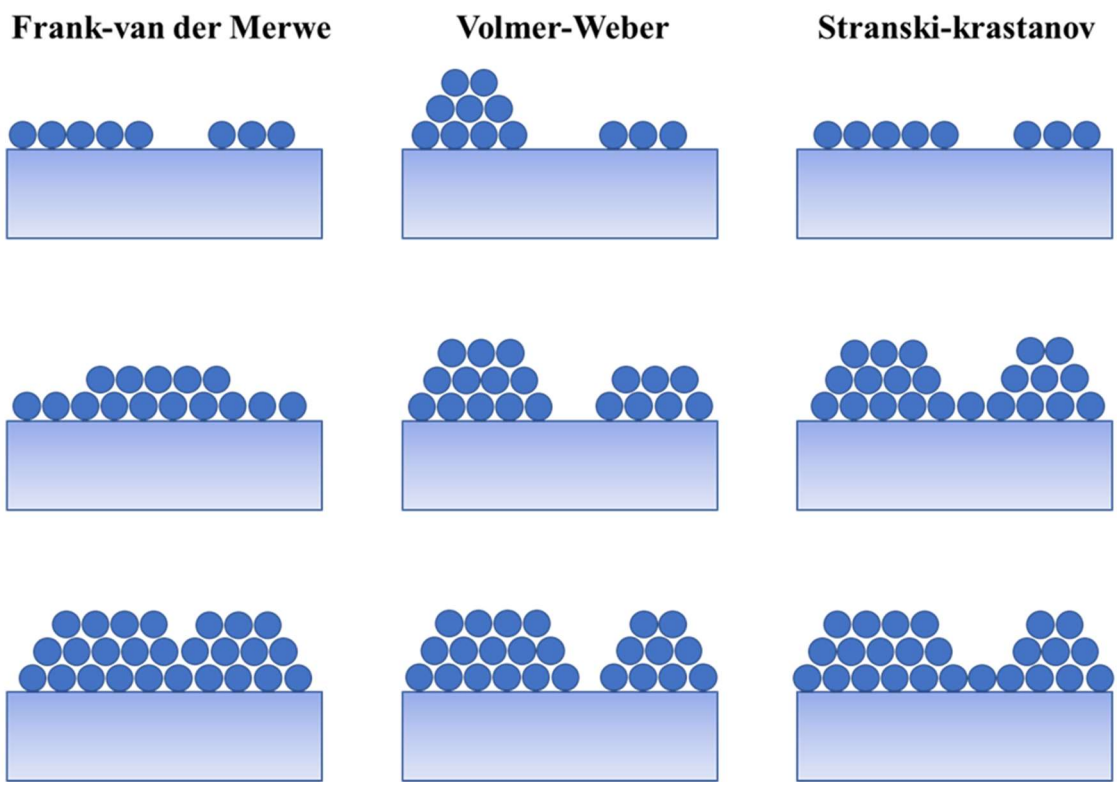

Figure 3-3. Frank-van der Merwe (FM), Volmer-Weber (VW), and Stranski-Krastinov (SK) growth mode.

Another challenge for the direct epitaxial growth of Ge on Si is the growth of Ge islands caused by the lattice strain near the Si-Ge interface[39]. As shown in Figure 3-3, there are three possible growth modes: Frank-van der Merwe (FM) growth, Volmer-Weber (VW) growth, and Stranski-Krastinov (SK) growth[40]. FM growth is a planar, thin-film growth mode and commonly desirable in the modern semiconductor industry. On the other hand, VW growth is a three-dimension growth mode through the formation of islands. In a lattice-matched system, either FM or VW growth is generally the growth mode depending on the surface energy of the substrate and the growth film. In contrast, in a lattice-mismatched system, a possible scenario is that layer-by-layer planar growth occurs in the beginning stages until the film thickness reaches a critical thickness. Then islands are formed to release the strain energy by the elastic deformation of lattices[41]. This is the process of SK growth mode shown in the Figure 3-3. It has been reported that the Ge-on-Si growth employs the SK growth mode with the formation of a metastable 3D cluster phase[42]. As a consequence, the Ge films grown on Si is expected to have high surface roughness due to the formation of islands and can be a problem for the subsequent device fabrication.

3.2. Ge grown directly on Si

An early attempt to grow high-quality (low-density TDs and flat surface) Ge thin-film directly on Si was reported by L.Colace *et al.*[43]. The growth process includes two steps. In the first step, a thin layer of Ge film (50 nm) was initially grown at a relatively low temperature (300 ℃) on Si in an ultrahigh vacuum CVD system. At 300 ℃, the Ge island growth (SK growth mode) could be largely suppressed since the formation of islands is a thermally activated process that requires high thermal energy (high temperature) for atomic diffusion. In this stage, it was suggested that the lattice mismatch between the Ge film and the underlying Si substrate was accommodated by misfit dislocations that nucleated from the dislocation half-loops[44]. In order to boost the growth rate and reduce the threading dislocation density, the growth temperature was then increased to 500 ℃ to grow Ge film over the initial Ge buffer layer. The study found that Ge thin-films with low surface roughness can be grown on Si by using this two-step process; these Ge films were then demonstrated to be used for the fabrication of high-performance Ge photodetector[43]. However, this approach failed to reduce the threading dislocation density to an acceptable level and it was shown that there were 10^{14} cm^{-3} recombination centers within the Ge film. Here, it is reasonable to assume that the density of recombination centers is approximately equal to threading dislocation density, since threading dislocation is the major source for the recombination centers.

In order to further reduce the threading dislocation density (TDD), cyclic thermal annealing was applied after the two-step growth proces[8]. Ge epilayers could be obtained with a threading-dislocation density of ~10^9 cm^{-3} from the two-step process. Then a cyclic heat-treatment between a high and a low annealing temperature (T_H/T_L) was performed to anneal the Ge-on-Si wafers. An average TDD of 2.3×10^7 cm^{-3} was achieved after 10 cycles of annealing between 900 and 780 ℃. In addition, it had been shown that in this process the reduction of threading dislocations depends weakly on the annealing time but depends strongly on the number of cycles as well as the annealing temperature. The mechanism behind this phenomenon is believed to be related to thermal-stress induced dislocation glide[8,45].

In addition, people have been working on further Ge on Si surface roughness reductions to enable the fabrication of nanoscale, Ge-based semiconductor devices. The effects of low temperature (LT) growth, high temperature (HT) growth and HT annealing on the Ge film surface roughness have been investigated and reported by Donghun Choi *et al.*[46]. Interestingly, Ge films grown at 350 ℃ on Si showed a smooth surface, but post-deposition annealing was found to degrade the surface roughness. On the other hand, Ge films grown by the two-step process (LT growth (350 ℃) in the beginning stage and then HT growth (600 ℃)) showed a rough surface. The roughness of these films, however, could be reduced by high temperature annealing. The authors suggested that at low temperature the diffusion of Ge atoms was inhibited, but the atoms were not stable and in a "high-energy" state. Then the post-deposition annealing transferred large amounts of heat into the system to activate the Ge atoms and induce the formation of Ge clusters on the surface. This process could reduce the total system energy and increase the surface roughness. In contrast, the Ge atoms were more stable in the films grown at high temperature. The post-deposition annealing boosted the diffusion of Ge atoms, but it was not likely to greatly modify the Ge surface morphology. Thus, the overall consequence was the improvement of the surface planarity. Despite the successful demonstrations of high-quality Ge films directly grown on Si, the wide application of this technology remains doubtful. The process itself is complex, consisting of two-step growth and a time-consuming and high thermal budget cyclic thermal annealing. Besides, although high-temperature annealing can vastly reduce threading dislocation density and improve surface roughness, it can also lead to significant Si out-diffusion and the formation of SiGe[47].

3.3. Graded buffers

Graded buffers were the first successful technique to reduce the threading dislocation density to a low level in a heterostructure[4]. In this approach, a low Ge content Si_xGe_{1-x} layer was first grown on Si followed by thin film layer-by-layer epitaxial growths. For the subsequent growths, the Ge content of each additional layer was slightly increased, e.g. 10 - 20 % Ge μm^{-1} along the normal direction of the Si substrate[7], until the composition reached the desirable value. Since the composition difference between a Si_xGe_{1-x} layer and the layer below it was small, it

was expected that the generation of additional threading dislocations could be suppressed due to the low lattice mismatch between the layers. Note that lattice mismatch is the main cause of the elastic strain field in a heterostructure and a large strain induces dislocation nucleation and therefore additional threading dislocations. As shown in Figure 3-4, during SiGe graded buffer growth, the lattice mismatch between layers were accommodated by the gliding of the preexisting dislocations and therefore the extension of misfit dislocations[48]. The dislocation glide is a thermal activated process; a high growth temperature (> 750 ℃), therefore, is necessary to entirely relax each Si_xGe_{1-x} layer.

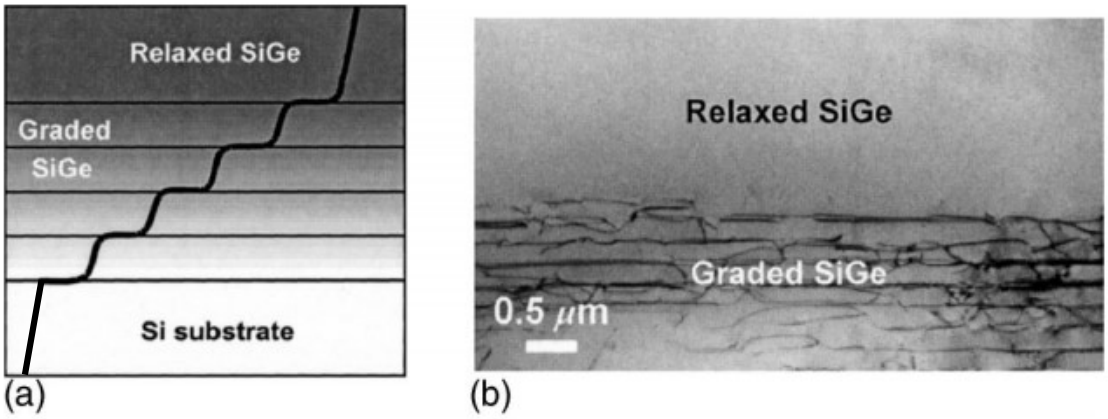

Figure 3-4. (a) Schematic and (b) Cross-sectional TEM micrograph of graded buffer layers[48].

The key point regarding the mechanism of how graded buffers can enable the high-quality growth of lattice-mismatched materials is that the lattice mismatch is largely relieved by the glide of the preexisting dislocations instead of nucleating new dislocation loops. In 1998, Currie *et al.* reported that a chemical-mechanical polishing (CMP) step could be introduced to graded buffers to improve the film quality[7]. It was found that dislocations glide is hindered by the deep trenches in the characteristic cross-hatch pattern. Since the glide of threading dislocation is the main relaxation mechanism for graded buffers, it is necessary to polish the surface to remove the trenches. It has been reported that fully relaxed Ge films could be grown with a threading dislocation density of 2.1×10^6 cm^{-2} by graded buffers along with the CMP step. The top, low-density TDs surface of Ge or SiGe in graded structure is promising for the fabrication of Ge-based semiconductors, e.g. Ge photodiodes[49]. However, this growth approach suffers from the fact that the graded layers may be excessively thick for the integration of the top devices[50]. It is a tough problem to solve because a low Ge-content increase at each new

layer in the graded buffer is generally required to inhibit the nucleation of additional dislocations, which will inevitably result in thick graded layers.

3.4. Selective Ge epitaxy

In 1989, Fitzgerald[37] investigated the impact of the growth area of lattice-mismatched epilayer on the density of the dislocations within the film. First, it is common sense that the total number of the fixed nucleation sources of dislocations is proportional to the size of the film. Besides, the glide distance of dislocations should not exceed the side length of the film. Therefore, it is expected that dislocation interactions and multiplications that may occur in the process of dislocation slip can be reduced in a small growth area. This is important because dislocation interactions and multiplications are two mechanisms to generate additional dislocations. Furthermore, in a small area, threading dislocations can easily glide to the edge of the film and then can be trapped and eliminated by the sidewalls. In brief, it was found that the number of threading dislocations and misfit dislocations were reduced in a small growth film. It might be attributed to the fact that less dislocation interaction occurred in a small area and threading dislocations were partially annihilated by the sidewall.

Using the similar principle and epitaxial necking, people have developed a technique to improve the crystal quality of the epitaxially grown Ge film on Si, termed as selective Ge epitaxy[9,51]. As shown in Figure 3-5a, a thermally grown SiO_2 film on Si was patterned by lithography and etching processes to predefine the positions (Si surface) to grow Ge. Then Ge was epitaxially grown on Si in a small, predefined window surrounded by SiO_2 sidewalls. It was reported that threading dislocations could be necked out by the SiO_2 sidewalls, and defect-free Ge was grown at the top of the epilayer. In 2007, a study of the mechanism behind the high aspect ratio epitaxial necking was reported[52]. It was found that the defect elimination by the selective Ge epitaxy was owning to the redirection of threading dislocations. During the growth process, threading dislocations were found to be parallel to the growth front normal. Within a high aspect ratio trench, threading dislocations were likely to encounter the (113) facets and then the (111) facets and move towards the sidewalls (Figure 3-5 b). In the end, the dislocations

were trapped and annihilated by the sidewalls. It was an interesting mechanism explaining the reduction of dislocation number in a high-aspect-ratio structure. Hyun-Yong Yu *et al.*[53,54,55] combined this technique with multi-step deposition/hydrogen-annealing cycles for the fabrication of high-performance p-Channel Ge MOSFET and Ge on Si photodiode.

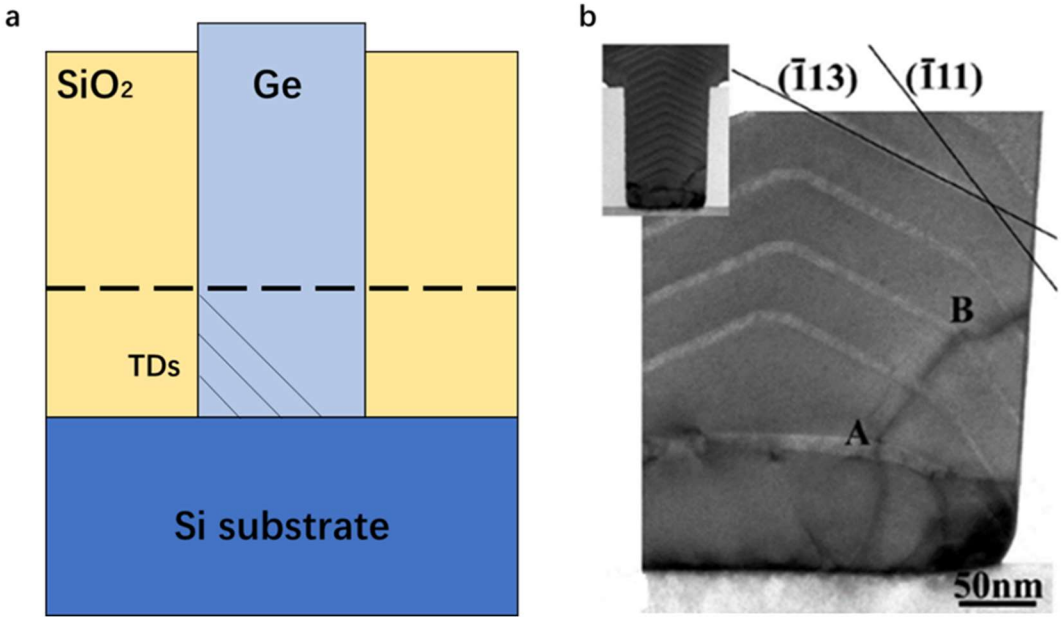

Figure 3-5. (a) Selective Ge epitaxy on Si/SiO_2. (b) Cross-sectional TEM micrographs showing the redirection of TDs[51].

3.5. Epitaxial Layer Overgrowth (ELO)

An early example of lateral growth was reported by B-Y. Tsaur *et al.*[56] to reduce the dislocation density within GaAs epilayer from 10^7 cm^{-2} to approximate 10^4 cm^{-2}. As illustrated in Figure 3-6, lateral overgrowth is a technique similar to selective growth of Ge on Si. However, the Ge selective growth on Si emphasizes on the trapping effects of the SiO_2 sidewalls. On the contrary, for the lateral overgrowth shown in the Figure 3-6, the SiO_2 film was only used as a mask to define the nucleation points on the GaAs substrate. GaAs was initially grown on the predefine areas and then grown laterally over the SiO_2 layer. The study found that the laterally overgrown GaAs films showed no threading dislocations except for the initial growth sections (the opening areas). However, the threading dislocations near the opening areas bent over quickly and did not propagate along the growth direction. It is also believed that this growth technique can be applied to other semiconductor materials to achieve low threading dislocation density within the films.

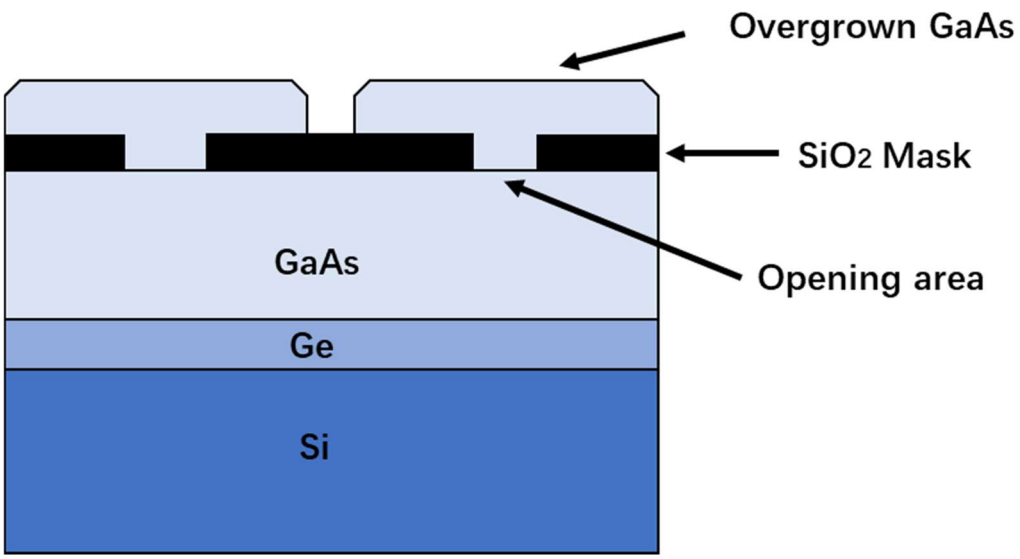

Figure 3-6. Lateral overgrowth of GaAs on a GaAs/Ge/Si substrate[56].

3.6. Ge lateral growth

In this thesis, epitaxial layer overgrowth is adapted to grow Ge laterally on Si instead of on an amorphous layer. This lateral growth process provides a pathway for investigating new relaxation mechanisms to accommodate the lattice mismatch between Si and Ge. In a lattice-mismatched, lateral growth process, it is thought that high-density threading dislocations may exist in the first growth section because the initial relaxation mechanism might be the nucleation of surface dislocation loops (Figure 3-7). Nevertheless, with the ongoing lateral growth, the misfit dislocations at the edge of the film might be elongated to release the strain at the interface (Figure 3-7). The new formation of dislocation loops is therefore suppressed since the strain is relaxed by the extension of existing misfit dislocations. In the end, the ratio of the number of threading dislocations to misfit dislocations is expected to decrease along with the lateral growth orientation. As discussed above, threading dislocations are the primary mechanism of device performance degradation in lattice-mismatched semiconductors. The new growth technique, lateral epitaxial growth, therefore has potential for growing high quality, lattice-mismatched thin films.

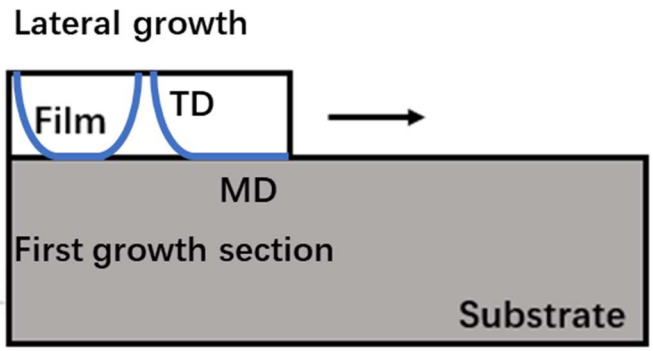

Figure 3-7. The extension of a misfit dislocation in a lateral growth process.

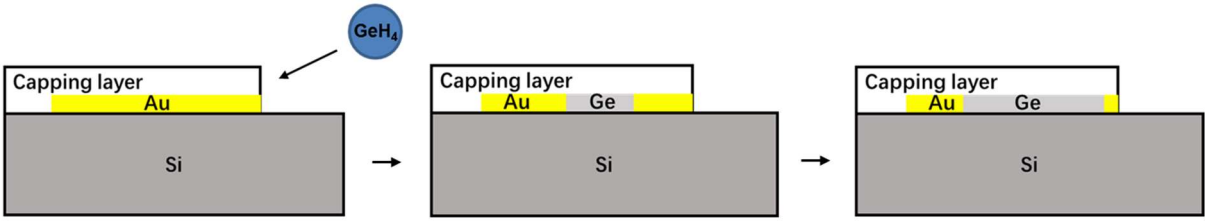

Figure 3-8. Schematic diagram of the metal catalyzed, lateral growth process.

In order to grow the films laterally in predetermined regions, an idea is to use a capping layer to prevent the vertical growth and a metal catalyst to define the nucleation point and engineer the growth direction. In this thesis, a micro-crucible structure[57] was designed for metal-catalyzed, lateral growth and the growth process is depicted in Figure 3-8. As we can see in this picture, the growth of the Ge thin film is confined to a channel underneath the capping layer; small Ge films are initially nucleated in the metal liquid and then grown laterally on Si within the channel. The metal-catalyzed growth method has been extensively used to synthesize semiconductor nanowires, termed as vapor-liquid-solid (VLS) growth[58]; the growth mechanism of VLS is discussed in the next section.

Chapter 4

Metal-Catalyzed, Lateral Epitaxial Growth

4.1. Chemical Vapor Deposition

Chemical Vapor Deposition (CVD) is the technique to form a thin film over a substrate by the chemical reactions of vapor precursors. CVD is extensively used in the semiconductor industry and is the basis of vapor-liquid-solid growth. The basic mechanism of CVD is demonstrated in Figure 4-1. It can be seen that a typical CVD process mainly involve gas reactions, the absorption and desorption of gases and multiple surface reactions. Here, the CVD growth of Ge based on the decomposition of germane ($GeH_4 \rightarrow Ge + 2H_2$) is used as an example to illustrate the growth process. First, the CVD precursor(s) (GeH_4) are transported by a carrier gas (e.g. H_2) to the reactor chamber. At an elevated temperature, the vapor precursors may chemically react in the gas phase to form intermediate reactants (GeH_3, GeH_2 or GeH). This is

followed by the adsorption of reactants on the target substrate surface. Afterwards, the reactants may decompose into atoms (Ge) which can diffuse to the growth sites to form a thin film on the substrate. In the end, the by-products are desorbed and transported away from the surface by the carrier gas.

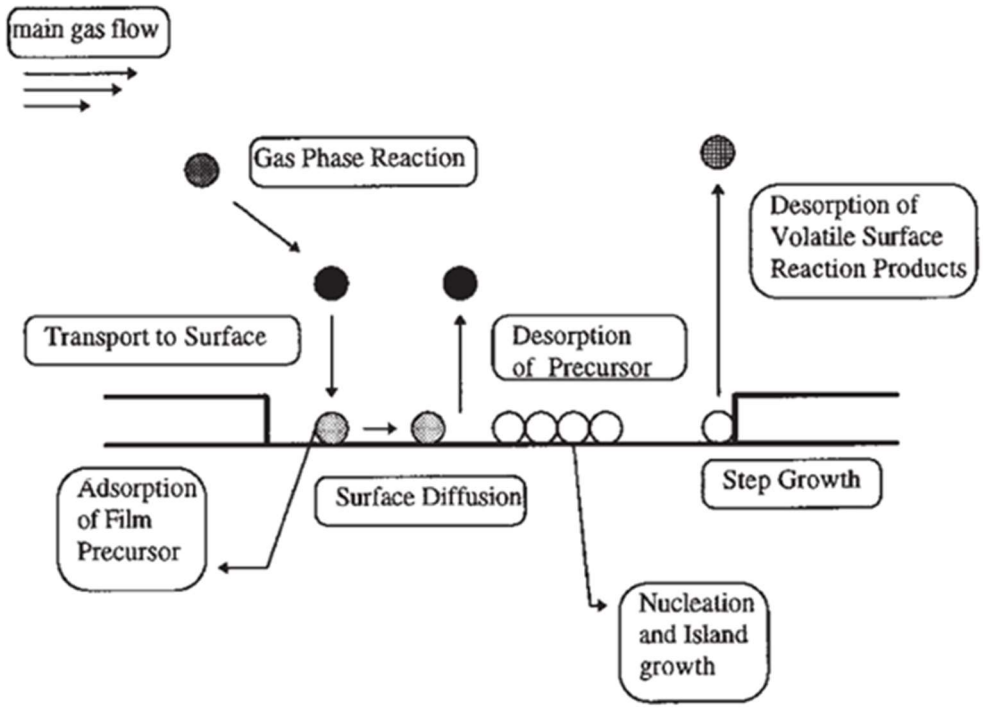

Figure 4-1. Schematic of CVD process[59].

In 1855, It was reported that tungsten was the earliest metal deposited by CVD[59]. Later in 1909, the first CVD growth of silicon was reported, and this growth method gained further popularity in the 1950s[59]. In the mid-1970s, CVD developed rapidly as a result of the large demand from the semiconductor industry, since CVD could be used to precisely control the uniformity, composition, purity and doping concentration of thin films. Despite its advantages over other thin film growth techniques, CVD suffers from several major drawbacks. First, gas precursors, essential for a CVD process, are generally expensive and toxic. Second, high temperatures are necessary for an epitaxial CVD growth which may cause damage to the temperature-sensitive substrates and increase thermal budget.

4.2. Vapor-Liquid-Solid Growth

4.2.1. Growth Mechanism and Kinetics studies of VLS

In 1963, Wagner and Ellis first described the unidirectional growth of semiconductors by using metal catalysts and discussed the related growth mechanism[58]. This type of growth was defined as vapor-liquid-solid (VLS) growth[58,60,61,62]. Figure 4-2 shows the growth of a silicon nanowire catalyzed by a gold droplet, demonstrating a typical example of VLS growth[63]. The Au droplet serves as a catalyst on Si substrate to determine the first nucleation site and guide the unidirectional growth of the Si nanowire. In Figure 4-2, the vapor precursors (SiH_4) tend to decompose at the surface of the liquid droplet rather than the Si substrate due to the catalytic ability of Au and the higher sticking coefficient of the Au/Si eutectic liquid. Once the droplet dissolves a sufficient amount of Si and reaches the supersaturation point, Si starts to precipitate at the liquid-solid interface in the form of a nanowire, dictated by the size of the Au catalyst. Then the system achieves a steady-state and the Si nanowire grows in a specific orientation.

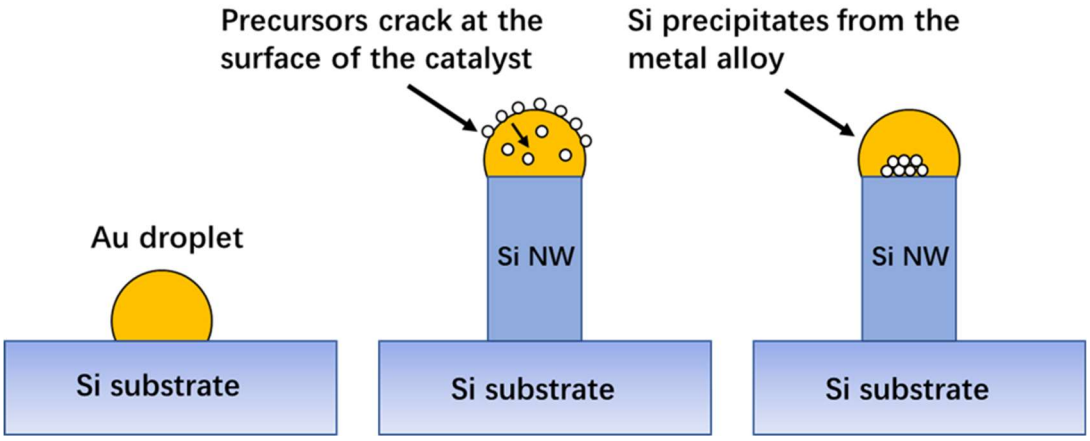

Figure 4-2. Schematic diagram of Si nanowire growth via VLS mechanism.

In 1971, Bootsma and Gassen studied the kinetics of the VLS growths of Si and Ge[64]. It was reported that the VLS growth rates of Si and Ge could be increased by increasing the substrate temperature and the vapor pressures of the hydride precursors (e.g. SiH_4 and GeH_4). The authors also confirmed that the growth rates of the catalyzed growths were hundreds times higher than that of noncatalyzed growth. Furthermore, it was suggested that the decomposition reactions of the precursors at the Vapor-Liquid surface was the most likely rate-limiting step

since the vapor pressure had impacts on the growth rate. Later, a further study on VLS growth mechanism was given by Givargizov[65,66]. These studies demonstrated that the growth rate of VLS growth decreased abruptly when the diameters of the semiconductor wires was reduced to a critical diameter at 0.1 μm because of the Gibbs-Thomson effect:

$$\Delta\mu = \Delta\mu_0 - \frac{4\Omega\alpha}{d},$$

where $\triangle\mu$ is the effective chemical potential difference of Si in vapor and solid, $\triangle\mu_0$ is the same chemical potential difference at plane boundary, d is the diameter of Si wire. As can be seen from the equation, when the diameter of the Si wire decreases, the chemical potential difference (the driving force for the VLS growth of Si wire) is reduced correspondingly which would lower the growth rate. However, a study by Nebol'sin *et al.*[67] reported that the Si VLS growth rate decreases with increasing Si whisker diameter. The authors suggested that a larger Si whisker diameter increases the Si equilibrium concentration in the liquid and thus provides a larger driving force to boost the growth rate. Afterwards, Kodambaka *et al.*[68] found that the growth rate was independent of the wire diameter, but proportional to the precursor partial pressure. They also proposed that during VLS growth the rate-limiting step is the irreversible dissociative adsorption of the vapor precursors on the liquid surface. In order to resolve the long-term ambiguity with respect to the dependence of nanowire diameter, Pinion *et al.*[69] performed measurements of Si nanowire growth rates over a range of temperatures, pressures, and diameters. They divided VLS growth into two regimes: (1) an incorporation-limited regime where the rate-limiting step was the precursor reactions at the V-L interface (Figure 4-3a), and (2) a crystallization-limited regime where the rate-limiting step was the deposition at L-S interface (Figure 4-3b). Moreover, it was found that the rate-limiting step depended on growth temperature and Si partial pressure. It was reported that in the incorporation-limited regime the growth rate is independent of the wire diameter, and in the crystallization-limited regime the growth rate depends on the wire diameter (positive correlation).

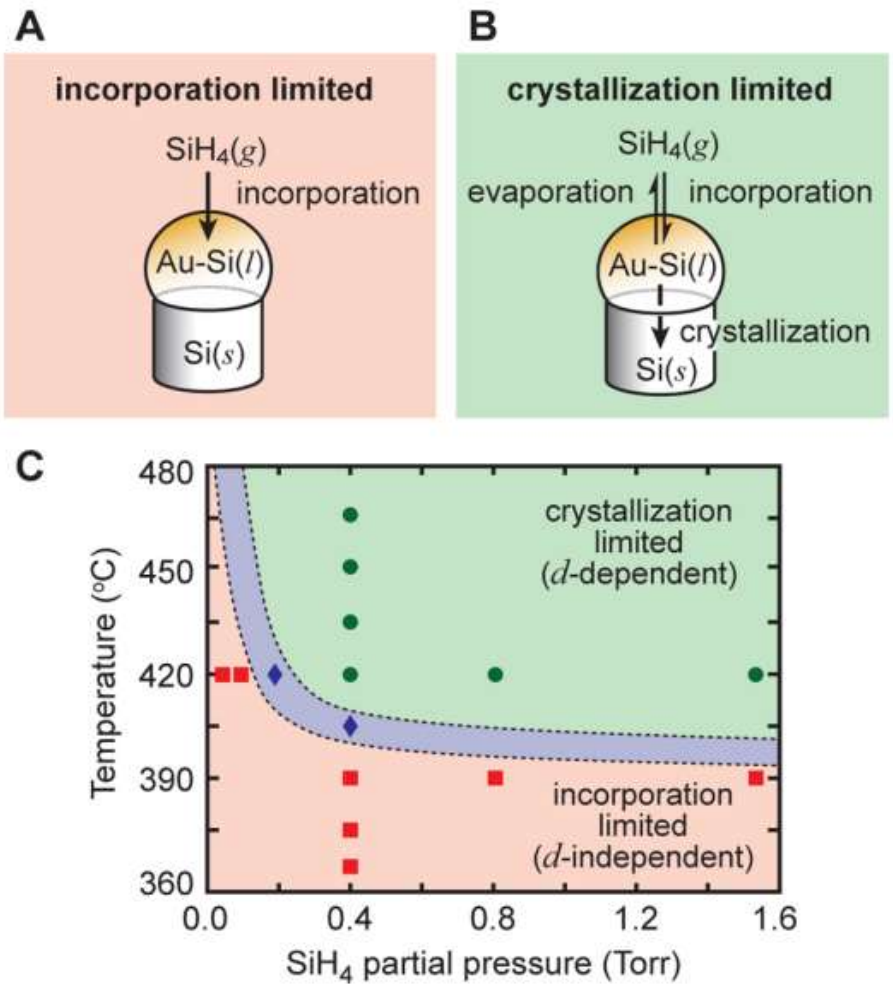

Figure 4-3. (a) Incorporation-limited where the rate-limiting step is the precursor reactions at the V-L interface. (b) Crystallization-limited where the rate-limiting step is the deposition at L-S interface. (c) The effects of temperature and Si partial pressure on the rate-limiting step[69].

In recent years, transmission electron microscopy was developed to study in situ VLS growth of nanowires; this technique presented a clearer picture of the growth process[70,71,72]. For the VLS growth of Si nanowires on SiO_2, it had been shown that Si tended to nucleate at the most energy-favorable sites (Figure 4-4a), e.g. the edge of the Au-Si alloy[71]. Once the first crystal seed was formed in the liquid (since it was grown on SiO_2, the first nucleated crystal was particularly hard to form which caused a large initial supersaturation), the nanowire grew quite fast because of that built up supersaturation and the corresponding increased chemical potential difference. However, after the Si concentration decreased to a near equilibrium value, the growth rate slowed (Figure 4-4b). Note that the growth rate was approximately proportional to the chemical potential difference (proportional to the extent of supersaturation) thus explaining the abrupt reduction in growth rate in Figure 4-4b.

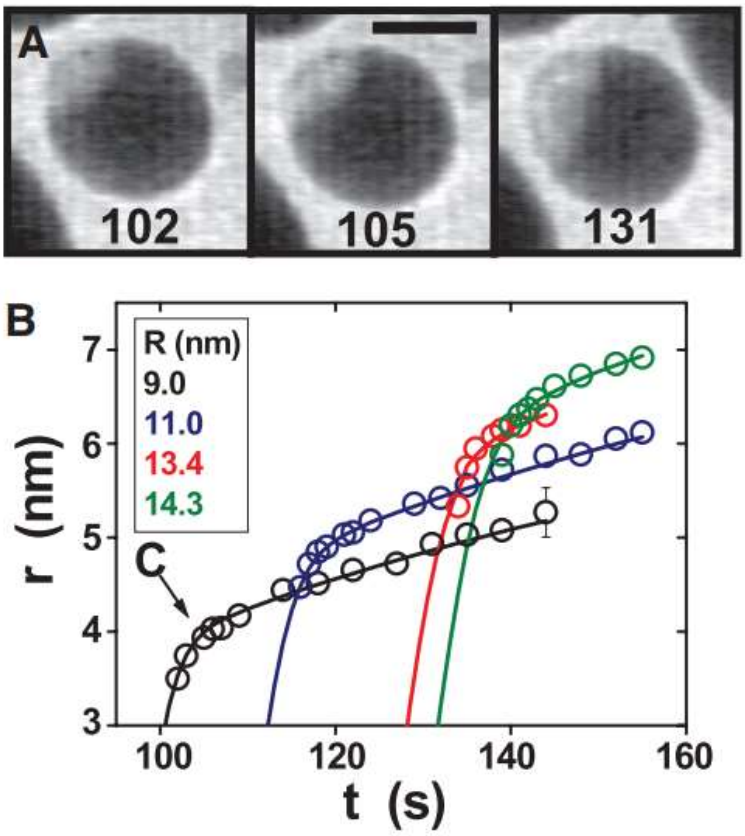

Figure 4-4. (a) TEM micrograph of an initial Si nucleation in a Au nanoparticle. Scale bar, 10 nm. (b) Sizes of several Si nuclei plotted versus growth time t for Au catalysts of different initial radius R[71].

Figure 4-4b also shows the incubation time to nucleate silicon. It was shown that the incubation time increased with the increasing size of Au droplets (the Au droplet size is approximately equal to the Si nuclei size). This is because more Si atoms are required to dissolve in a larger Au-Si droplet to reach the same supersaturation concentration to initiate the first nucleation. Kalache *et al.*[73] reported a study with respect to the incubation times in the VLS growths of Si nanowires and calculated the activation energy for the nucleation.

Over the past decades, the rapid development of VLS growth has attracted a great deal of interest. The growth mechanisms, growth techniques, alternative catalyst materials, etc., have been studied extensively and reviewed by Schmidt *et al.*[74].

4.2.2. VLS growth of Ge nanowires

The VLS growth of Ge resembles that of Si because Si and Ge are both group IV semiconductor

materials and have similar physical and chemical properties. One major difference is the growth temperature. Although the eutectic temperature of Au/Si is similar to that of Au/Ge (both ~ 360 ℃), the activation energies which are necessary to crack the vapor precursors are quite different. In general, the decomposition rate of Ge precursors, e.g. GeH_4, is higher than that of Si precursors. It is suggested that the CVD growth of Ge should be carried out at a relatively low temperature to better control the growth rate. The first growth of single-crystal Ge nanowire by VLS was reported in 2002[75]. In this study, it is interesting to note that the Ge nanowires could be grown at 275 ℃, a temperature substantially lower than the eutectic temperature. One key point of VLS growth is the formation of liquid metal alloy to catalyze and guide the growth. Since the Au-Si or Au-Si-Ge alloy is likely to solidify below the eutectic temperature, the successful demonstration of the VLS growth of Ge nanowires at 275 ℃ is surprising. Traditionally, it has been argued that the metal alloy catalyst remains liquid below the eutectic temperature due to the nano-size effect[76]. In addition, people also speculated that the nanowires were grown via a vapor-solid-solid mechanism at such low temperatures[77]. In 2007 Kodambaka *et al.*[78] analyzed the data from in situ microscopy and suggested that the metal alloy catalyst could either be liquid or solid below the eutectic temperature. What is more, no matter what state the catalyst is, Ge nanowires can be grown in both cases but at a different growth rate.

In 2004 Kamins *et al.*[79] investigated the structures of Ge nanowires over the temperature range from 320 °C to 380 °C (Figure 4-5). At higher growth temperatures (~ 380 °C), Ge nanowires grown by VLS generally demonstrated 6-fold faceted morphologies, which clearly shows the epitaxial connection between the nanowires and the underlying (111) Si substrate, while those grown at ~ 320 °C have circular cross sections, which is thought as a better morphology because it is more symmetrical. Outside the temperature range of 310 °C to 425 °C, the growth of Ge nanowires disappears. At a growth temperature higher than 425 °C, the decomposition rate of GeH_4 was excessively fast. Consequently, Ge was deposited on the surface of the Au catalyst before the Ge atoms diffused to the liquid-solid interface. Growth above 425 °C leads to three-dimensional growth around the catalysts rather than the one-dimensional nanowire growths. On the other hand, the growth rate decreased abruptly at a growth temperature below

310°C, probably due to the solidification of the Si/Au alloy.

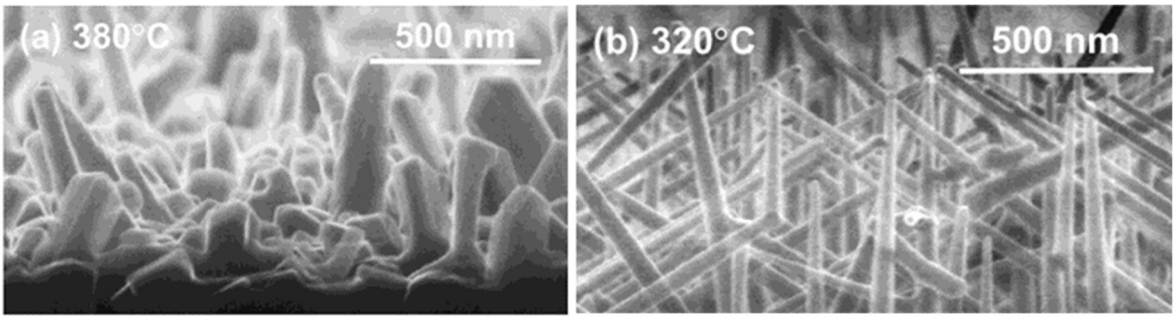

Figure 4-5. SEM micrographs of Ge nanowires grown on Si (001), showing (a) blocky structure at 380 °C and (b) well-formed structure at 320 °C[79].

In 2010, Cho and Kamin[80] reported a convenient procedure to in situ modify the morphologies of Ge nanowires by varying the growth temperature (Figure 4-6). This study was in agreement with Kamins's findings which showed that the vertical, catalyzed growth of Ge nanowires was dominated at lower growth temperature. On the other hand, at a high growth temperature, the lateral Ge growth on the sidewalls of the nanowires become more pronounced. As a result, the authors proposed to change the growth temperature to control the morphologies and the taper structures of the Ge nanowires.

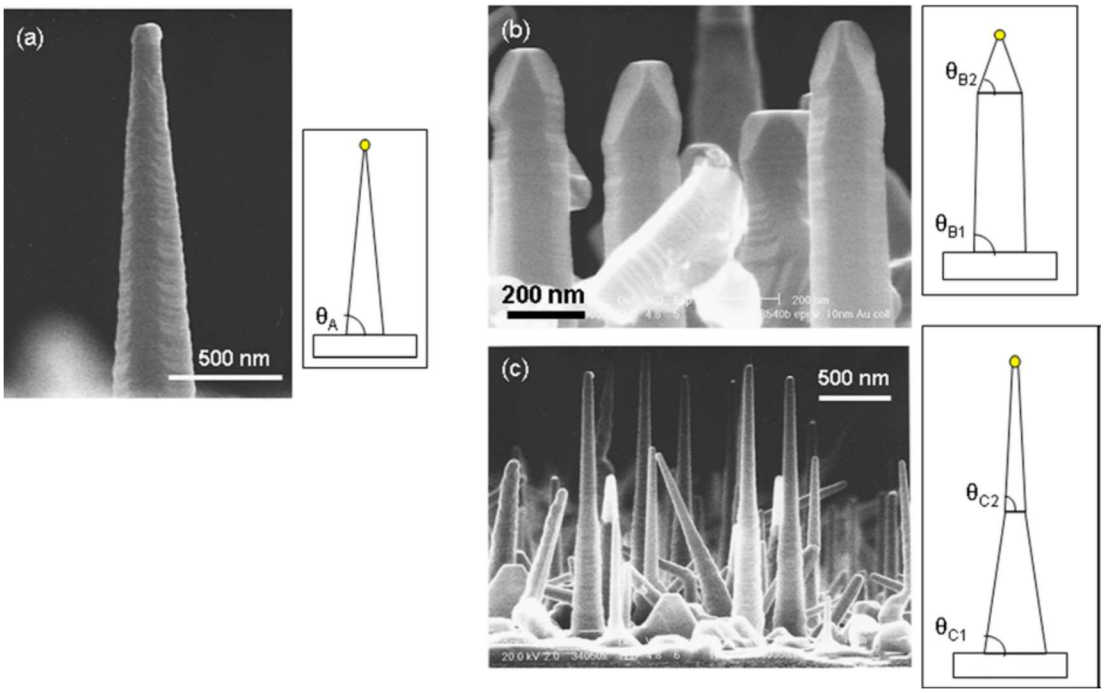

Figure 4-6. SEM micrographs and respective schematics of Ge nanowires grown at: (a) 380 °C, (b) 350 °C, then increasing to 400 °C, and (c) 395, 375, then 350 °C[80].

The past decade has seen the rapid development of the VLS growth of Ge on Si[81,82,83,84]. A variety of Ge nanocrystals of different shapes can be grown by varying the growth temperatures, pressures, gas compositions and catalysts. The VLS growth of Ge nanowires puts forward an exciting approach to fabricate novel Ge-based semiconductor devices. However, the precise control of nanowire growth, the integration with the modern CMOS process and the well-known deep-level property of Au poses remaining and significant challenges.

4.2.3. Lateral and guided VLS growth

As discussed previously, metal-catalyzed, guided growth offers a promising way of growing Ge laterally on Si because this technique may greatly reduce the threading dislocation density within the Ge film. One key component of this type of lateral growth is a special micro-structure (Figure 3-7), termed as micro-crucible, to control the growth in the horizontal direction. Previous studies have reported the utilization of nanoporous alumina templates to synthesis Si nanowires with uniform sizes[85,86]. As can be seen in Figure 4-7, the metal catalyst (Au) was deposited in the middle of the channels of the nanoporous alumina membrane. These Au nano particles were then used to catalyze the growth of Si nanowires within the channels, and the Si nanowires inherited the internal structure of the template. Even though the nanoporous alumina template was used to only define the diameters of nanowires, it is similar to the micro-crucible structure and can potentially be adapted to control the growth direction. It is an example showing how to engineer VLS growth by using templates.

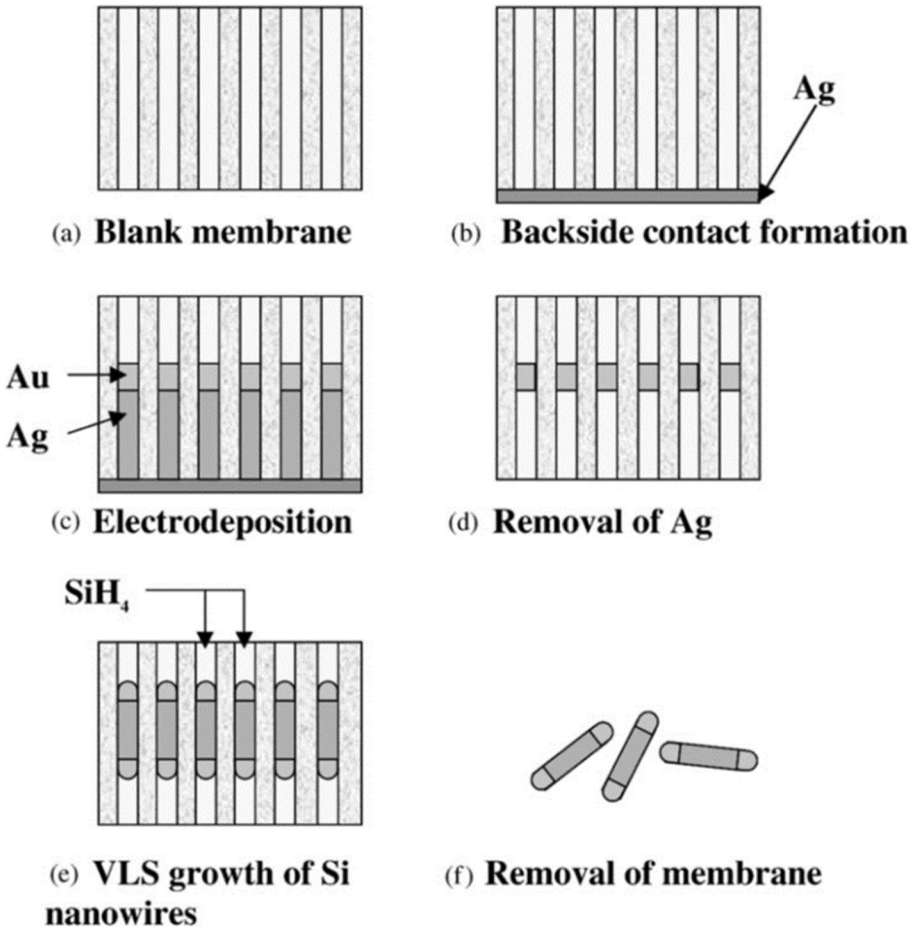

Figure 4-7. Schematic of the Si nanowire fabrication process. (a) Blank nanoporous membrane. (b) Deposition of thin Ag layer on the back of the membranes. (c) Electrodeposition of Au into the pores. (d) Chemical etching of the Ag. (e) Si nanowires growth within the pores. (f) Etching of the membrane[85].

In 2009, Lecestre *et al.* fabricated early micro-crucible structures to grow Si thin films laterally on an insulator surface without a crystal seed[87]. The fabrication process is demonstrated in Figure 4-8. First, Au catalysts and Ge sacrificial layers were defined and patterned on SiO_2 substrates via a standard lithography process. The metal layers formed the structure of the growth channels. Afterwards, conformal PECVD was performed to deposit Si*x*O*y*/Si*x*N*y* capping layers on the prepared substrates followed by a lithography and dry etching process to partially etch the capping layers. Note that parts of the Ge layers were exposed for etching. Then the substrates were dipped in a H_2O_2 solution to completely etch away the sacrificial Ge layers to from the channels. In the end, crystalline Si thin films of different sizes were grown inside the micro-crucibles by metal-catalyzed CVD.

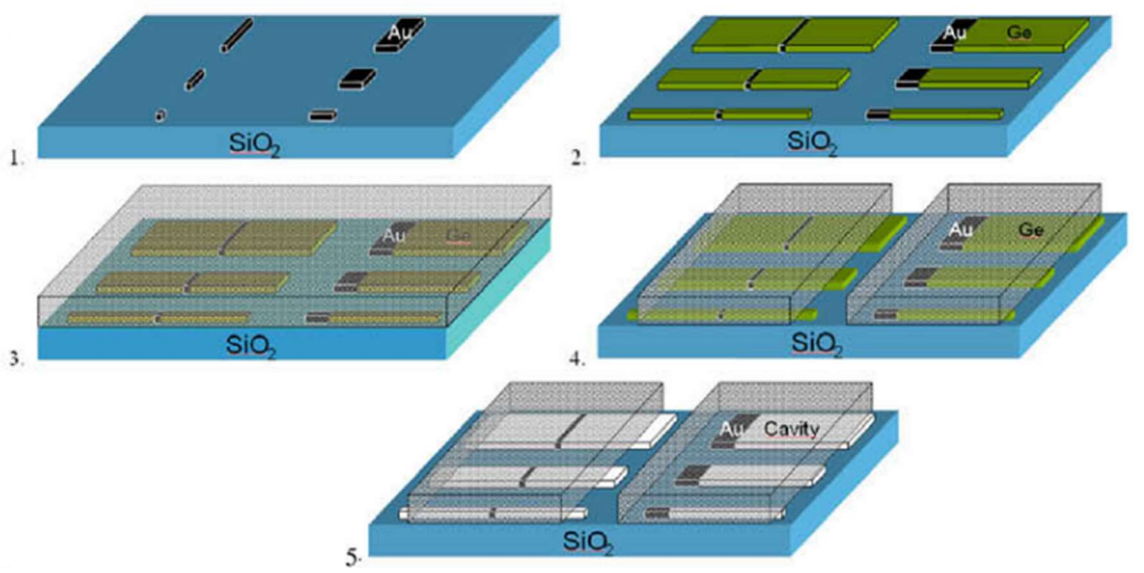

Figure 4-8. Fabrication process of early micro-crucible structures. (1) Selective deposition of Au catalysts on SiO_2. (2) Selective deposition of Ge on SiO_2 which are aligned to the Au catalysts. (3) PECVD of SixOy/SixNy capping layers. (4) Creating openings by lithography and RIE. (5) Etching of the Ge layers[87].

Later, the authors performed several characterization techniques (SEM, TEM and EBSD) to gain some insight into the laterally grown Si films on SiO_2. As demonstrated in Figure 4-9, it was found that the Si thin films could not entirely fill the channels that have a width larger than 1 μm. This is because a large Au catalyst tends to break into small pieces to catalyze the growth of Si thin films; larger Au catalyst is necessary to enable large thin film lateral growth since the sizes of the films are determined by the sizes of the catalysts. In addition, the authors observed the Au diffusion along the sidewalls of the channels. More importantly, TEM and EBSD results showed the existence of the single crystalline Si thin films with twins, demonstrating the possibility of growing single-crystalline Si films on an amorphous substrate at low temperature.

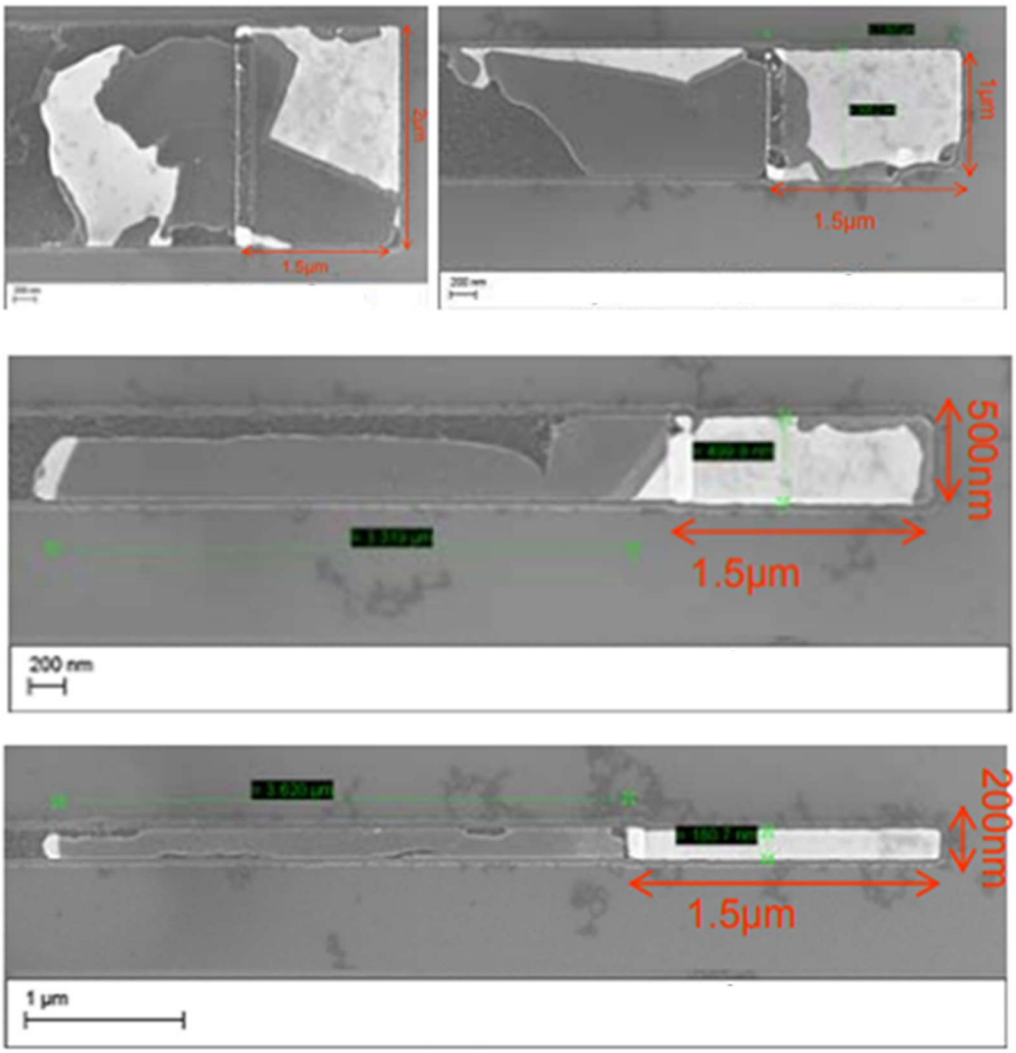

Figure 4-9. Plan-view SEM micrographs of the laterally grown Si films within channels of different widths (from 200nm to 2µm)[87].

In 2012, Pevzner *et al.* first demonstrated the controllable shaping of semiconductor nanowires and nanoribbons on SiO_2 using the lateral, confined and guided VLS growth technique[88]. Figure 4-10 shows that Si nanowires with different shapes can be grown on an amorphous substrate. Afterwards, LeBoeuf *et al.* investigated on the nucleation, solidification, single crystalline characteristics, and crystal orientations of Si thin films grown laterally on SiO_2[57,89].

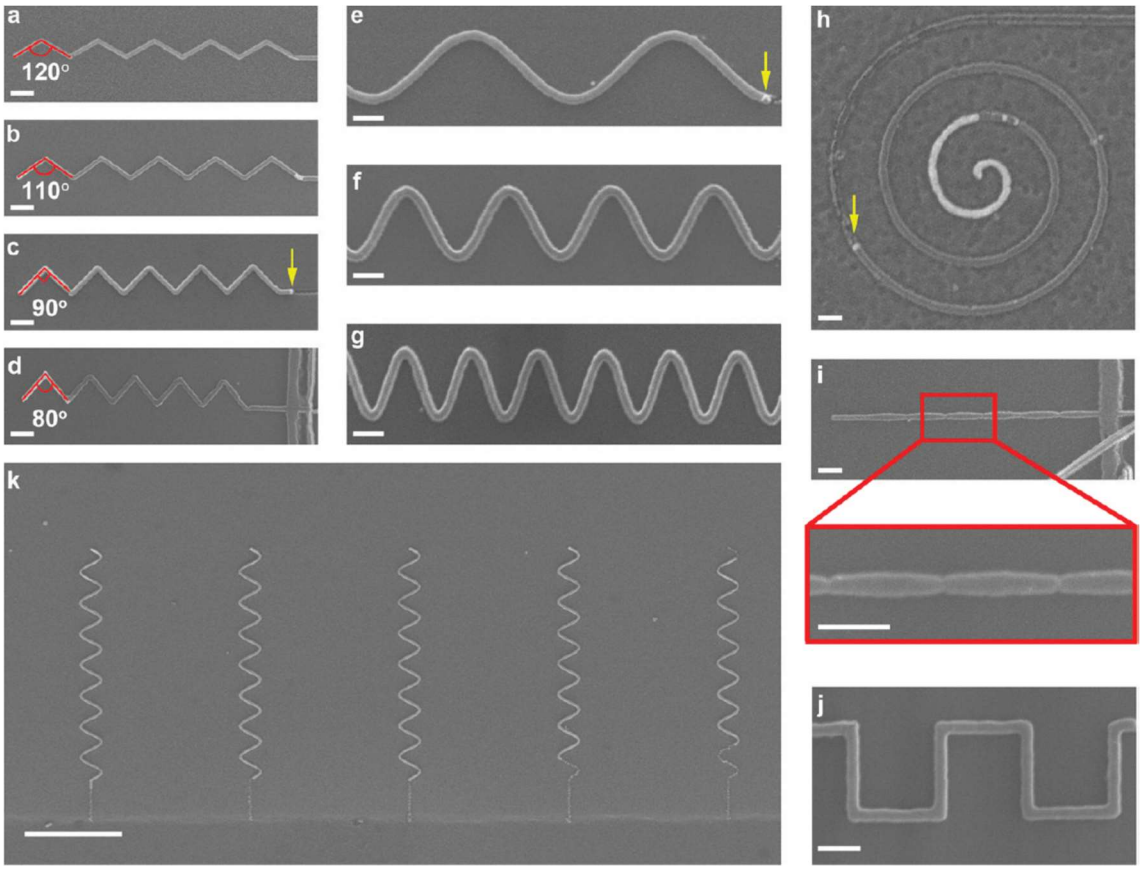

Figure 4-10. SEM micrographs of nanowires with different 2D shapes[88].

The lateral growth of Ge by VLS on amorphous or lattice-mismatched substrates was reported by Quitoriano *et al.* in 2010[11,12]. In Figure 4-11b, the authors initially grew Ge nanowires epitaxially on Si via the VLS mechanism; then the Ge nanowire was grown down and reached the surface of SiO_2 followed by the lateral growth against SiO_2. This approach can also be utilized to grow Ge nanowire laterally on Si (Figures 4-12 b-d). Importantly, it was found that many of the Ge nanowires grown laterally on Si or SiO_2 showed a single crystalline characteristic. Furthermore, even though a few crystal defects were observed near the Si-Ge interface or the ending of Ge nanowires, these Ge nanowires demonstrated surprisingly high crystal quality. It is suggested that an unclear relaxation mechanism from the lateral growth process may exist to accommodate the lattice mismatch between Si and Ge at nanoscale.

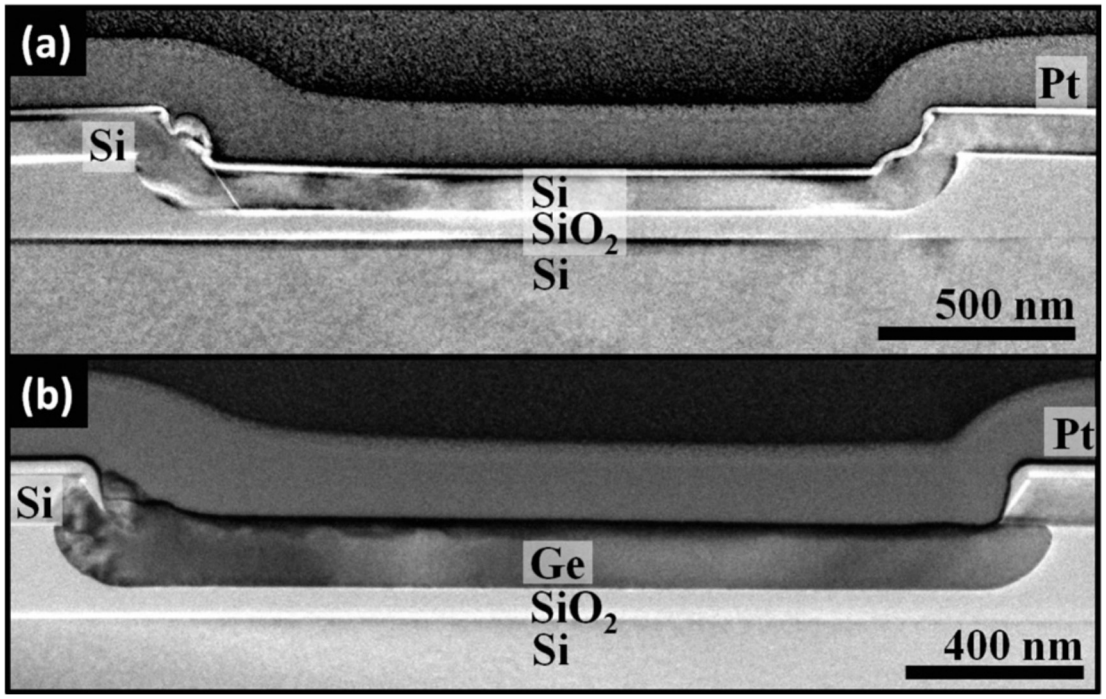

Figure 4-11. TEM micrographs of Si and Ge nanowires laterally grown on a SiO_2 surface[11].

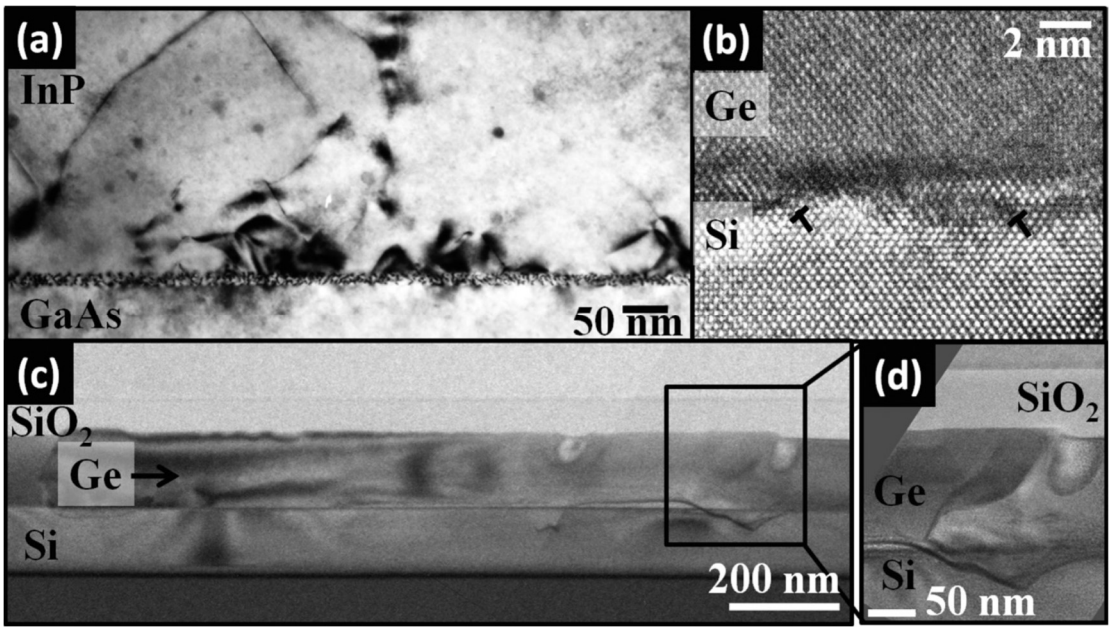

Figure 4-12. (a) TEM micrograph of InP grown on GaAs. (b) TEM micrographs of Ge nanowire laterally grown on Si[12].

The metal-catalyzed, lateral growth technique can be developed to be used for more applications, e.g. the lattice-mismatched, epitaxial thin film growth, since there might be a new relaxation mechanism to relieve the strain in the heterostructure without generating many additional dislocations or other defects. As mentioned in chapter 3, one possible explanation is the extension of misfit dislocations.

4.3. Lateral epitaxial growth of Ge on amorphous substrates

In addition, the lateral growth of Ge films on amorphous substrates without metal catalysts was studied[90,91,92,93]. For example, in Figure 4-13, rapid-melting-crystallization was used to laterally grow a high-quality Ge film from a single crystalline seed over an amorphous (insulating) film. Before the rapid melting process, an amorphous Ge strip was deposited on a single-crystalline Si substrate with an insulator layer on the surface. The insulator layer only partially covered the Si surface; thus, one end of the Ge strip could connect to the underlying substrate. Afterwards, the substrate was heated to a high temperature to melt the Ge. Then the sample was cooled. The Ge in contact with the Si solidified first (since the Si substrate acted as a crystalline template for the Ge) and formed a single crystalline Ge seed which induced the lateral, single-crystalline Ge growth on the insulator layer. The grown Ge layer showed good crystal quality, but the size of the Ge strip was limited to the cooling rate. For a large Ge film, it was possible that Ge might nucleate a crystal on the insulator before the growth front moved to this area which would result in a polycrystalline film.

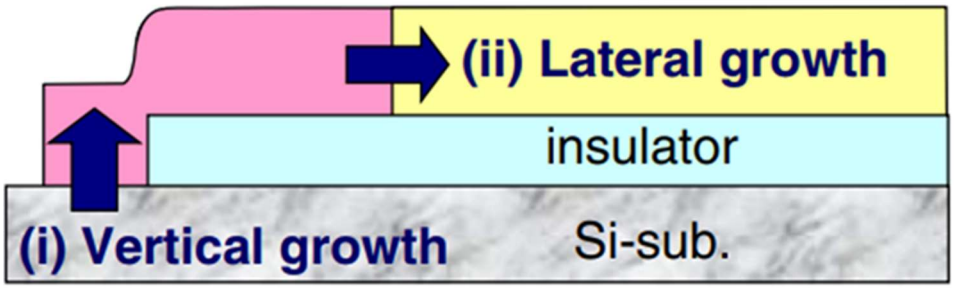

Figure 4-13. Schematic of rapid melting lateral-crystallization[91].

Chapter 5

Micro-crucible Fabrication

The micro-crucible structure (Figure 3-7) was fabricated in McGill Nanotools Microfab. The microfabrication techniques and the fabrication process are presented in this chapter.

5.1. Microfabrication Techniques

5.1.1. Photolithography

In micro-fabrication, photolithography is a process commonly used to create patterns on a substrate and its process flow is shown in Figure 5-1. Before more details regarding the process are discussed, a brief introduction of a photomask should be presented. In general, a photomask is a transparent plate partially covered by opaque Cr films designed to define the desired patterns, e.g. the strips in Figure 5-2a. As can be seen from the Figure 5-2b, the role of the Cr films is to absorb and block the incident light. It corresponds to the first step in Figure 5-1a where a photomask with predesigned patterns is located above a substrate allowing some, select

areas of a photoresist (PR) to be exposed to light. The PR is a photo-sensitive, viscous organic liquid spin-coated on the substrate and there are two types positive PR and negative PR. After light exposure, positive PR becomes soluble in a specific developer and can thus be easily removed away by the solvents (Figure 5-1b). On the other hand, negative PR becomes insoluble in the developer and the unexposed areas are removed (Figure 5-1c). In both cases, the patterns from the photomask will be transferred to the photoresist layer which can serve as a mask for selective etching (Figure 5-1d) or metal deposition (Figure 5-1e).

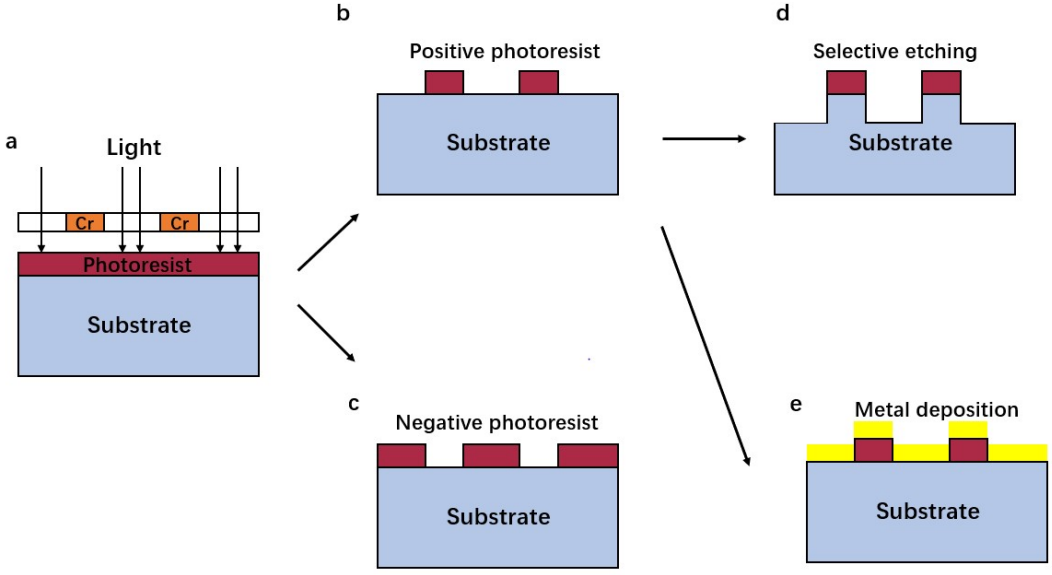

Figure 5-1. Process flow of the photolithography process.

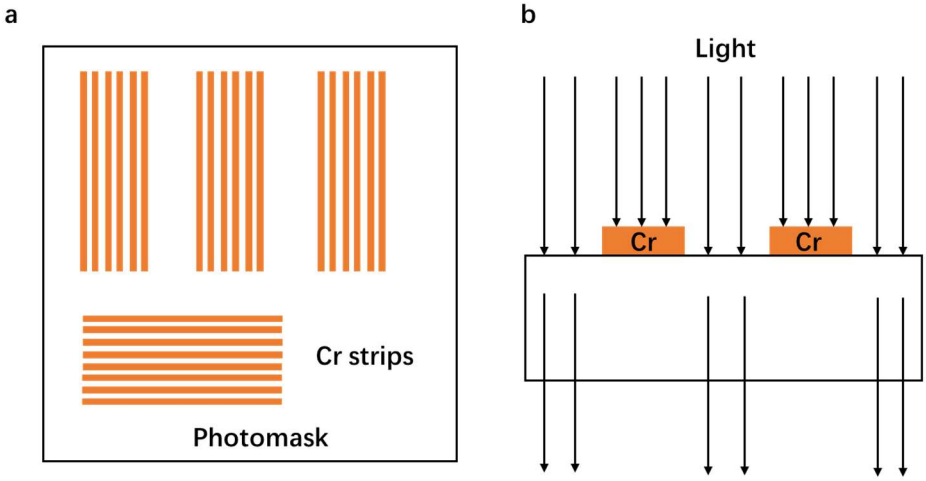

Figure 5-2. Schematic of a photomask in (a) plan-view and (b) cross-sectional view.

5.1.2. Electron-beam Deposition and Sputter Deposition

Electron-beam and sputter deposition are widely used for metal film deposition in micro-

fabrication. The inner structure of an electron-beam evaporator is shown in Figure 5-3a. It can be seen from the figure that the electrons are accelerated and guided by a magnetic field and move toward the target material. Then these high-energy electrons bombard the surface of the metal heating and vaporizing the metal. Afterwards, the vapors move straightly to the substrate and form a thin film over it. On contrary, in a sputtering chamber (Figure 5-3b), Ar ions are used to bombard the target metal. Ablated atoms on the target are ejected toward the substrate to grow a thin film. Electron-beam deposition generally grows less conformal films and is more extensively used for metal lift-off. Sputter deposition can be used to deposit more uniform and conformal films because the target is typically much larger in area, rather than a point-like source in an e-beam evaporator; however, sputter deposition can lead to plasma damage in the film.

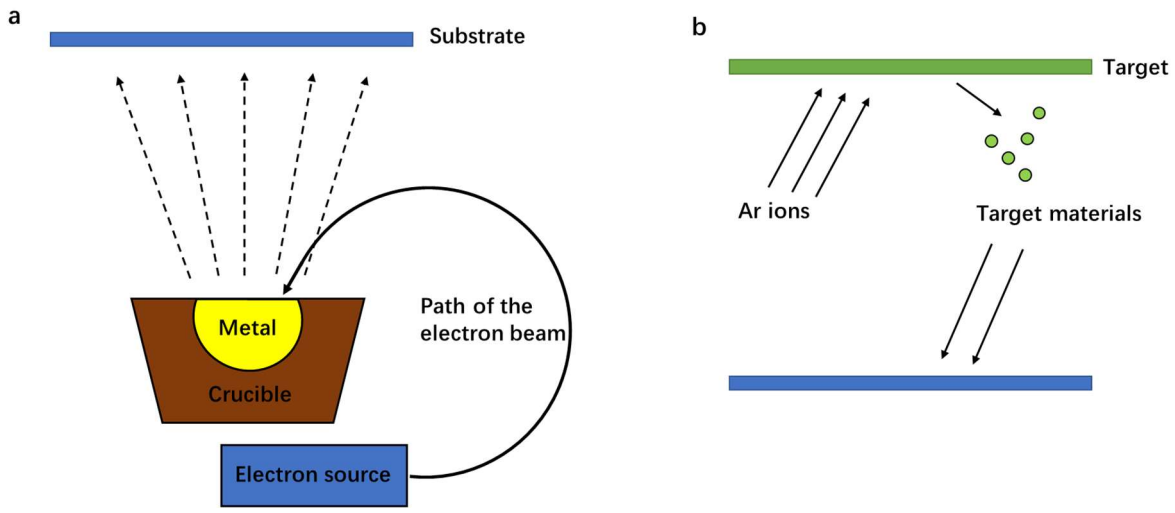

Figure 5-3. Schematics of the inner structure of (a) an electron beam evaporator (b) a sputtering chamber.

5.1.3. Metal Lift-off

Metal lift-off is a process to create patterns of a target metal on a substrate. For the first step, a metal layer is deposited on a patterned photoresist layer in an electron-beam evaporator. Here electron-beam deposition instead of sputter deposition is used because a less conformal growth is necessary to inhibit metal deposition on the photoresist sidewalls (Figure 5-4a, not 5-4b). The photoresist sidewalls must be uncovered because acetone is used to selectively etch the PR and the metal which is deposited on top of the PR floats in the solution thereby leaving only

the desired metal-covered areas remaining. The structure shown in Figure 5-1e can thus be fabricated followed by an ultrasonically agitated solvent bath to strip photoresist (Figure 5-4b). In the end, the predefined patterns from the mask can be generated on the substrate by the partial removal of the metal.

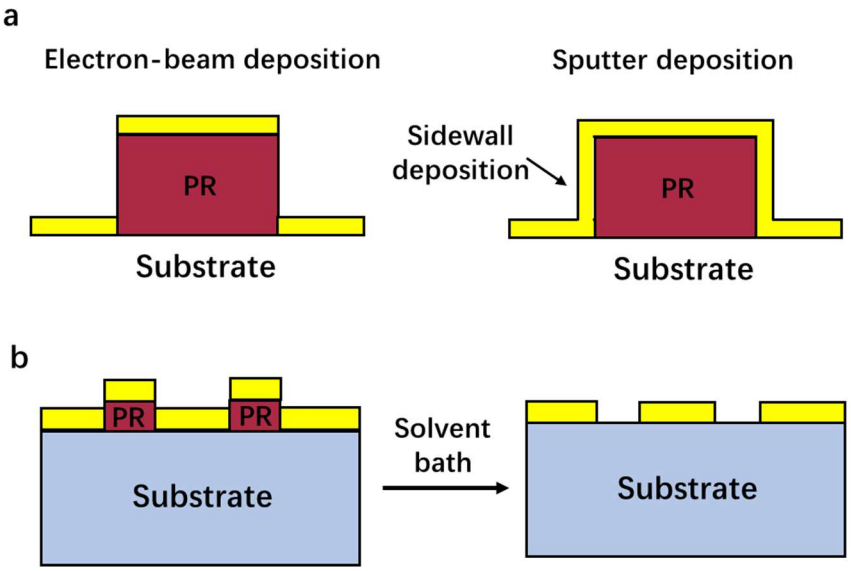

Figure 5-4. Schematic diagram of the metal lift-off process. (a) Metal deposition on a patterned photoresist layer by electron-beam deposition and sputter deposition (b) Photoresist Removal.

5.1.4. Plasma-Enhanced Chemical Vapor Deposition

Plasma-enhanced chemical vapor deposition (PECVD) is a variant of traditional CVD and a key feature of PECVD is the generation of a plasma of the reactants. The plasma can be used to lower the energetic barrier to crack the precursor gases, which means the growth rate of PECVD is much higher than that of traditional CVD at low temperatures. This is important because Si can diffuse into Au above the Si-Au eutectic temperature (363 ℃), which is not desirable. In fact, a 600 nm PECVD film of SiO_2 can be grown at a relatively low temperature, 300 ℃, in one minute. It is a fast and convenient process to deposit layers on a substrate; however, the crystal quality of the PECVD layers suffers from the impurities or vacancies that could be incorporated into the films in a high-energy plasma environment. PECVD is widely used for the deposition of dielectric layers (e.g. SiO_2 and Si_3N_4 which were used in this study).

5.1.5. Wet Etching

Wet etching is a chemical reaction process in liquid to remove undesirable materials on a substrate. The most common case of wet etching in micro-fabrication is the etching of SiO_2 using HF. It is based on the chemical reaction below:

$$6HF + SiO_2 \rightarrow H_2SiF_6 + 2H_2O$$

It is well known that Si wafers suffer from oxidation when exposed to air; a very thin SiO_2 layer on Si, termed the native oxide, should be removed before processing a step requiring an exposed Si surface. In general, the native oxide is etched by a low-concentration HF solution since the HF etching is a convenient, effective, and low-cost process. It is also common that wet etching is used to remove metal on a substrate. Transene Gold Etchant TFA, for instance, is a KI-I_2 based solution that is widely used to etch Au (etch rate = 28 Å/sec.) at room temperature. Furthermore, this gold etchant as well as many of other liquid etchants are compatible with negative and positive photoresists and can be easily washed away after use. Therefore, wet etching can be used to selectively etch a layer where the regions to be etched are specifically defined by photoresist masks. It is important to note that liquid etchants typically etch the target materials isotropically; however, there are some liquid etchants when etching crystalline materials that etch anisotropically. For a single crystalline material, the etching rate of a certain set of lattice planes may be much lower that of other planes which may lead to anisotropic etching (Figure 5-5a). More often, single crystalline, polycrystalline or amorphous materials are etched by liquid etchants isotropically (Figure 5-5b). As can be seen in Figure 5-5b, isotropic wet etching results in often unwanted etching underneath the masks (undercutting). Thus, the shape of the etched materials deviates from the original predefined structure.

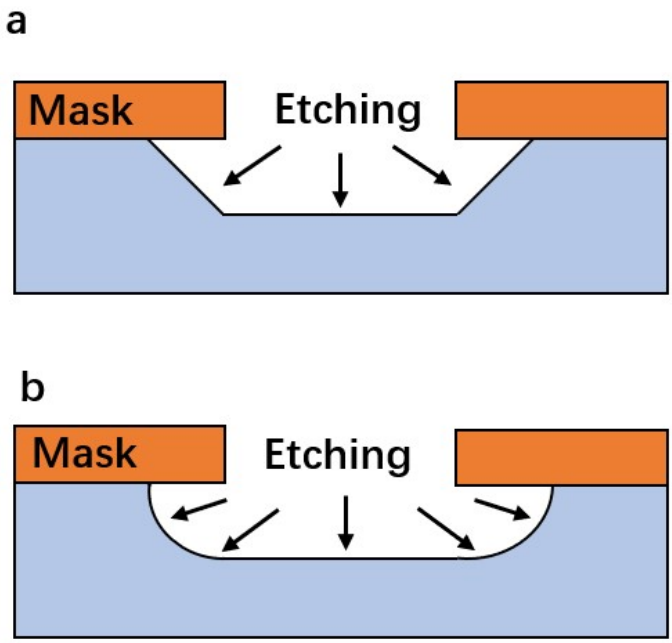

Figure 5-5. Schematics of wet etching profile in (a) an anisotropic and (b) an isotropic etch of a surface.

5.1.6. Reactive Ion Etching

Reactive-ion etching (RIE) is a dry etching process used in micro-fabrication to anisotropically etch materials on a substrate. In an RIE process, a chemically reactive plasma is generated in the chamber by using a RF (radio frequency) electromagnetic field. Afterwards, the positive ions drift toward the target substrate due to the large potential field caused by the accumulation of electrons on the substrate (Figure 5-6a). The positive ions then bombard and ablate the target removing material, some of which deposits on the substrate. RIE is an extensively used dry processing tool because it provides an effective way to quickly etch the materials that may not have an appropriate liquid etchant. Besides, RIE has a characteristic of anisotropic etching to accurately define the final shape of the product (Figure 5-6b).

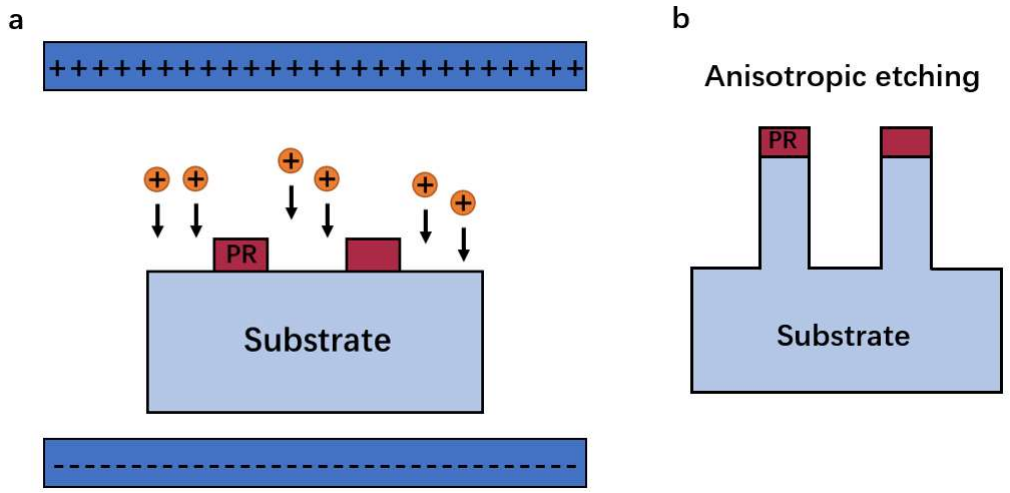

Figure 5-6. (a) Schematic of the inner structure of a RIE chamber. (b) Schematic of RIE etching profile.

5.2 Fabrication process of micro-crucibles

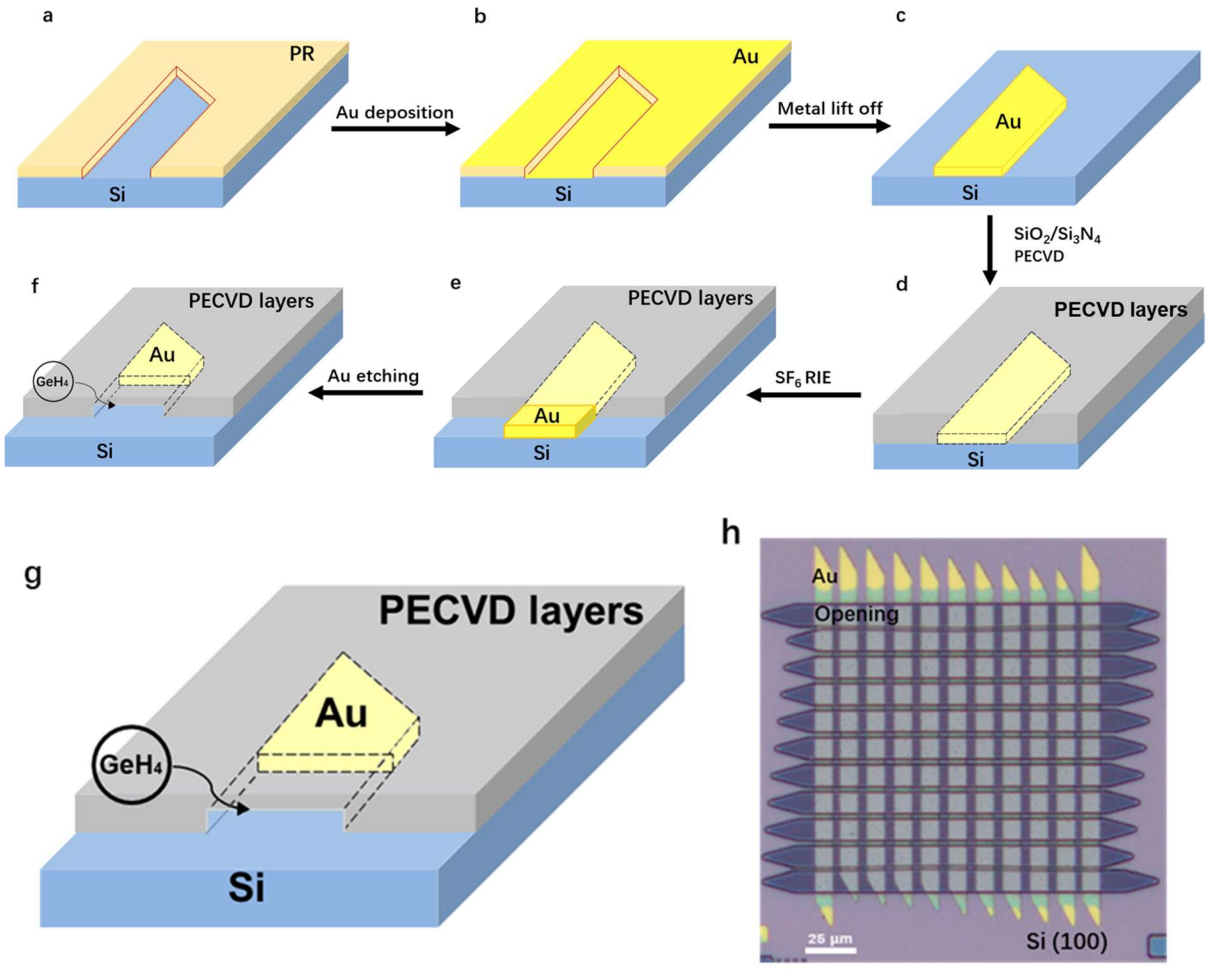

Figure 5-7. (a-f) Schematic diagrams of the fabrication process for the micro-crucible structure. (g) Schematic diagram of the micro-crucible structure. (h) Optic micrograph of micro-crucibles on Si.

The fabrication process of the micro-crucible structure began with a silicon (100) substrate. First, the substrates were cleaned in a piranha solution (H_2SO_4 : H_2O_2 :: 3:1) at 80 ℃ for 15 mins to remove organic or metal residues. This was followed by a photolithography process to spin a layer of PR onto the Si substrate and the PR layer was developed to partially expose the Si wafer for the subsequent metal lift-off process (Figure 5-7a). After that, the substrates were dipped in a 10% HF solution for 30 s to remove the native oxide and were cleaned by DI water and dried by N_2 gun. The substrates were then immediately loaded into the chamber of a BJD1800 Electron Beam Evaporator. After the chamber pressure reached about 5.5×10^{-6} Torr, a 100 nm Au thin film was deposited onto the substrate (Figure 5-7b). The Au deposition was followed by ultrasonically agitated solvents baths (10-min Removal 1165 bath, 10-min Acetone bath, 5-min IPA and 5-min DI water) to strip the photoresist and transfer the pattern from the mask to the substrate (Figure 5-7c). Then a piranha cleaning process was performed to remove the photoresist residue; note that even small amounts of carbon residue may burn in the PECVD chamber at 300 ℃. After the substrate was carefully cleaned by DI water and dried by N_2 gun, it was inserted into a PECVD chamber for the deposition of SiO_2/Si/Si_3N_4 capping layers (Figure 5-7d). A ~ 600 nm SiO_2 layer was first deposited on the substrate at 300 ℃; then a ~ 600 nm Si layer and a ~ 140 nm Si_3N_4 were deposited in sequence on the oxide layer to enhance the strength of the micro-crucible. Afterwards, the substrate was patterned again by photolithography to selectively mask the substrates. This was followed by a long (960 s) SF_6 Deep Reactive-Ion Etching (DRIE) to etch through the PECVD capping layers and selectively expose the Au. Finally, the substrates were immersed into Transene Gold Etchant TFA solution to partially etch the Au to form the final micro-crucible structure (Figures 5-7e and 5-7f). The Figure 5-7h shows a plan-view optical micrograph of the substrate where the micro-crucibles have a triangular shape.

Chapter 6

CVD Growth of Ge

6.1. CVD System

The CVD growth of Ge was performed in a custom-built, Metal-Organic Chemical Vapor Deposition (MOCVD) system. Figure 6-1 shows the schematic of the MOCVD system which was adapted to grow Ge using a 10% GeH_4, balance H_2, gas tank (Figure 6-1a). As can be seen from the figure, the GeH_4 cylinder is connected to a gas flowmeter (C_2) that controls the flow of GeH_4/H_2 gas mixture in the range of 0 - 100 Standard Cubic Centimeters per Minute (sccm). Figure 6-1b highlights a (high purity, 99.999%) H_2 cylinder and Figure 6-1c shows a H_2 purifier employed to further improve the purity of H_2. The lines between the H_2 cylinder and the H_2 purifier were purged by N_2 before the H_2 was flowed through the purifier. This step is necessary

because even a small amount of O_2 may damage the H_2 purifier. The H_2 flow then passed through the purifier and entered the run line and the vent line; the flowmeters of the run line and the vent line are denoted by A_1 (1500 - 10000 sccm) and A_2, respectively. The run line is connected to the reactors supplying gases for the CVD growth whereas the vent line is directly connected to the pump and the gas burner. Note that there is a line to link up the H_2 purifier with the GeH_4 line; the gas flow in this line is controlled by the flowmeter C_3. It was used to pressurize the GeH_4 line using H_2 and it was combined with a GeH_4 vent line (controlled by C_4) to purge the entire GeH_4 line prior to CVD growth. In Figure 6-1, the GeH_4 line is connected with the vent line and the run line by the valves denoted by d and e, respectively. The GeH_4/H_2 gas mixture was flowed in the run line during the CVD growth and the flow was switched to the vent line before and after growth. It should be aware that the H_2 flow from the H_2 purifier serving as the carrier gas flowed in both the run and vent lines all the time. Figure 6-1f shows the CVD reactor which is a cold-wall CVD reactor fabricated by a quartz tube, a lamp heater, and a water/air cooling system. The CVD growth can be performed in the temperature range of 200 - 1000 ℃ with a heating rate of 10 degree per second. In addition, the reactor pressure is monitored and controlled by a pressure controlled (P_4) with the help of a couple of valves (VC_2, VC_3, and VC_4). In the end, all the gases from both the run line and the vent line are transported to a gas burner (800 ℃) to decompose the possible toxic gases.

6.2. CVD Growth Procedure

Before CVD growth, the prepared substrates were cleaned by acetone, IPA, deionized water, and a 10% HF solution to clean the surface of the samples and to remove the naive oxide of Si. Then the substrates were immediately loaded into the CVD chamber (Figure 6-2). Afterwards, the reactor was closed and pumped to reach a low pressure (40 mTorr) followed by a 15 min H_2 purging process. Once in the reactor, the temperature was increased using a lamp heater above the Au-Si eutectic temperature (~ 360 ℃) to liquify the Au-Si mixture; the annealing temperature was usually set at 450 ℃ and it was measured by a thermocouple underneath the substrate (Figure 6-2). The annealing process generally lasted for more than 15 min to form the Au-Si liquid alloy and remove possible moisture and contaminates. Then a mixture of GeH_4

and H_2 was introduced to the vent line and flowed in the entire GeH_4 line for at least 5 min. In the meanwhile, the reactor temperature was changed to the desirable growth temperature. After the reactor temperature was stable, the GeH_4/H_2 gases were switched to the reactor via the run line to grow Ge films at a growth temperature in the range of 375 - 500 ℃ for 1 - 2 hours. Throughout this process, the GeH_4 flow was varied from 2 - 10 sccm, but the total gas flow rate (2.5 slm) and the reactor pressure (40 mTorr) were kept constant.

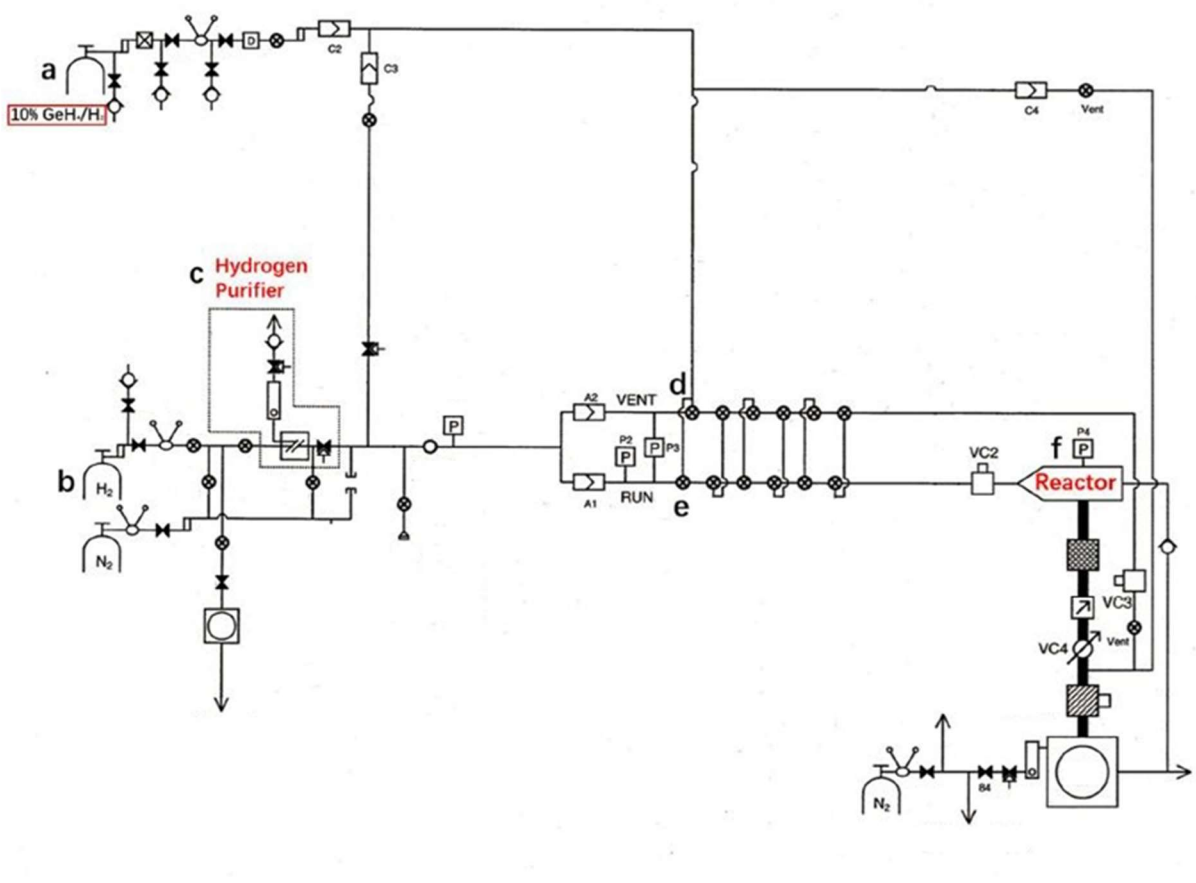

Figure 6-1. Schematic of the Ge CVD system.

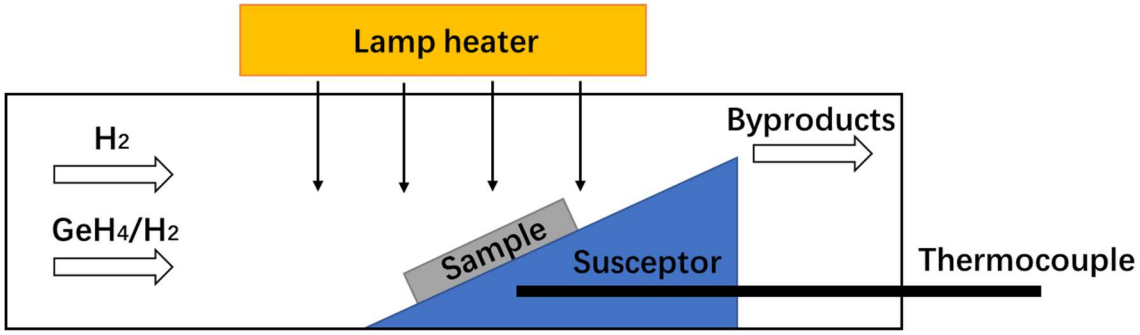

Figure 6-2. Schematic of the cold-wall CVD reactor.

6.3. CVD Growth Parameters

The CVD growth parameters, e.g. the growth temperature, the gas flows, and the reactor pressure, etc. play important roles in a growth process and can critically affect the thin film quality. Here a simple kinetics study of the Ge growth using GeH_4 is presented. First, it would be helpful to review the major steps of a typical CVD process: the transportation of vapor precursors, the adsorption of the precursors, the deposition of thin film on the substrate, and the desorption of the byproducts. In order to simplify the analysis, we assume that the decomposition of the GeH_4 is a first order reaction without any vapor-phase reactions. Hence, the diffusion of the GeH_4 from the vapor phase to the substrate and the subsequent decomposition of the GeH_4 on the substrate are considered to be two primary steps to determine the growth rate. As shown in Figure 6-3, the flux of the GeH_4 through a boundary layer can be describe by the below equation:

$$F_1 = h_G (C_G - C_S)$$

where C_G and C_S are the GeH_4 concentration in the gas phase and near the substrate surface, respectively and h_G is the mass transfer coefficient. On the other hand, the flux of the consumption of the GeH_4 near the substrate surface can be written as below:

$$F_2 = k_S C_S$$

where k_S is the chemical surface reaction rate and is exponentially related to the growth temperature ($ks = k_0 \exp(-E_a/kT)$, k is Boltzmann constant and T is temperature). The total growth rate is limited by the slowest step and can be divided into two regions (the mass-transfer-controlled region and reaction-controlled region) based on the above equations. The Ge lateral growths might be reaction controlled, since the growths were performed at a low temperature and a large flow carrier gas (H_2) was used to transport the GeH_4. However, the gas must diffuse underneath the capping layers over relatively long distances, which may affect the gas transport process and add complexity to this study. In both cases (mass transfer controlled, and reaction controlled), as can be seen from the equations, the Ge partial pressure in the vapor phase (affecting C_G and C_S) and the growth temperature (affecting k_S and h_G) are the key parameters to control the growth rate. The Ge partial pressure can be varied by adjusting the GeH_4 flow, the total gas flow, and the reactor pressure. Nevertheless, the total gas flow and the

reactor pressure were generally kept constant to grow the films more reproducibly because these two parameters may also affect the status of gas-flow distribution in the reactor. The GeH_4 flow thus is the major parameter to change the GeH_4 partial pressure in the vapor phase.

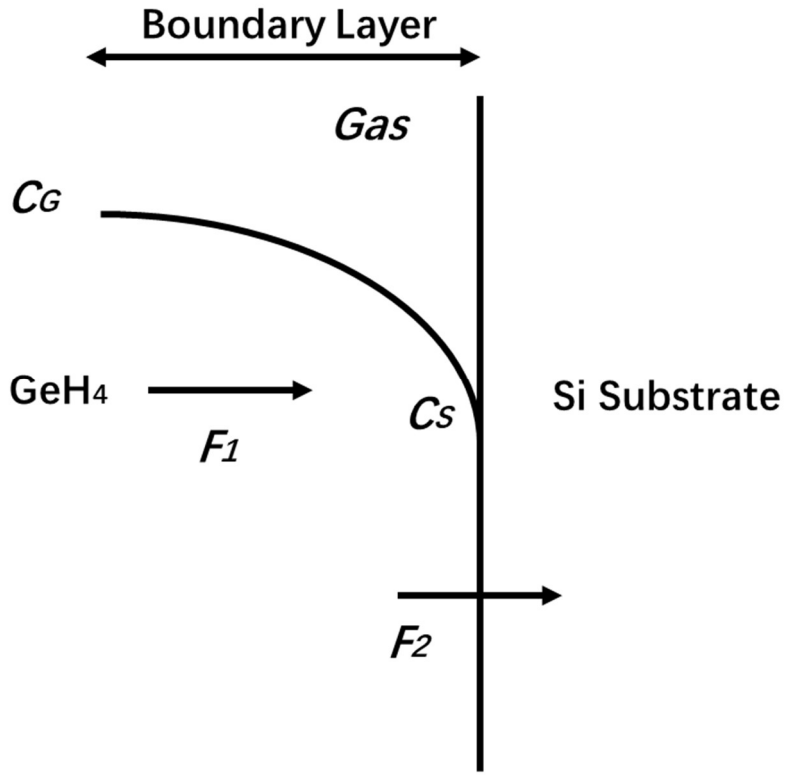

Figure 6-3. The concentration profile and fluxes of GeH_4 near the Si substrate in a Ge CVD process.

In our experiments, a narrow temperature range (375 ℃ - 500 ℃) was used to grow Ge films. Note that the Au-Si eutectic temperature is around 363 ℃, and it means that the growth temperature is required to be higher than this temperature to liquify the Au-Si alloy. Furthermore, it was found that high growth temperature (> 500 ℃) resulted in fast and uncatalyzed deposition of Ge on the Si substrates and the capping layers. It should be aware that only the catalyzed growth of Ge within the micro-crucibles is desirable; thus, it is necessary to employ a relatively low temperature to better control the growth location. Table 6-1 lists the actual parameters of eight Ge CVD growths. As can be seen from the table, the total gas flow (H_2 flow +10% GeH_4/H_2 flow) was set to 2500 sccm and the reactor pressure was set to 40 mTorr. Basically, Ge films were grown at different temperatures with different Ge partial pressures to investigate on how the variables affected the growths. At relatively high temperature, e.g. 450 ℃, a lower 10% GeH_4/H_2 flow (20 sccm) was generally used to reduce

the growth rate (e.g. growth #1). In addition, the growth time may be extended from 1 hour to 1.5 or 2 hours because it can help to increase the film size under a low-growth-rate condition.

Growth #	H_2 flow (sccm)	10% GeH_4/H_2 flow (sccm)	Reactor pressure (mTorr)	Growth time	Temperature (°C)
1	2480	20	40	1h	450
2	2480	20	40	1h	400
3	2480	20	40	2h	400
4	2460	40	40	1h	400
5	2460	40	40	1h	375
6	2470	30	40	1h	375
7	2460	40	40	1.5h	375
8	2470	30	40	2h	375

Table 6-1. Summary of the parameters of several Ge CVD growths.

6.4. Growth Reproducibility

In order to study the growths systematically, it is important to grow the films reproducibly. Unfortunately, many factors (oxygen, moisture, etc.) other than the growth variables have great impacts on the growth results. Therefore, it is essential to purge the system using H_2 or N_2 before and after CVD growth. Typically, the system should be purged for more than 4 hours after long non-utilization of the system or the change of new reactor. All the lines that will be used are required to be purged for 15 min and the whole system should be purged again for 15 minutes before each deposition. Even though the purging process was carefully carried out, it was found that the growth reproducibility was still not satisfactory. Later, it was figured out that it would be helpful to run the system or at least the H_2 lines all the time (five days per week) to improve the reproducibility.

Chapter 7

Characterization Techniques

7.1. Scanning Electron Microscopy

Scanning Electron Microscopy is an imaging technique widely used in engineering, biomedicine, physics, chemistry, and other disciplines. In an SEM chamber, the electrons are ejected from an electron gun and accelerated through a high voltage to the sample. Then the electrons interact with the sample and generate various signals (secondary electrons, backscattering electrons, and characteristic X-rays, etc.) that can provide information with respect to the topography and composition of the sample surface (Figure 7-1a). In general, an SEM scans the sample surface with a raster scan electron beam where the resulting signal(s) (electrons or photons) are collected from one point before exposing another point to the

incident electron beam. Secondary electrons and backscattering electrons are two primary signals in SEM; they both can be used to depict the surface morphologies of the sample. However, secondary electrons can produce higher resolution image and are less sensitive to the atomic numbers of the target materials. A secondary electron SEM micrograph, therefore, can give us better topographic contrast compared to backscattering SEM micrograph. On the other hand, the emission coefficients of backscattering electrons depend strongly on the atomic number (Figure 7-1b). It is thus suggested that a backscattered electron micrograph is promising to reflect the surface composition of the sample.

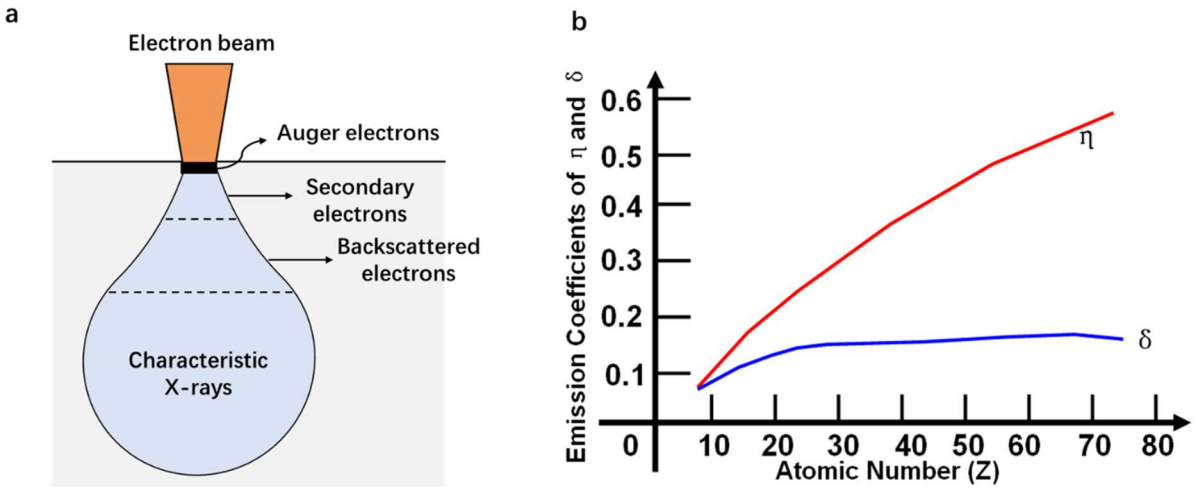

Figure 7-1. (a) Schematic of the signals that can be generated in SEM. (b) Schematic shows emission coefficients of backscattering electrons (η) and secondary electrons (δ), depending on atomic number (Z)[94].

In our experiments, a Hitachi SU-3500 SEM system was used to preliminarily characterize the Ge thin film morphologies within the micro-crucibles. Figure 7-2 shows a SEM micrograph of micro-crucibles after the CVD growth of Ge. In this SEM micrograph, the Ge(Si) crystal demonstrates a color of light-black, a contrast that is slightly brighter than the dark-black Si substrate. Here the Ge(Si) is used to denote that a small amount of Si might be incorporated into the Ge films. By contrast, the Au catalysts show a much brighter contrast in the SEM micrograph due to the larger atomic number of Au. The outlines of the Ge(Si) film and the Au catalysts within the third micro-crucible are demonstrated in this image. The plan-view SEM micrographs can provide valuable information, e.g. the possible first nucleation site of the

Ge(Si) film in the micro-crucible, the size and the shape of the Ge(Si) film, the uncatalyzed growths, and the shape of the Au catalysts after growth, etc.

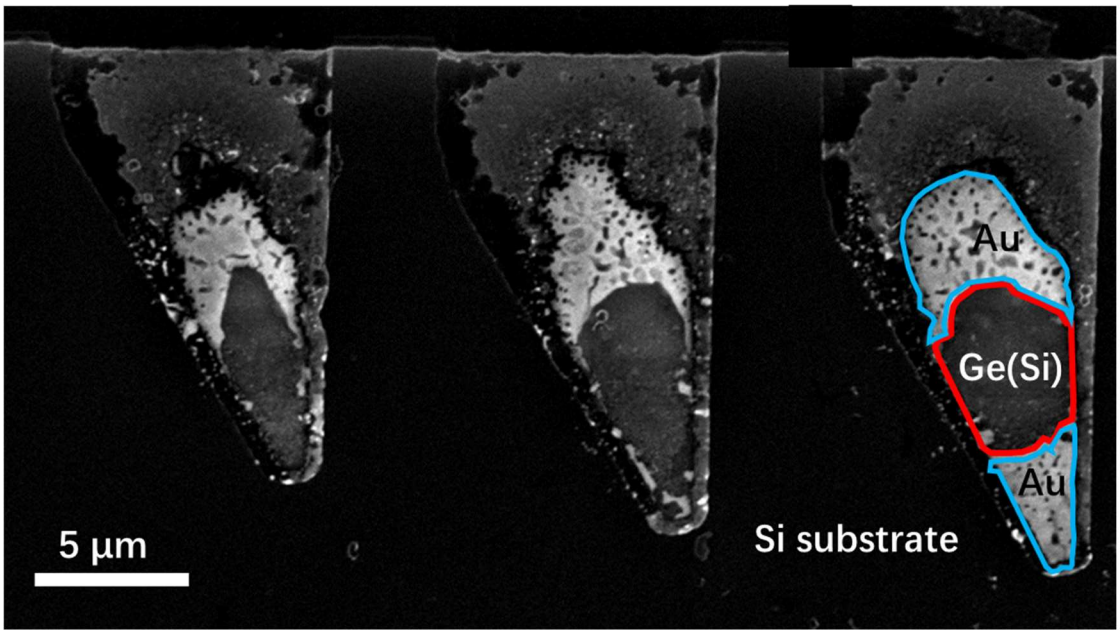

Figure 7-2. SEM micrograph of micro-crucibles after CVD growth; the film was grown at 375 °C a reactor pressure of 40 mTorr and a total flow rate of 2500 sccm with a GeH_4 flow of 5 sccm for 1 hour. The red polygon delineates the outline of the Ge(Si) film and the blue polygons delineate the outlines of the Au catalysts.

7.2. Transmission electron microscopy

Transmission electron microscopy (TEM) is a microscopy technique where electrons are accelerated by high voltage to pass through an ultra-thin film (typically 100 nm or less), interacting with the specimen and generating a variety of signals. In our experiments, TEM is a key technique in characterizing the defects (dislocations, stacking faults, twins, and grain boundaries, etc.) within the Ge-on-Si film. In addition, TEM can provide higher resolution compared to a standard SEM and can reach atomic resolution level to obtain more information, e.g. the crystallographic orientation and the approximate lattice constant. However, the preparation of TEM specimens is a time-consuming and tough process because the sample must be thinned to ~ 100 nm to be electron-transparent.

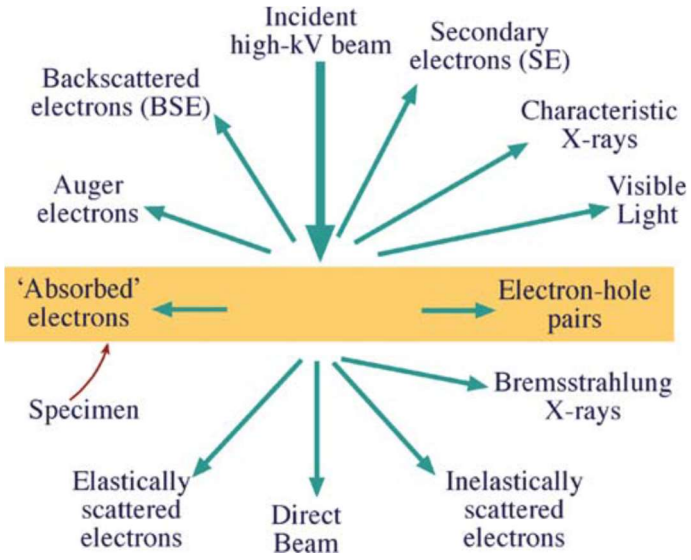

Figure 7-3. Signals generated in TEM[95].

In order to better understand the mechanism of TEM imaging, the fundamental knowledge with respect to the scattering or diffraction of electrons (electrons are treated as particles or waves) should be discussed. As shown in Figure 7-3, electron scattering can be mainly divided into two categories: inelastic scattering and elastic scattering. Inelastic scattering are the scattering mechanisms related to the energy loss of electrons and the scattered electrons generally form the background signals of a TEM micrograph. On the contrary, elastically scattered electrons are the primary signals responsible for the formation of contrasts in an image. The contrast in TEM is defined as the difference in intensity (number of the electrons that are detected) between two regions.

In 1913, William H. and Mr. W. Lawrence Bragg first proposed a simple equation to describe the patterns observed in X-ray diffraction:

$$n\lambda = 2d\sin\theta\,,$$

It was later demonstrated that this equation, Bragg's law, can also be applied to diffraction in TEM. As we can see from the equation, the wavelength of the electrons (λ), the incident angle of the electron beam (θ), and the lattice spacing of a set of crystalline planes (d) may satisfy the Bragg condition to generate strong diffraction (Figure 7-4a). Assuming that there are two grains with different crystallographic orientations in a thin-film specimen (Figure 7-4b). The

specimen can be tilted so that the electron beam can be strongly diffracted by grain#1 whereas the beam almost entirely penetrates grain#2. Then an objective aperture can be used to filter out the diffraction beams and allow only the direct beam to form the image. It is thus expected that the grain#1 shows a darker contrast since the incident beam was partially diffracted by the grain#1. That is the basic mechanism of the diffraction contrast in TEM.

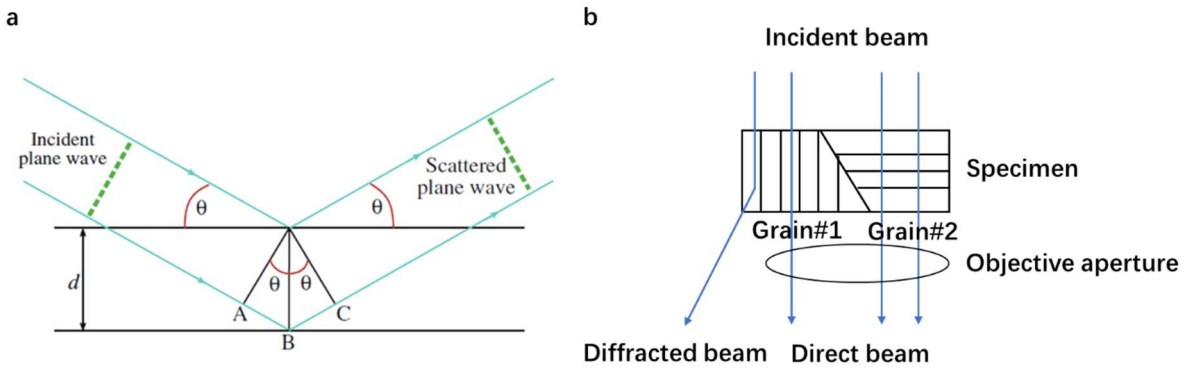

Figure 7-4. (a) Schematic of a set of crystalline planes that satisfy the Bragg condition to generate strong diffraction[96]. (b) Schematic of the basic mechanism of the diffraction contrast in TEM.

One of the main applications of TEM is its ability to observe crystal defects in a specimen. As shown in Figure 7-5a, the lattice planes distort around a dislocation center and the lattice distortion changes the angle between the incident beam and the crystal planes. The intensity of diffraction beams around the dislocation can either be increased or decreased (Figure 7-5b), giving rise to the contrast of the dislocation line. Furthermore, more in-depth TEM studies demonstrate that no diffraction contrast can be seen from a dislocation if the burgers vector of the dislocation is orthogonal to the active diffraction vector ($\boldsymbol{g} \cdot \boldsymbol{b} = \mathbf{0}$) . This rule can be used to determine the burgers vector of a certain dislocation or to highlight the dislocations using a specific diffraction condition. For the study of SiGe/Si or Ge/Si heterostructure, (220) or (2-20) diffraction conditions are commonly employed to highlight 60° threading dislocations that are lying on the (111) planes with a burgers vectors in the (110) directions.

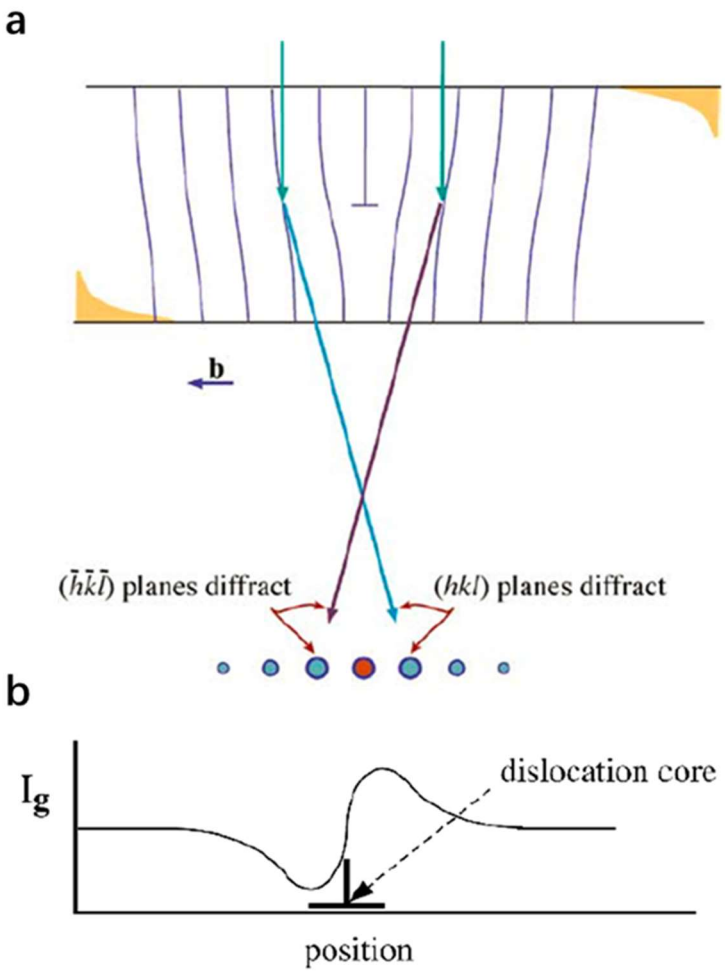

Figure 7-5. (a) Crystalline planes are distorted because of a dislocation[96]. (b) Diffraction contrast as a result of a dislocation[96].

High-resolution transmission electron microscopy (HRTEM) is an imaging mode of TEM based on phase contrast instead of diffraction contrast (one direct beam and a couple of diffraction beams are used for imaging). HRTEM is a powerful tool to study semiconductor materials at an atomic level; it is the technique providing us atomic images to directly determine crystal orientations and the epitaxial relationship (Figure 7-6). In the HRTEM mode, the electron beams passing through the thin foil are affected by the potential fields of the materials and then reconstruct the atomic structure of thin specimens on the screen.

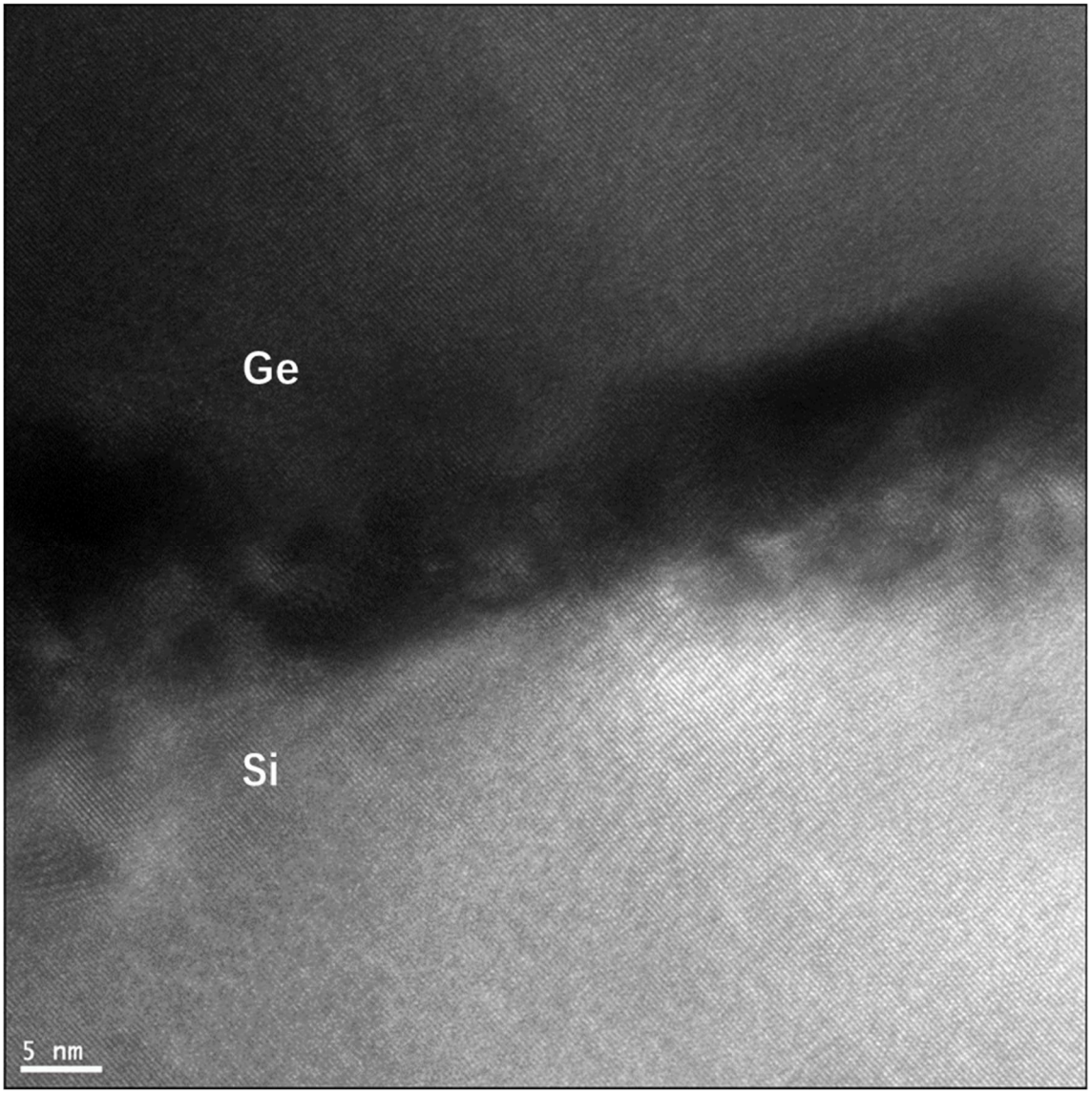

Figure 7-6. High-resolution TEM micrograph of Ge/Si interface.

In this thesis, TEM micrographs can not only provide higher magnification imaging for the study of thin film morphologies or compositions, but also contribute to the understanding of the defects within the films. Note that Au has black contrast in TEM imaging because Au can scatter more electrons due to the large atomic number. As shown in Figure 7-7, the information regarding the density and distribution of defects can be directly obtained from the plan-view TEM micrograph. In this TEM micrograph, the dislocations generally appear as slightly curved lines whereas the stacking fault show a contrast of parallel straight lines which are separated by partial dislocations on each side. The TEM results may help to study the evolution of dislocations during the lateral growth process. Moreover, TEM imaging can also give us clues

with respect to the possible first nucleation regions and the lateral growth directions.

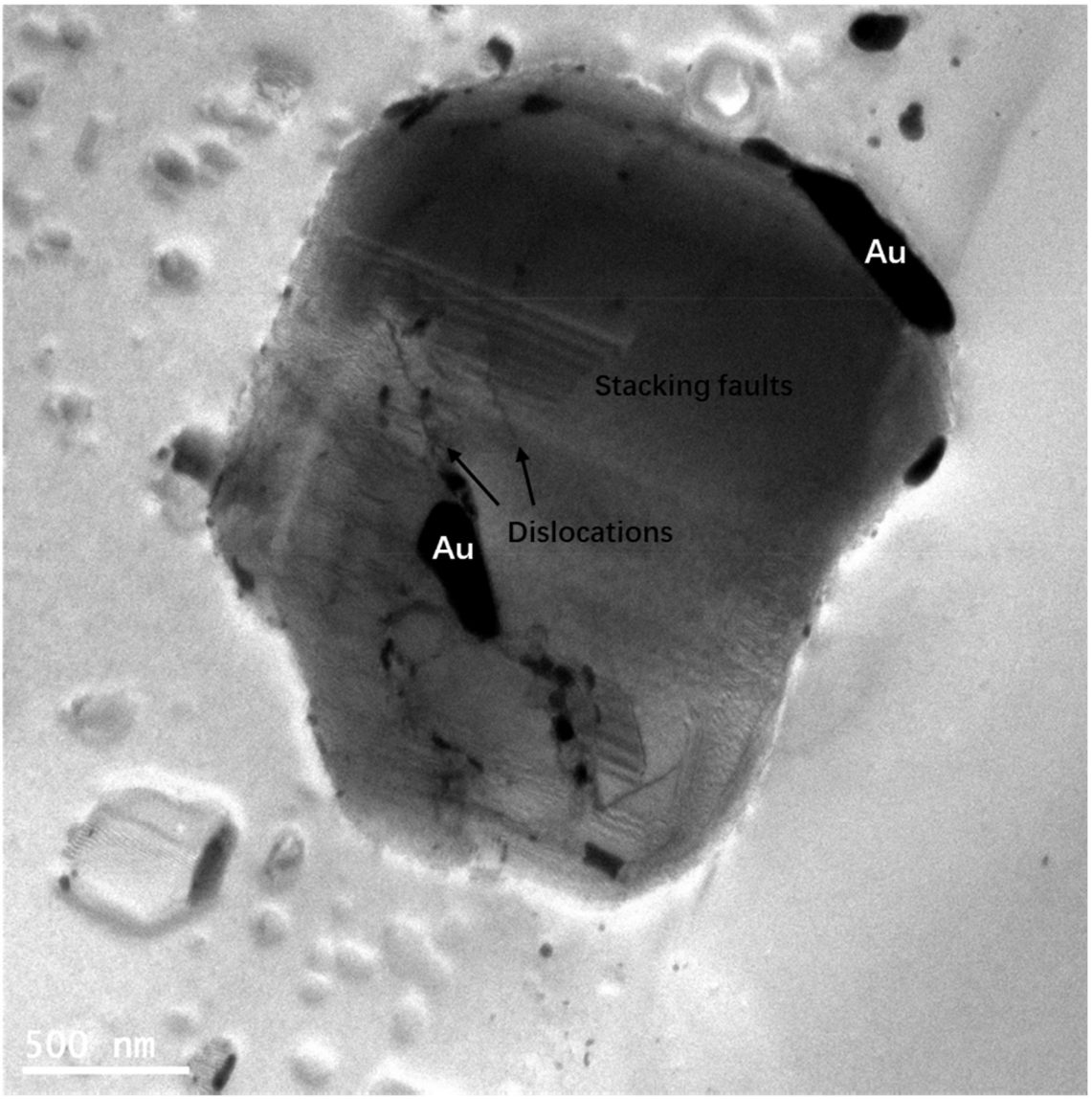

Figure 7-7. Plan-view TEM micrograph of a lateral grown Ge film on Si under 220 diffraction condition.

7.3. X-ray diffraction

X-ray diffraction (XRD) is the technique to directly measure the lattice constants of the epitaxially grown Ge films on Si to obtain the information of the strain and composition. As discussed in Chapter 3, at the beginning of the Ge growth on Si, the lattices in the Si-Ge heterostructure are fully strained (Figure 7-8a) because of the larger lattice of Ge compare to Si. The in-plane lattices ($a^{//}$, the lattices parallel to the interface) of the fully strained Ge are

compressed; on the other hand, the out-of-plane lattices ($a^{\perp}$, the lattices perpendicular to the interface) are stretched due to deformation of the lattice. Afterwards, this strain can be plastically relaxed by the formation of dislocations at the interface. One should be aware that both $a^{//}$ and $a^{\perp}$ are equal if the Ge film is fully relaxed (Figure 7-8b). In order to determine if a Ge layer on Si is relaxed or partially relaxed, the most straightforward way is to measure the in-plane Ge lattices ($a^{//}$). The measured $a^{//}$ should be between the lattice constant of Si (a_{Si}) and that of Ge (a_{Ge}). If the $a^{//}$ is approaching that of pure Ge, it would suggest that the film is almost entirely relaxed by dislocations. Therefore, the relaxation (R) of the film can be defined as the below equation:

$$R = \frac{a_{//} - a_{Si}}{a_{Ge} - a_{Si}},$$

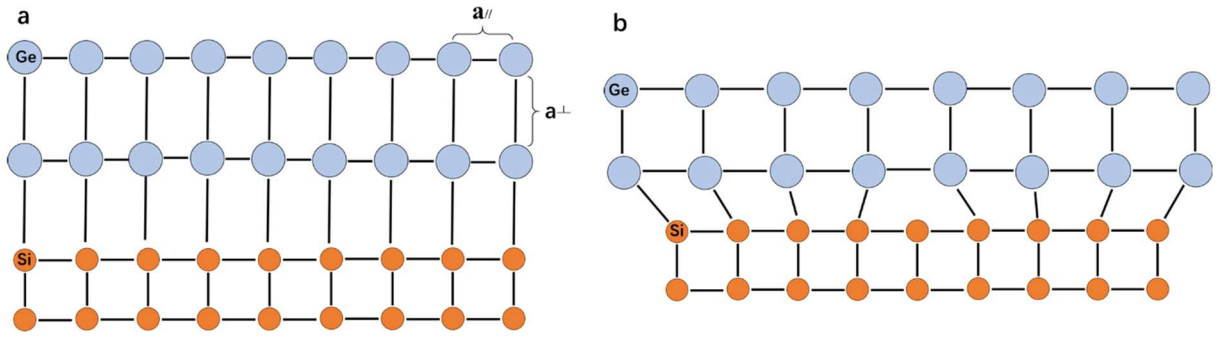

Figure 7-8. Schematic of the Si-Ge interface; the Ge film are (a) fully strained (b) fully relaxed.

In addition, the measurements of the lattice constants can provide composition information for us. It is important to note that Si might be incorporated into the Ge films during the lateral growth process; thus, the composition of the film is unclear. Fortunately, the composition of $Si_{1-x}Ge_x$ (x) can be approximated from the equation: $a(x) = 5.431 + 0.20x + 0.027x^2$, where $a(x)$ is the $Si_{1-x}Ge_x$ lattice constant.

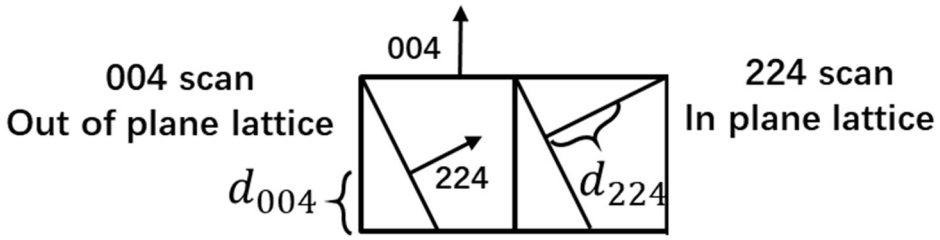

Figure 7-9. XRD measurements of in-plan and out-of-plane lattices by using 004 and 224 scans.

According to Bragg's law, after the beams of X-ray enters a single-crystalline thin film, the strongest reflected beam can be observed at an angle which is determined by the equation:

$$sin\ \theta = n\lambda/2d,$$

where λ is the wavelength of the incident beams and d is the lattice spacing of the planes. Then the lattice spacing can be used to calculate the in- and out-of-plane lattice constants of the Ge epilayer. As shown in Figure 7-9, the out-of-plane lattice of the film can be directly calculated from the 004 lattice spacing (d_{004}) and the in-plane lattice can be obtained from the 224 lattice spacing (d_{224}) after knowing the out-of-plane lattice.

Chapter 8

Metal-catalyzed, Lateral Epitaxial Growth Process

Chapter 8 presents the experimental findings, focusing on the study of the lateral growth process. The growth films were mainly characterized by a Hitachi SU-3500 Variable Pressure Scanning Electron Microscopy to study the roles of Au catalyst in the growth process and the effects of the growth variables (e.g., growth temperature, gas flow) on the size and morphology of the films. Furthermore, this chapter provides a simple model to calculate the final film size and suggests ideas to predetermine the first nucleation site and control the growth direction. In the end, this chapter discusses the results with respect to the uncatalyzed, vapor-solid growth.

8.1. Results and Discussion

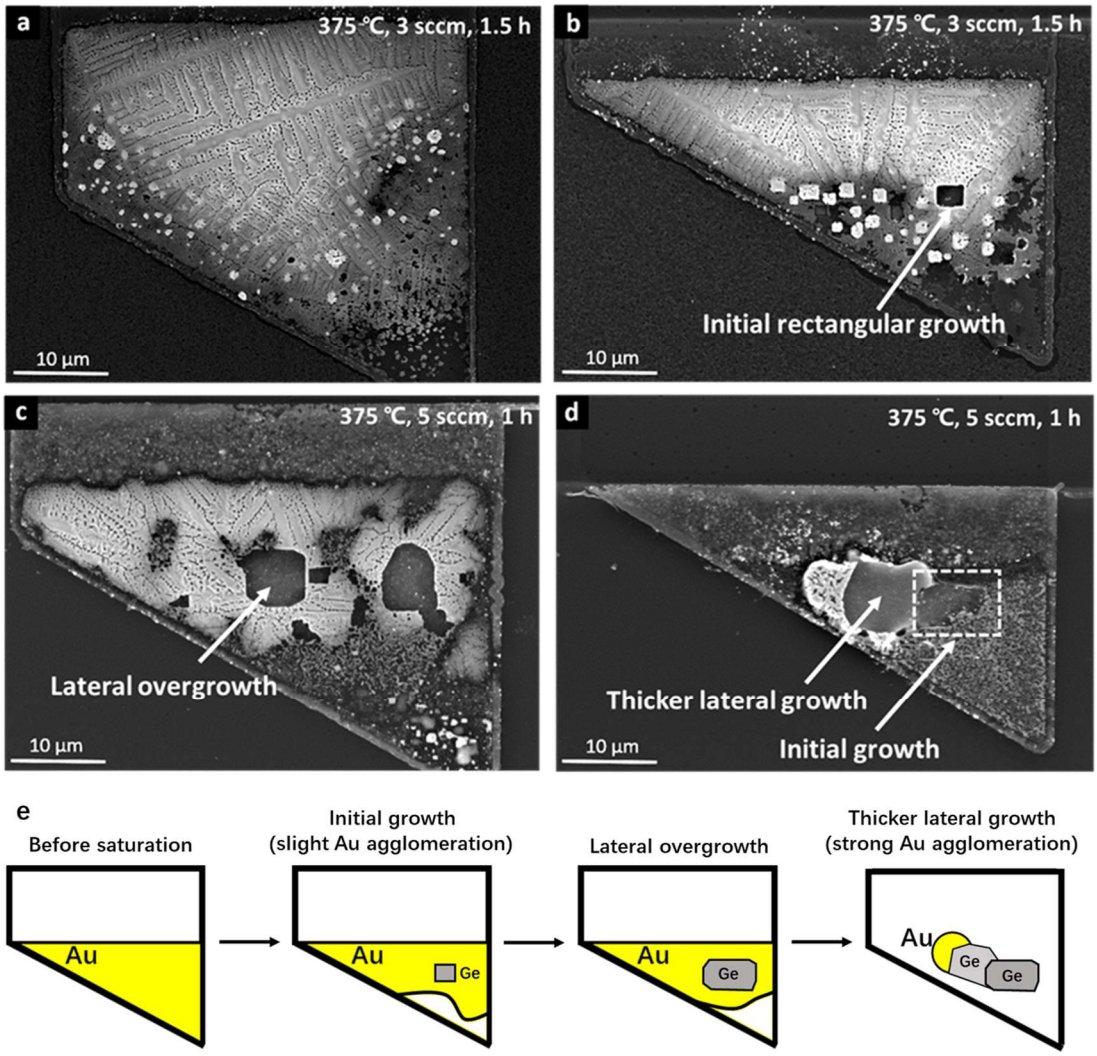

Figure 8-1. (a-d) SEM micrographs of laterally grown Ge(Si) films on Si which may represent different periods of the growth process; films were grown at 375 °C, a reactor pressure of 40 mTorr and a total flow rate of 2500 sccm under two growth rates: 3 sccm GeH_4 for 1.5 hours (Figures 8-1a and b) and 5 sccm GeH_4 for 1 hour (Figures 2c and d). (e) Schematic diagrams of the lateral growth process.

After CVD growth, a combination of SF_6 RIE and HF dipping was used to etch the PECVD capping layers to observe the micro-crucibles in high resolution SEM. In Figures 8-1 a-d, SEM micrographs from two samples are shown representing different stages of the growth process. Both micro-crucibles in Figures 8-1a and 8-1b were from the same sample; but, their overall Au catalyst size was large and small, respectively. In Figure 8-1a, there are no observable Ge(Si) films in a large micro-crucible after a growth of 90 min at a GeH_4 flow of 3 sccm. This image

thus shows a micro-crucible before the gas precursors supersaturate the Au. The annotation Ge(Si) was used to show that a small amount of Si may be incorporated into the Ge films. In contrast, a rectangular Ge(Si) film (indicated by an arrow in Figure 8-1b) appeared in a relatively small micro-crucible on the same sample. This fact indicates that the Ge atoms supersaturated the small Au catalysts in Figure 8-1b and nucleated an initial Ge(Si) film. In addition, this Ge(Si) film were found to be faceted and were probably bounded by the planes with low surface free energies, e.g. {111} planes, which reveals the epitaxial relationship of the Ge(Si) films with the underlying Si substrate. To increase the film size, the GeH_4 flow was increased to 5 sccm and the results are shown in Figures 8-1c and 8-1d, again two micro-crucibles from the same sample with different Au catalyst sizes. An observation is that Au agglomerated more in Figures 8-1c and 8-1d than Figures 8-1a and 8-1b. This is seen by the fact that there is less Au in the micro-crucible tip at the lower right of Figures 8-1c and 8-1d compared to Figures 8-1a and 8-1b. In Figure 8-1c, the Ge films grew laterally from smaller nucleation areas, like those depicted in Figure 8-1b. In Figure 8-1d, Au agglomerated even more in a small micro-crucible leading to thicker lateral overgrowth of a Ge(Si) film with a brighter-contrast. The thicker Ge film leads to more backscattered electrons compared to the underlying Si and thus also leads to a brighter contrast. The schematic diagrams in Figure 8-1e depict the lateral growth process more clearly and divide the process into 4 stages: before saturation, initial growth, lateral overgrowth and thicker lateral growth. However, it is important to note that only small number of micro-crucibles went through all the stages. Which stage a micro-crucible will reach after a growth depends on the growth conditions, e.g., the growth temperature, the gas flow rates, the growth time, the size and shape of the micro-crucible. In summary, Figures 8-1a-d show two major implications: first, Ge can saturate the liquids to nucleate initial small Ge(Si) crystals; second, Ge(Si) films can be grown laterally on Si extended from the first-to-nucleate areas.

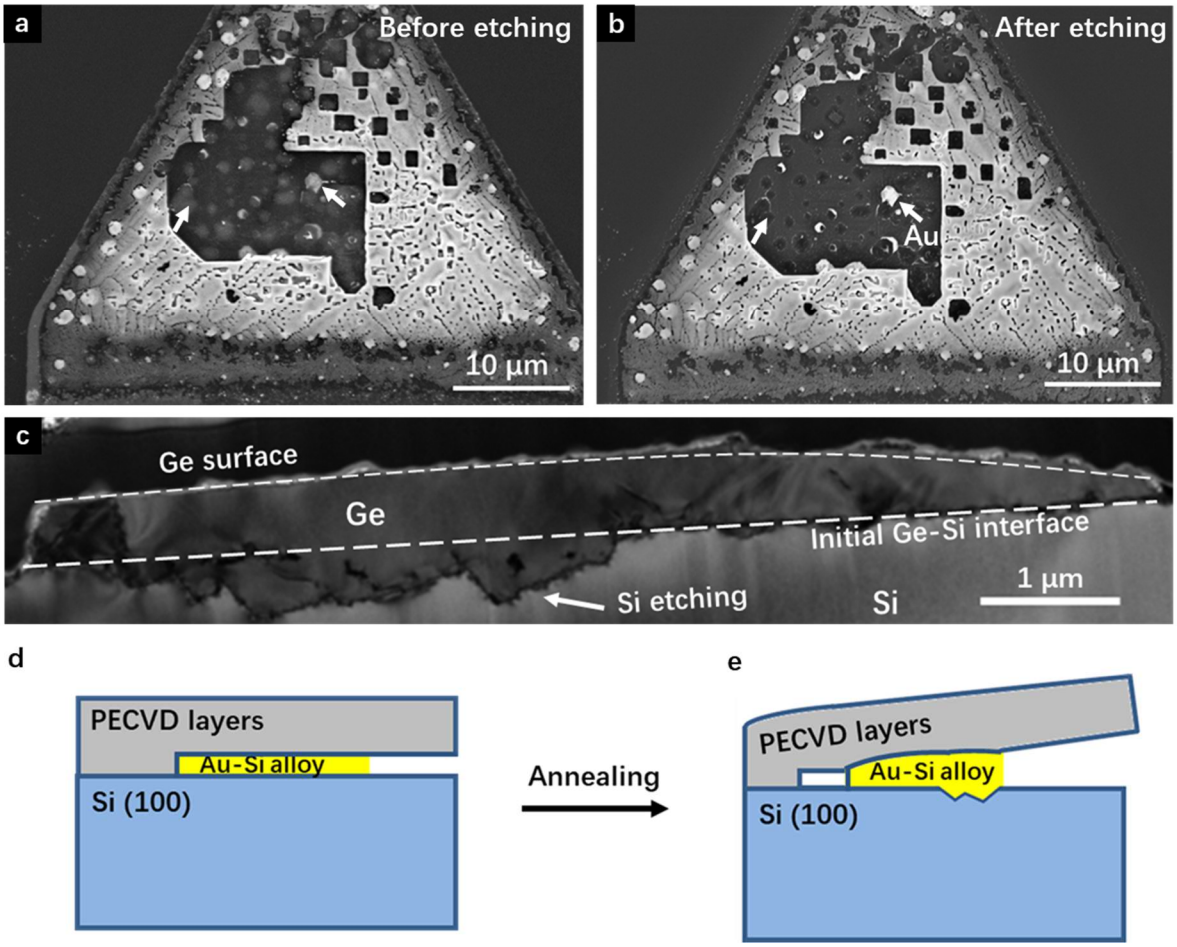

Figure 8-2. SEM micrographs of laterally grown Ge(Si) films on Si (a) before chemical etching, (b) after chemical etching. Films were grown at 375 °C, a reactor pressure of 40 mTorr and a total flow rate of 2500 sccm for 1 hour and the GeH_4 flow is 5 sccm. (c) Cross-sectional TEM micrograph of a laterally grown Ge(Si) film on Si. Films were grown at 375 °C for 1 hour and the GeH_4 flow is 5 sccm, (d) Schematic diagrams showing the agglomeration of Au on Si during annealing process.

In the metal-catalyzed, lateral growth process, the Au catalyst has been thought as a key factor in engineering the growth since the catalyst can define the first nucleation site and guide the growth direction[11]. It should be aware that the catalyst morphology would change when the substrate was heated above a temperature higher than the Au-Si eutectic temperature. First, A certain amount of Si was dissolved into the Au catalyst to form a liquid alloy, which resulted in the etching of the underlying Si substrate. In Figure 8-2a, a relatively large Ge(Si) film in a micro-crucible demonstrates contrast variations: a number of brighter spots seem to uniformly distribute within the film. As mentioned above, we attribute it to more scattering of electrons from these spots either because of the thickness increase of the film or the composition variations. The left arrow in Figure 8-2a points to a grey-contrast spot, and the right arrow

points to an even-brighter spot. In order to figure out the causes of the contrast variations, the Ge(Si) film was completely etched by a CrO_3-based solution that has a high selectivity between Si and Ge[97]. The SEM micrograph of the same micro-crucible after chemical etching is shown in Figure 8-2b. It was found that the gray spot in Figure 8-2a corresponds to a pitted area in Figure 8-2b, left arrow, and the even-brighter spot is Figure 8-2a is a Au particle underneath the Ge(Si) film. The dissolution of Si into Au led to the formation of the etch pit indicated by the arrow in Figure 8-2b. The etch pit increased the film thickness locally and thus increased the contrast. It is worth noting, however, that not all micro-crucibles demonstrated apparent contrast variations in the Ge(Si) films. It is thus suggested that high-density etch pits were not always formed underneath the films. A very thin native oxide layer between Au and Si is speculated to be the cause of the different morphologies of etch pits. Additionally, it is possible that the Au merely etched a small part of the underlying Si substrate before it became saturated with Si.

Besides, as can be seen from the plan-view SEM micrographs in Figures 8-1 a-d, the liquid Au-Si alloy tends to agglomerate on Si to varying degrees during annealing. This phenomenon can be studied more in cross-sectional TEM. Figure 8-2c shows a cross-sectional TEM micrograph of a Ge(Si) film that agglomerated strongly in a similar fashion to that depicted in Figure 8-1d; the surface of the film was found to be curvy and the left side is higher than the right side. The Au had a thickness of 100 nm prior to annealing and, as can be seen in Figure 8-2c, the Ge(Si) thickness is as large as 500 nm above the initial Si substrate surface. Since the Au thickness should be equal to the Ge(Si) film thickness, it suggests that the Au has a higher thickness on the left-hand side in the growth process. It is therefore suggested that the Au agglomerates from right to left as shown schematically in the Figure 8-2d; note that the Au agglomeration is possible from the deformation of the capping layers. Moreover, a jagged interface was clearly seen on the left-hand side in Figure 8-2c. As discussed above, the underlying Si substrate was dissolved into Au during the annealing process and the space was subsequently occupied by the Ge(Si) film.

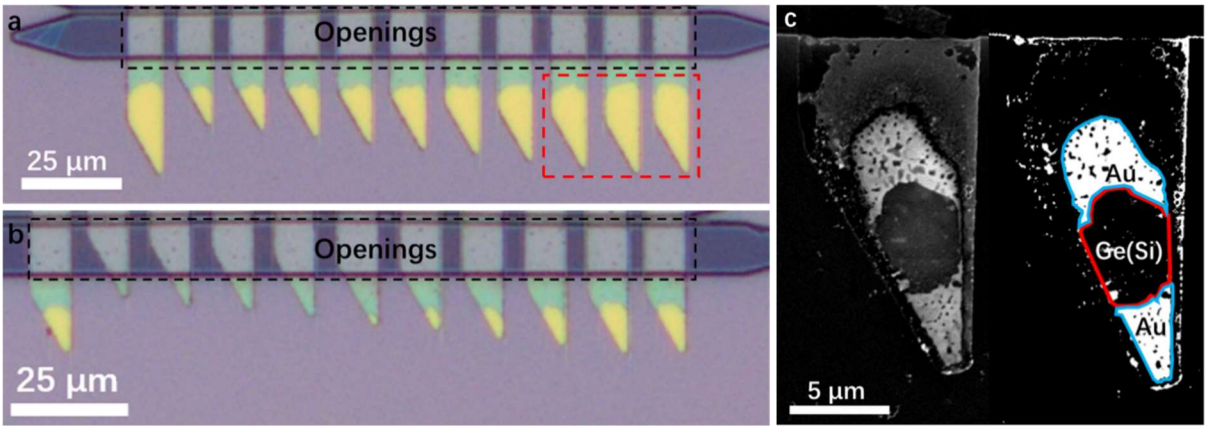

Figure 8-3. (a) and (b) Optical micrographs of micro-crucibles containing different amounts of yellow-colored Au catalyst prior to CVD growth; the black dashed-line boxes highlight the openings. (c) SEM micrograph of a micro-crucible after CVD growth and the image after being processed; the film was grown at 375 ℃ a reactor pressure of 40 mTorr and a total flow rate of 2500 sccm with a GeH_4 flow of 5 sccm for 1 hour. The red polygon delineates the outline of the Ge(Si) film and the blue polygons delineate the outlines of the catalysts. The areas of the film and the catalysts in plan-view images can be estimated by measuring the areas of the red and blue polygons.

Furthermore, under a certain growth condition, we hypothesized that the Au size and geometric shape have impacts on the Ge(Si) film growth. In order to understand this topic (the effect of the Au area on the area of the film, for example) more deeply, as shown in Figures 8-3a and b, micro-crucibles are designed to contain different amounts of Au (increasing amount of yellow-colored Au from left to right except for the leftmost one). After CVD growth, we processed the SEM images of the micro-crucibles and measured the areas of the Ge(Si) films and the Au catalysts in plan-view SEM (Figure 8-3c). Here, it is important to point out that we used the final Au size (what we measured in SEM) rather than the original one (in the optical images) to carry out the study. The results of this study can inspire us to figure out the ways to increase film size under a certain growth condition, which is important because the ideal way to grow a Ge(Si) films is to predefine a nucleation site and then laterally grow the film as large as possible from the crystal seed.

The Figure 8-4a shows Ge(Si) films grown within micro-crucibles containing different amounts of Au catalyst. As can be seen from Figure 8-4a, the tips of the micro-crucibles (the acute angle at the bottom) can induce the first nucleation of the Ge(Si) films. However, it was found that only two films (having the two least amounts of Au present) were grown from the

tips and the rest Ge(Si) films nucleated further from the tip. Because of this, a lower decomposition rate of GeH_4 might help to nucleate the films at the tip, since it reduces the Ge concentration near the Au-vapor interface and gives more time for the Ge to diffuse to the tip. Interestingly, a general trend can be seen in Figure 8-4a, as the Au size increase the Ge(Si) film size initially increases as well until the Ge(Si) film size plateaus and then decreases with increasing Au size. This trend can be more clearly seen in Figure 8-4b, a plot of the Ge(Si) film size versus the Au size as collected from numerous plan-view SEM images by performing a areal size calculation from the images like that shown in Figure 8-3c, where the blue-highlighted areas total to form the Au area and the red-highlighted area is the Ge(Si) area. This observation can be understood in the following manner, as the size of the Au catalyst increases, both the vapor-liquid interface and the volume of the Au are expected to increase. A previous study by LeBoeuf *et al.* has reported that the growth is not limited by diffusion of the gas but rather by the reaction kinetics at the surface[57]. Since the experimental conditions in this thesis are similar to his conditions, it is thus suggested that the more surface, the more Ge can be absorbed by the Au. Nevertheless, a larger Au catalyst also requires more Ge atoms to saturate Au catalyst. Given that the ratio of the vapor-liquid interface's area to the Au's volume decreases with increasing Au size, the overall outcome should be that the Ge(Si) film size decreases after it reaches a plateau. Therefore, the results from Figures 8-4 a and 8-4b suggest that large Ge(Si) films are likely to be grown within a medium sized Au catalyst.

In addition, note that the film area as measured in plan-view images is not perfectly proportional to the actual volume of the Ge(Si) films because the Au catalysts tend to agglomerate and increase the thickness of the Ge(Si) films, which cannot be determined in plan-view SEM. This is especially true if the micro-crucibles are large because the more Au present tends to enable larger Au agglomeration (Figure 8-4a). The Au agglomeration is likely to be one cause of the larger variance in the data (Figure 8-4b) as the initial Au area exceeds 40 μm^2.

In order to better correlate the Ge(Si) film size and the Au size, the ratio A_{Ge}/A_{Au} is used and is plotted against the Au area in Figure 8-4c; it shows a monotonically decreasing curve. The use

of A_{Ge}/A_{Au} minimizes the impacts of the increase of the film thickness by assuming that the Ge film and the Au have the same thickness which is valid in most cases. As suggested by the trend of the curve in Figure 8-4c, a small Au catalyst can be used to grow a Ge crystal much larger than itself (high A_{Ge}/A_{Au}) under this growth condition, e.g. the growth of Ge nanowires catalyzed by Au nano-particles. On the other hand, a larger Au catalyst (> 20 μm^2) generally grows a Ge crystal smaller than itself. In extreme cases, the GeH_4 may not supersaturate a large Au catalyst to nucleate any Ge crystals.

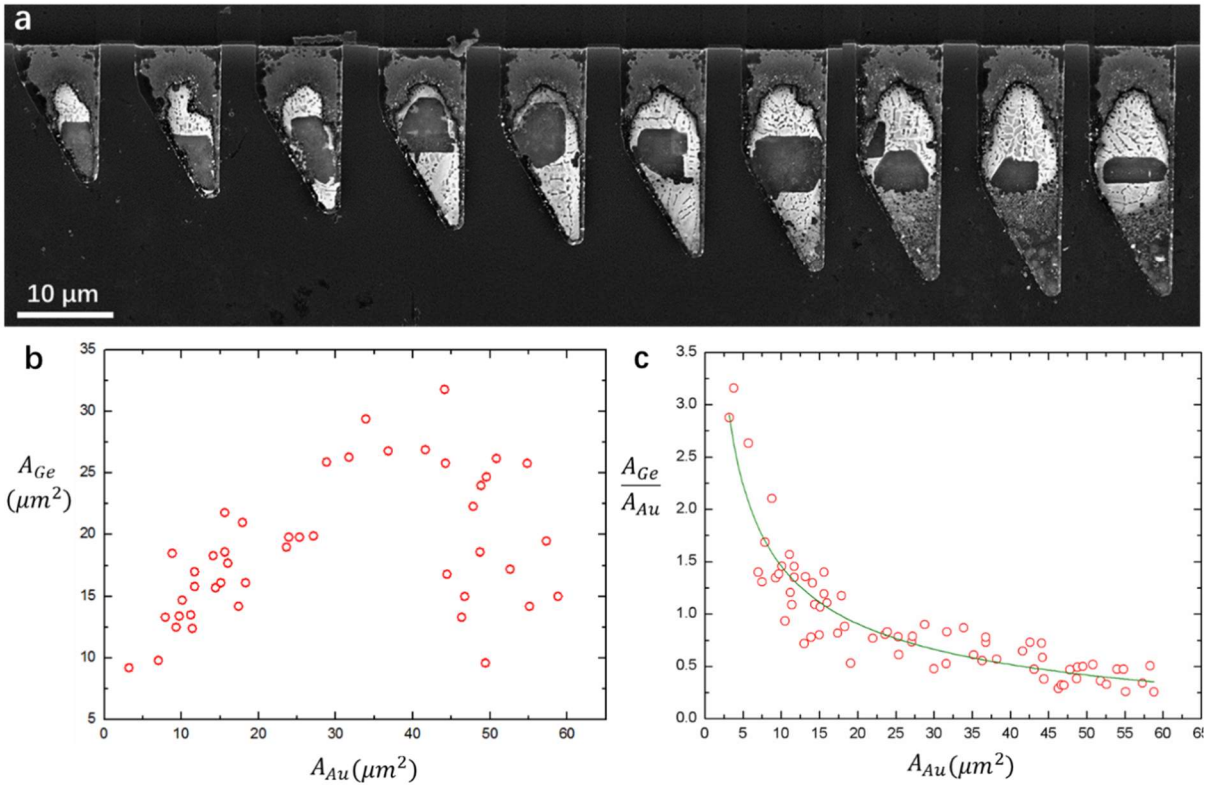

Figure 8-4. (a) SEM micrographs of laterally grown Ge(Si) films on Si in micro-crucibles of varying sizes; the films are grown at 375 °C, a reactor pressure of 40 mTorr and a total flow rate of 2500 sccm with a GeH_4 flow of 5 sccm for 1 hour. (b) The plot of the Ge film size versus the Au size. The Ge film size and the Au size are measured in plan-view SEM images. (c) The plot of A_{Ge}/A_{Au} ratio versus the Au size.

In addition, a simple mathematic model can help interpret the data shown in Figures 8-4b and 8-4c by assuming that the Ge flux is constant, and the film thickness is uniform. Here, the number of Ge atoms (N_{Ge}^c) in the films is given by the following equation:

$$N_{Ge}^c = F \cdot t \cdot A_{liquid-vapor} - c_0 \cdot N_A \cdot V_{Au} \quad (1)$$

where F is the GeH_4 flux, t is the growth time, $A_{liquid\text{-}vapor}$ is the area of the liquid-vapor interface. This first term is the total number of Ge atoms dissolved in the Au catalyst at the growth temperature. In Eq. 1 c_0 is the saturation concentration, N_A is Avogadro number and V_{Au} is the Au volume and this second term represents the number of Ge atoms required to saturate the Au catalyst. Thus, the number of atoms in the film is the total minus those atoms required to saturate the catalyst at the growth temperature. Next we can approximately establish the relationship between V_{Au} and $A_{liquid\text{-}vapor}$ using the below equation:

$$A_{liquid-vapor} = \alpha\sqrt{h}\cdot\sqrt{V_{Au}} \quad (2)$$

where α is the geometry factor depending on the shape of the Au in the plan-view image and h is the thickness of the film. Here, we are assuming that the Au catalysts have similar shape (e.g., similar triangle) and the film thickness is uniform; the area of the liquid-vapor interface in each micro-crucible is thus proportional to the square root of V_{Au} (see Appendix A). However, note that this is not true in every case. As shown in Figure 8-3a, the red dashed-line box highlights three micro-crucibles where the areas of the liquid-vapor interfaces are limited to the width of the micro-crucible channels and do not increase with the increasing amount of Au. In this study, it is a major error source. Then we combine equations (1) and (2) to obtain the following equation.

$$N_{Ge}^{c} = F\cdot t\cdot\alpha\sqrt{h}\cdot\sqrt{V_{Au}} - c_0\cdot N_A\cdot V_{Au} \quad (3)$$

As we can see from equation (3), a larger Au catalyst can absorb more Ge atoms due to the larger liquid-vapor interface (due to the increase in the first term as the square root of V_{Au}), but it would require a further increase in the number of Ge atoms to saturate the Au, (due to the increase in the second term linear with V_{Au}). Since the square root term initially increases faster than the linear term, we see a peak Ge(Si) film area. Thus, to grow a large-sized Ge(Si) crystal, medium-sized Au catalysts are required. Afterward, equation (3) can be manipulated to describe the relationship between A_{Ge}/A_{Au} and A_{Au}:

$$k\frac{A_{Ge}}{A_{Au}} = F\cdot t\cdot\alpha\cdot\frac{1}{\sqrt{A_{Au}}} - c_0\cdot N_A \quad (4)$$

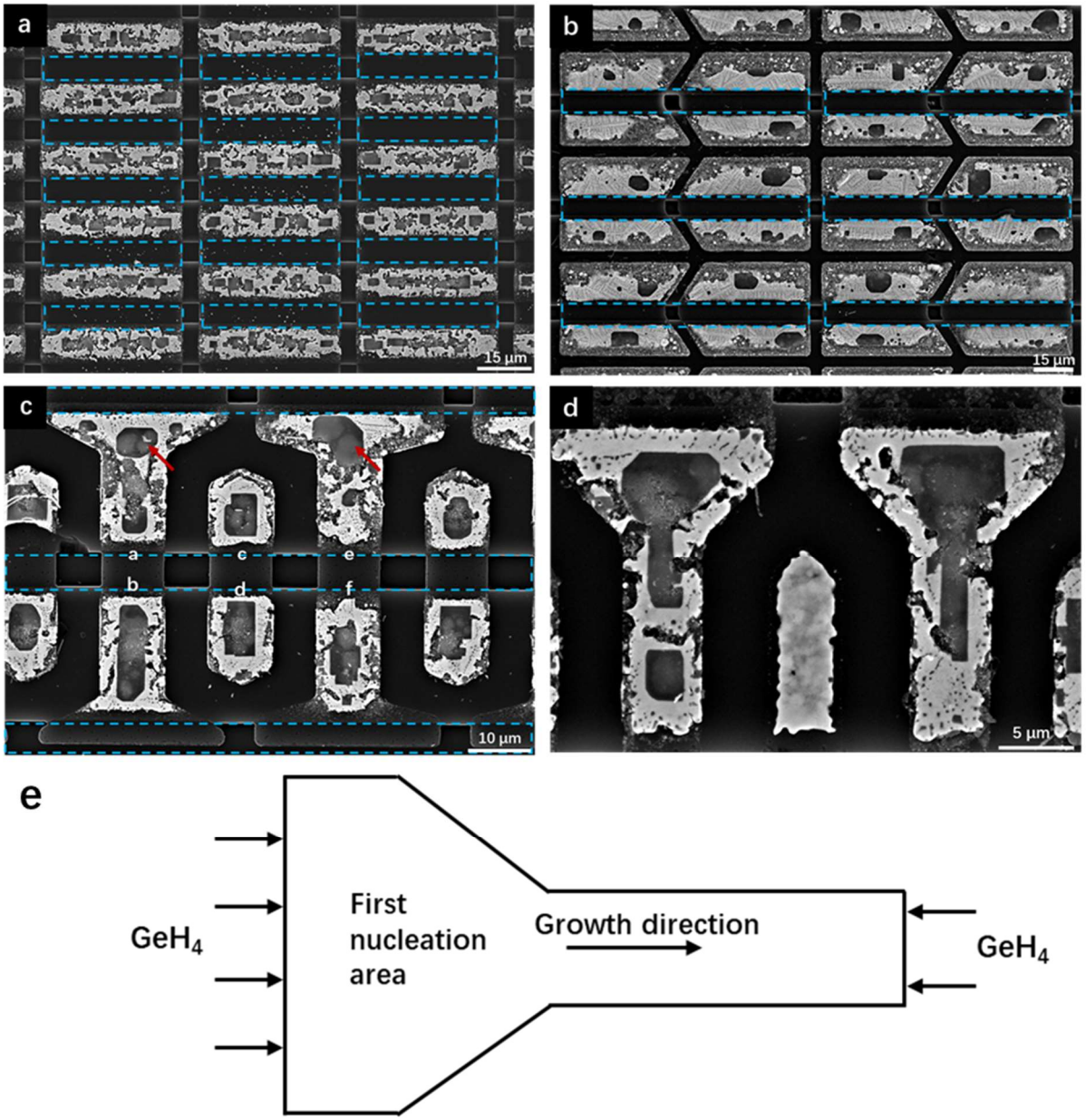

Figure 8-5. (a-d) SEM micrographs of micro-crucibles with different shapes; films were grown at 375 °C at a GeH_4 of 3 sccm for 2 hours, a reactor pressure of 40 mTorr and a total flow rate of 2500 sccm. The blue dashed-line boxes denote the openings for micro-crucibles and the red arrows in (c) highlight the preferential nucleation points. (e) Schematic diagram of an asymmetric, two-opening micro-crucible showing the preferential nucleation area and the growth direction.

Equation (3) is consistent with the trend shown in Figure 8-4b and may explain the correlation between the film size and the Au size in plan-view SEM images. Furthermore, Eq. 4 can be used to fit the data points in Figure 8-4c (the green curve); then we can estimate the saturation concentration of Ge (atomic percent content in the liquid) from this equation (21% from the fitting curve). Together these results provide important insights into the growth process and

may help to engineer the film growth.

The results obtained from the analysis of the Au geometric shape suggests that a large Au-vapor interface is beneficial to increasing the size of the Ge(Si) films. This idea allows us to design a rectangular micro-crucible with one or two longer side(s) having exposure to GeH_4 (Figures 8-5 a and 8-5b with two and one side(s), respectively). However, as can be seen from Figure 8-5a, numerous small Ge(Si) films were grown in each Au catalyst which suggests that the Ge atoms were rapidly absorbed by the narrow, two-opening micro-crucibles, reaching supersaturation in the liquid quickly and causing many nucleation points. This morphology is similar to that observed by LeBoeuf *et al*.[98] when a high growth rate was used. As mentioned above, the ideal way to laterally grow Ge(Si) films is to nucleate a crystal seed at one specific point so that it can help control growth. Hence, a single-opening micro-crucible shown in Figure 8-5b is employed to reduce the absorption of Ge precursors, and many of these micro-crucibles successfully demonstrate single film growth in each micro-crucible. Unfortunately, these micro-crucibles are not perfect because the nucleation points in Figure 8-5b are randomly distributed. To help predefine the nucleation site and better engineer the growth, a two-opening micro-crucible was designed to have one opening wider than the other one (Figures 8-5c and 8-5d). In Figure 8-5c, the micro-crucibles labeled a and e are two-opening micro-crucibles with asymmetric sides (the Au surface in one opening is much larger than the other); while micro-crucibles b and f are approximately symmetric, two-opening micro-crucibles; and finally, micro-crucibles c and d are single-opening micro-crucibles. One notable observation for micro-crucibles a and e is the trend to nucleate large crystals near the wider openings (highlighted by the red arrows in Figure 8-5c); such preferential nucleation is observed in most of micro-crucibles of this shape. This is probably because the wider openings absorb more Ge atoms to increase the Ge concentration locally near the openings, which make it easier to reach Ge supersaturation in the liquid, but not too much to cause many nucleation points. The two-opening, asymmetric micro-crucible is therefore promising to enable first nucleation at a predefine region (Figure 8-5e), realizing the lateral growth in a more controlled way. As shown in Figure 8-5d, it is observed that the films could nucleate in the upper (wider) areas and then

grew downward into the narrower parts in some of this kind of micro-crucibles. By contrast, symmetric, two-opening micro-crucibles b and f in Figure 8-5c show no sign to preferentially nucleate crystals at a specific point.

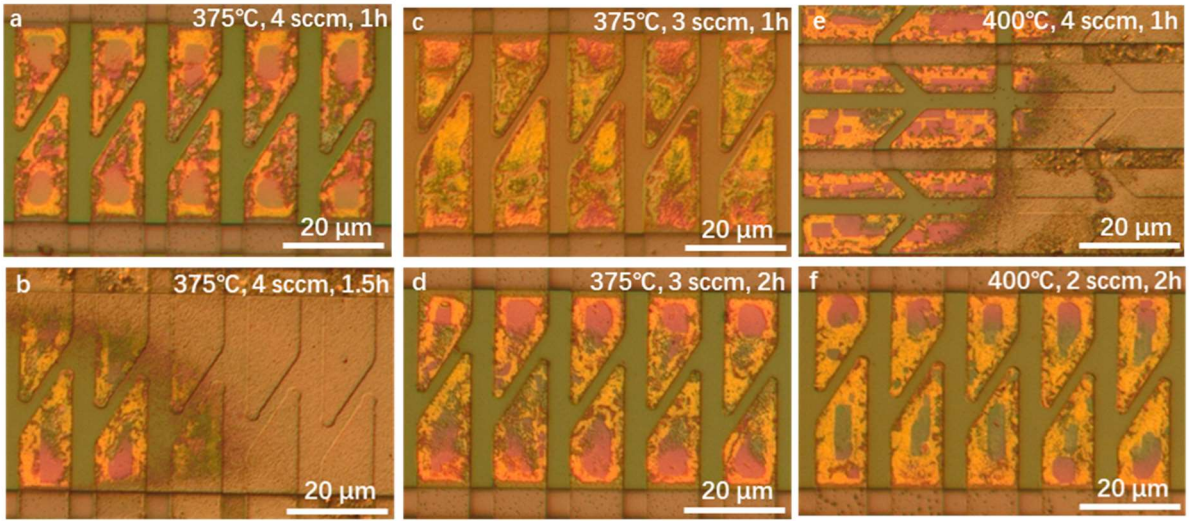

Figure 8-6. (a-f) Plan-view optical micrographs of laterally grown Ge(Si) films on Si. The films were grown at a reactor pressure of 40 mTorr and a total flow rate of 2500 sccm. The growth variables are the temperature, the GeH_4 flow rate and the growth time.

Figures 8-6 a-f show plan-view optical images of the micro-crucibles after CVD growths under different growth conditions. In these figures, Ge(Si) crystals of different sizes were observed surrounded by the yellow-colored Au. The Ge(Si) crystals are grey-blue in Figure 8-6a but their color in the optical images depends on the thickness of the capping layers and can be grey, purple or green. In our experiments, since the reactor pressure and the total flow rate remained unchanged, the growth rate was primarily controlled by the GeH_4 flow rate and the growth temperature. First, it is worth noting that a high growth rate leads to significant uncatalyzed, polycrystalline Ge crystals (standard vapor-solid (VS) growth) on the Si substrate and the capping layers, as can be seen by the brown textured growth on the right side of Figures 8-6 b and 8-6e. Figure 8-7 presents three types of growth (VLS, VS on Si and VS on the capping layers) that can occur in the growth process. Under high growth rate, the GeH_4 precursors can crack on the Si substrate and the amorphous encapsulation layers. Owing to the large GeH_4 flux, the Ge atoms can form small clusters before they diffuse to the Au catalyst, which leads to VS growth of polycrystalline or amorphous Ge. It can thus be suggested that a relatively low growth rate is necessary to grow the Ge(Si) films by only the catalyzed reaction. This is

important because the catalyzed reaction is the only desired growth to enable laterally grown films. Taking the growth temperature, GeH_4 flow rate and the growth time as the variable parameters, the growth conditions were investigated. Figure 8-6a shows the Ge(Si) films grown at 375 ℃ and at a GeH_4 flow rate of 4 sccm for 1 hour. Faceted Ge(Si) films were observed near the openings of the micro-crucibles and the uncatalyzed growth was negligible in this optical image. However, uncatalyzed Ge growth appeared on the capping layers after 1.5-hour growth under the same conditions (as can be seen in the textured brownish region in Figure 8-6b). Since the growth time is less likely to affect the growth rates, it suggests that under this growth condition (Figures 8-6a and 8-6b) the uncatalyzed Ge crystals were always present but were grown at a fairly low growth rate. At 375 ℃, a lower GeH_4 flow rate of 3 sccm was employed to eliminate or reduce the uncatalyzed growth. Unfortunately, it also dramatically reduced the yield (percentage of micro-crucibles with Ge(Si) films) as can be seen in Figure 8-6c. The yield of the Ge(Si) films could be boosted without growing polycrystalline Ge by increasing the growth time to 2 hours (Figure 8-6d). The results obtained from Figures 8-6 c and d indicate that under this condition the growth rate of crystalline Ge(Si) is low and the uncatalyzed growth might not be present. As can be seen from the Figure 8-6e, increasing the temperature to 400 ℃ leads to more uncatalyzed growth and is probably equivalent to increasing GeH_4 gas flow. At 400 ℃, a low flow rate of 2 sccm was used to suppress the uncatalyzed Ge growth and a 2-hour growth time was used to enhance the yield (Figure 8-6f).

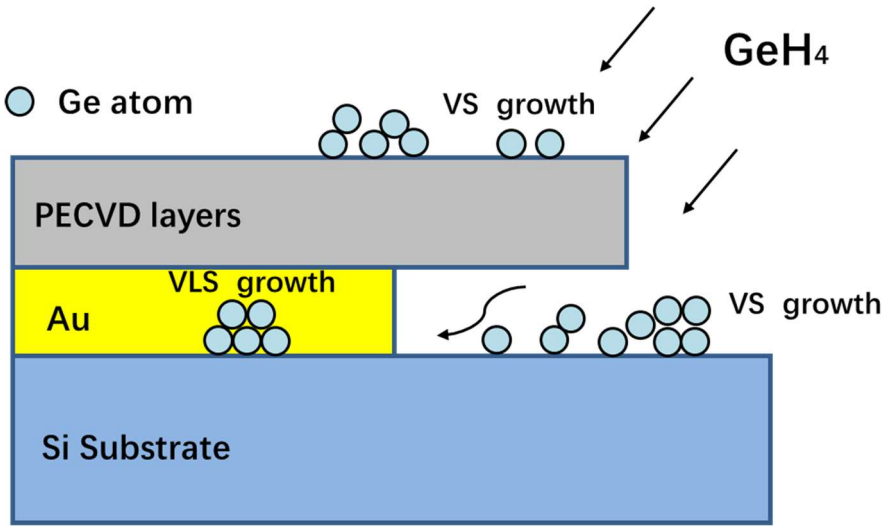

Figure 8-7. Schematic diagram of three types of growths (VLS, VS on Si and VS on amorphous) that may occur in the metal-catalyzed, lateral growth process.

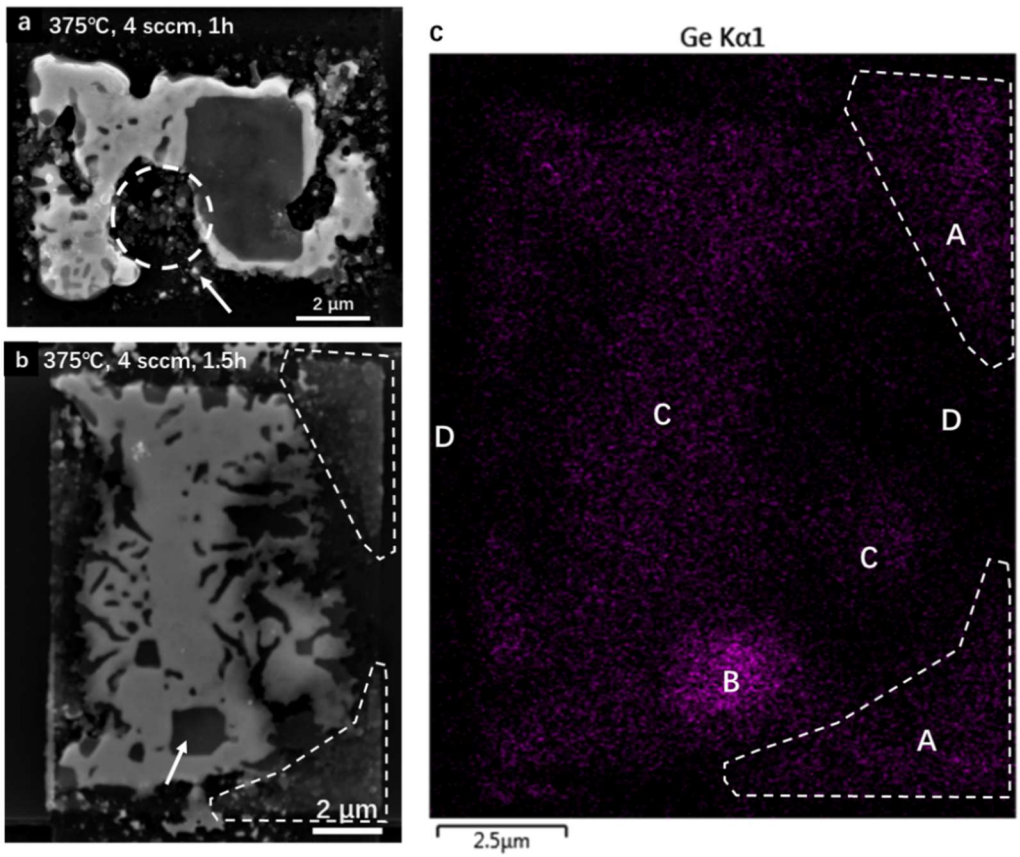

Figure 8-8. (a) and (b) SEM micrographs of laterally grown Ge(Si) films on Si; films were at 375 °C, a reactor pressure of 40 mTorr and a total flow rate of 2500 sccm with a GeH_4 flow of 5 sccm for 1 hour and 1.5 hours (a) the arrow shows the Ge nanowire growths catalyzed by small Au particles, and the circle highlights the Au agglomeration area, (b) the dashed lines indicate the uncatalyzed poly-Ge growths on Si and the arrow points to a VLS film growth. (c) The EDS mapping of Ge from the area corresponding to the micro-crucible in Figure 8-8b. The mapping image is divided into four different regions. A: uncatalyzed growth area. B: VLS growth area. C: Au-Si-Ge alloy. D: Si substrate.

Figures 8-8a and b show SEM micrographs of laterally grown Ge(Si) films on Si grown at the same deposition rate but different growth times. In Figure 8-8a, a faceted Ge(Si) thin film was surrounded by Au; an observation of this image is the agglomeration of Au, which can be seen from the blank area on the right side of the Ge(Si) film. The initial Au film covered this area as well as the circle area in Figure 8-8a. However, the Au-Si liquid agglomerates at 375 °C and reduces its film coverage area in plan-view SEM. More importantly, as shown in Figure 8-8a by the arrow, the Au agglomeration might induce the formations of Au particles or Au islands which catalyzed the growth of Ge nanowires. In Figure 8-8b, as highlighted by the white arrow, the Ge(Si) film that was grown for longer time shows similar morphology, but more uncatalyzed Ge crystals were found on the Si substrate as shown in the area highlighted by the

dashed zones in Figure 8-8b. Figure 8-8c shows the EDS Ge composition map from the area corresponding to the micro-crucible in Figure 8-8b, and the image was divided into four different regions which represent the uncatalyzed growth on Si (labelled as A), the VLS growth (B), the Au-Si-Ge metal alloy (C) and the Si substrate (D). The Ge EDS signal from the region A confirms the existence of the Ge uncatalyzed growths that are shown in the dashed zones in Figure 8-8b. Even though the uncatalyzed growth areas appear to be brighter compare to the VLS growth film (highlighted by the arrow) in the secondary electron imaging (Figure 8-8b) perhaps caused by characteristic uncatalyzed film roughness (Figures 8-6b and e), the catalyzed growth film (B) demonstrated stronger EDS signal, which means the catalyzed growth film is probably thicker. Additionally, Ge was found to be almost uniformly distributed in the metal alloy (C) and much less Ge signals were detected from the bare Si substrate (D).

8.2. Conclusions

Chapter 8 has discussed the effects of the Au catalysts and the growth rate on the Ge(Si) films which grew laterally on Si. In the annealing process, the Si substrate was etched and dissolved into the Au catalyst to form a liquid. The liquid tended to agglomerate on Si, pushing up the PECVD layers and locally increasing the film thickness. More importantly, it has been found that the Au size affects the final film size: a large Au catalyst tends to absorb more Ge because of its larger vapor-liquid interface but it also requires more Ge to saturate the Au. Therefore, the general trend is that under a certain growth condition the film size increases as the Au size increases, then plateaus and finally decreases. In this chapter, a simple model was designed to predict the final size of the films and estimate the Ge saturation concentration. Moreover, this chapter has discussed the different shapes of micro-crucibles; in particular, two-opening micro-crucibles with asymmetric sides are found to have potential to predetermine the first nucleation site and control the growth direction. Finally, a study with respect to the film growth rate is provided in Chapter 8. The study has shown that the growth rate can be increased by using a high temperature or high GeH_4 partial pressure. It has observed that high growth rate can help to enlarge the size of the films but also lead to more uncatalyzed Ge growth on Si. It is therefore suggested that a relatively lower growth rate and a longer growth time should be used to reduce

the uncatalyzed growth and increase the film size.

The findings in Chapter 8 provide valuable information for the engineering of metal-catalyzed, lateral epitaxial growth. First, the investigation of the Au catalysts has shown that a large vapor-liquid interface can absorb more GeH_4 and increase the local Ge concentration more rapidly compared to a smaller one. This find is important because it can help to design a micro-crucible that allows for large film growth and preferential nucleation near the opening by using a large vapor-liquid interface. Additionally, it is preferable to use a medium-size catalyst, since Ge can rapidly saturate a smaller one, resulting in undesirable multiple crystal growths, and may not be able to saturate a larger one to nucleate any crystals. Furthermore, a relatively lower growth rate is useful to realize single film growth in a micro-crucible because it allows Ge to diffuse to the predefined site to grow. On the other hand, Ge may nucleate everywhere in the micro-crucible under a high growth rate. Taken together, these results suggest that a well-designed micro-crucible and an appropriate growth rate are the keys to enable single and large film growth in a metal-catalyzed, lateral epitaxial growth process.

Chapter 9

Laterally Grown Ge Films on Si Using New Relaxation Mechanism

Chapter 9 provides a deeper insight into lateral epitaxial growth, discussing on a new relaxation mechanism to relieve the strain at the Si/Ge interface. It has been hypothesized that the initial growth section of a film is relaxed via the formation of dislocation loops while the subsequent lateral overgrowths use new relaxation mechanism since the film's sidewalls instead of the film surface are used as the growth fronts. In this chapter, firstly, we found a way to identify the first-to-nucleate areas within some micro-crucibles in SEM. Then, TEM and XRD were

performed to study the dislocation morphologies and the strain states of the films. In the end, we hypothesized a relaxation mechanism that might be present to relax the films during the lateral growth process. The growth results were characterized by a Hitachi SU-3500 Variable Pressure Scanning Electron Microscopy, a FEI Tecnai TF20 Transmission Electron Microscope, and a Bruker D8 X-ray diffraction system.

9.1. Results and Discussion

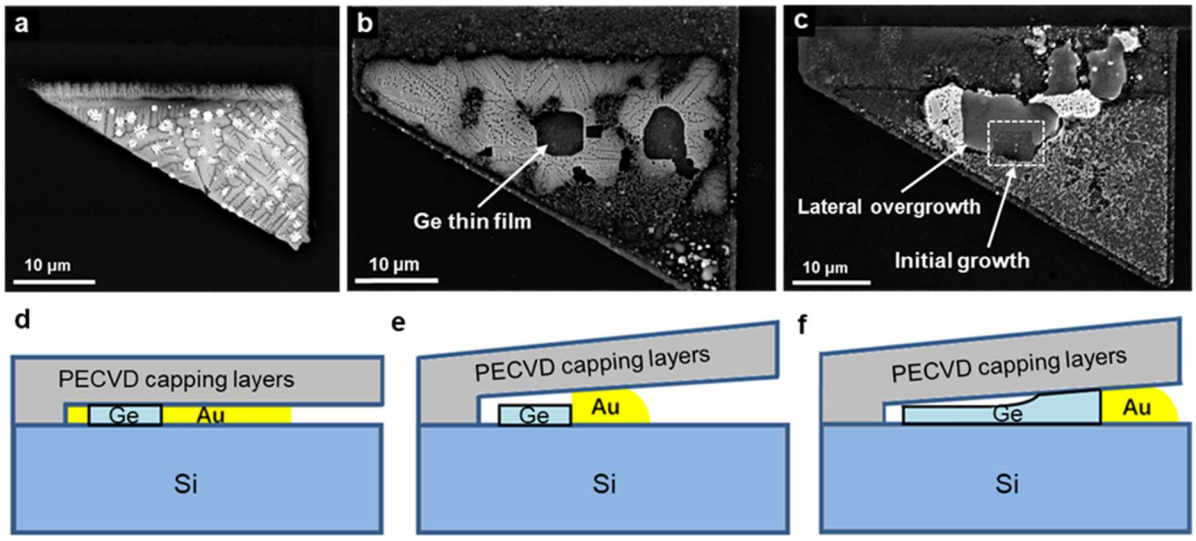

Figure 9-1. SEM micrographs of Ge(Si) films that were grown in the micro-crucibles which have been removed to clearly image the microstructure and schematic representation of the agglomeration of Au on Si which leads to thicker Ge(Si) film growth. (a) Triangular Au-Si eutectic structure without Ge film growth and Au agglomeration. (b-c) Ge(Si) films grew at 375 °C and a GeH_4 flow rate of 5 sccm for 60 min. (d-f) Cross-sectional schematic of the agglomeration of Au.

Figures 9-1 a-c present plan-view SEM micrographs of three different micro-crucibles to review the growth process. Figure 9-1a shows a triangular Au structure that has been annealed on Si with little exposure to GeH_4. Therefore, this is thought to be a no-growth micro-crucible where the Au film almost remains its original shape and only the Au-Si eutectic structure can be observed. On the other hand, in Figures 9-1b and 9-1c, Ge(Si) films (surrounded by the brighter contrast Au in Figure 9-1b or having a lighter gray contrast in Figure 9-1c and indicated by the arrows) start to appear in micro-crucibles after a 60-min growth. We see that the Au agglomerates in Figures 9-1 b and c from the fact that there is less Au in the micro-crucible tip (right bottom corners) compared to Figure 9-1a. Figure 9-1c demonstrates the strongest Au

agglomeration and shows a brighter-contrast (Ge(Si) film), lateral overgrowth extended from the initial rectangular shape (highlighted in Figure 9-1c). As discussed in chapter 8, the brighter contrast is a result of an increased Ge(Si) film thickness. The brighter contrast is because of a thicker Ge(Si) film; the increased thickness is observable by SEM, because more of the electrons are backscattered due to the higher Z number of Ge compared to Si. We therefore suspect that the Au agglomeration deforms the capping layers as is illustrated in Figures 9-1 d-f. The capping layer deformation can result in both thicker Au and a thicker Ge(Si) film (Figure 9-1f). This observation is important because it can be used to identify the first-to-nucleate areas within some micro-crucibles in plan-view SEM since the bright-contrast, lateral overgrowth is readily distinguished from the dark-contrast, initial growth.

Figure 9-2a shows a laterally grown Ge(Si) film with an initial growth area noted as rectangle #1 and a thicker Ge(Si) film surrounding rectangle #1 on 3 sides. A TEM sample was prepared using a Focused Ion Beam (FIB) along the dashed line in Figure 9-2a; note that the dashed line includes part of rectangle #1 as well as some of the thicker Ge(Si) film surrounding it. Part of the cross-section corresponding to the rectangle #1 in Figure 9-2a is shown in the TEM micrographs in Figure 9-2b. The reason why we think rectangle #1 as the first nucleation crystal is because of its dark contrast in SEM; as mention earlier, the initial growth areas should have a thinner thickness (dark contrast) whereas the later Au agglomeration could increase the Ge(Si) thickness as the capping layers were deformed. Further evidence supporting that rectangle #1 grew first can be seen in Figure 9-2b; the arrow in Figure 9-2b notes the beginning of lateral growth on top of rectangle #1 which grew on top of rectangle #1 in the direction of the arrow. The start of the lateral growth on top of rectangle #1 can be seen at the lower intersection of the dashed line and the dashed rectangle in Figure 9-2a.

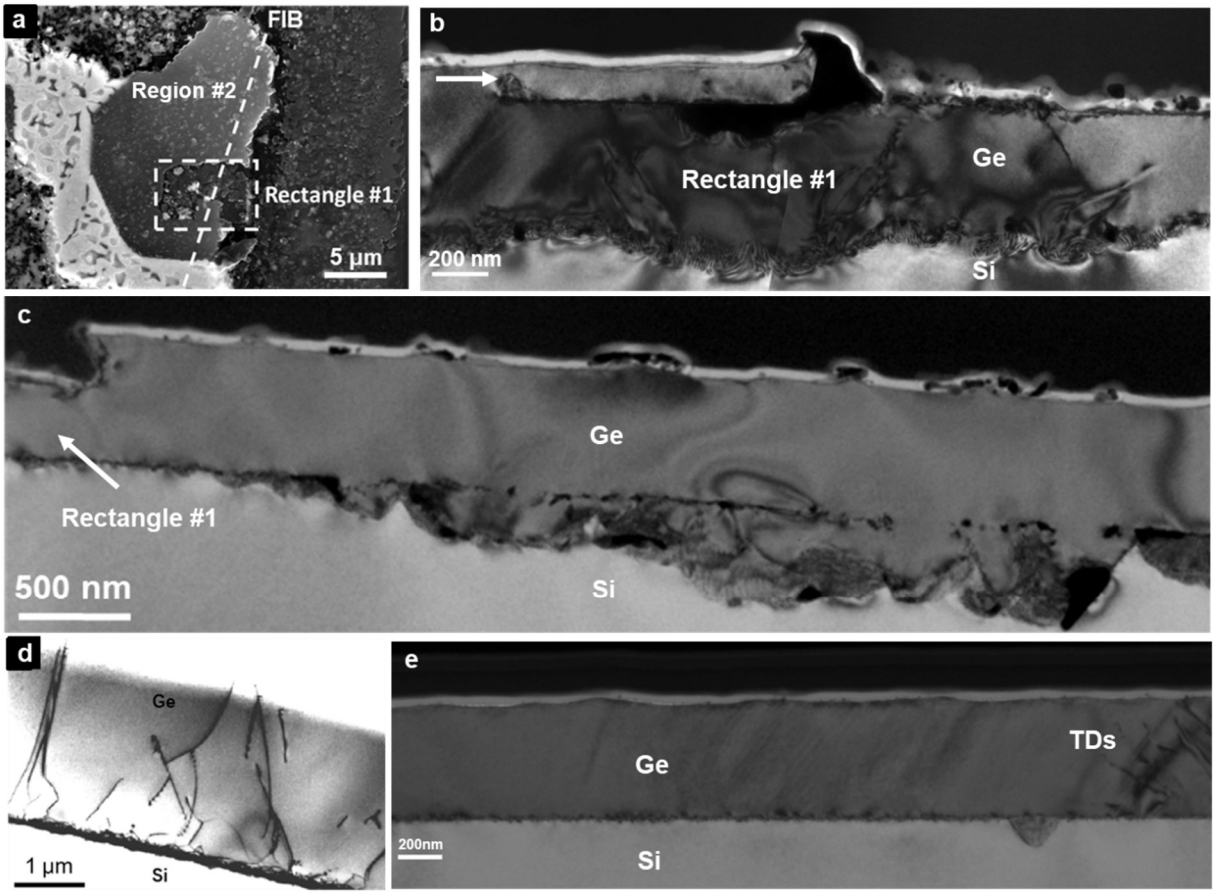

Figure 9-2. (a) Plan-view SEM micrograph of the Ge(Si) thin film on Si. Ge(Si) films grew at 375 °C and a GeH_4 flow rate of 5 sccm for 60 min. (b) and (c) Cross-sectional TEM micrographs under a g = <220> beam taken through the dashed line (FIB plane) in Figure 3a, rectangle #1 and region #2, respectively. (d) Cross-sectional TEM micrograph of a Ge film grown vertically on Si (planar film growth of Ge on Si)[99]. (e) Cross-sectional TEM micrograph of Ge film grown laterally on Si with a flat Ge-Si interface under a g = <220> beam.

Figure 9-2a shows a laterally grown Ge film with an initial growth area noted as rectangle #1 and a thicker Ge film surrounding rectangle #1 on 3 sides; the upper part of the thicker film in Figure 9-2a is noted as region #2. A cross-sectional TEM sample was prepared using a Focused Ion Beam (FIB) along the dashed line in Figure 9-2a, which includes part of rectangle #1 as well as some of the thicker Ge film surrounding it, like region #2. Part of the cross-section corresponding to rectangle #1 in Figure 9-2a is shown in the TEM micrograph in Figure 9-2b. As discussed earlier, part of rectangle #1 includes a first-to-nucleate area because of its darker contrast in SEM. Further evidence supporting that rectangle #1 grew first can be seen in Figure 9-2b; the arrow in Figure 9-2b notes the beginning of lateral Ge growth on top of rectangle #1in the direction of the arrow. The start of the lateral growth on top of rectangle #1 can be

seen at the lower intersection of the dashed line and the dashed rectangle in Figure 9-2a.

The dislocation morphology in rectangle #1 (Figure 9-2b) is similar to that of planar film growth of Ge on Si with numerous dislocations including a couple of TDs intercepting the film surface. From a mechanistic point of view, we would expect the first Ge growth to nucleate on the Si substrate and thus the first part of the film will grow in a planar fashion. Owing to the strain induced by the lattice mismatch between the Si substrate and Ge(Si) film, beyond a critical thickness (< 10 nm for a Ge concentration higher than 50%)[15], dislocation loops nucleate from the surface and generate a high-density of TDs in rectangle #1. After reaching the capping layers, the film grew laterally on Si because the capping layers inhibited vertical growth.

Part of the film in Figure 9-2b grew laterally above rectangle #1 highlighted by the arrow suggesting the promise of lateral growth since the dislocations and defects originating in rectangle #1 are stopped at the interface between rectangle #1 and the lateral overgrowth region. More importantly, the lateral overgrowth areas (region #2) around rectangle #1 demonstrate defect-free growth with a width of a few microns in cross-sectional TEM (Figure 9-2c), a surprising and fortuitous result given the ~ 4% lattice mismatch. This result contrasts with planar Ge film growth on Si, Figure 9-2d, which shows much more TDs in cross-sectional TEM. Figure 9-2e further shows the promise of lateral growth; on the right, a highly defective area can be seen in the Ge(Si) and is probably a first-to-nucleate area. However, the following lateral growth shows a defect-free area on a flat Si-Ge interface. It should be noted that it also contrasts with the high-quality Ge film growth on the rough Si-Ge interface as shown in Figure 9-2c. This result shows that this growth technique can be used to grow low TDD films on both rough and flat surfaces.

Furthermore, Figures 9-3a and b show plan-view TEM micrographs of a rectangular Ge(Si) thin film under a g = $<2\bar{2}0>$ beam and a g = <220> beam. It can be seen from the figures that a couple of TDs denoted by the black arrows are present in a certain region, which is likely to be a first-to-nucleate area. Importantly, apart from this small region, the lateral overgrowth

areas demonstrate high quality, less defective surface. By contrast, planar Ge film grown on Si typically generates numerous threading dislocations with a density up to more than $10^9/cm^2$, which means at least ~ 36 dislocations should be found in the film as shown in Figure 9-3a.

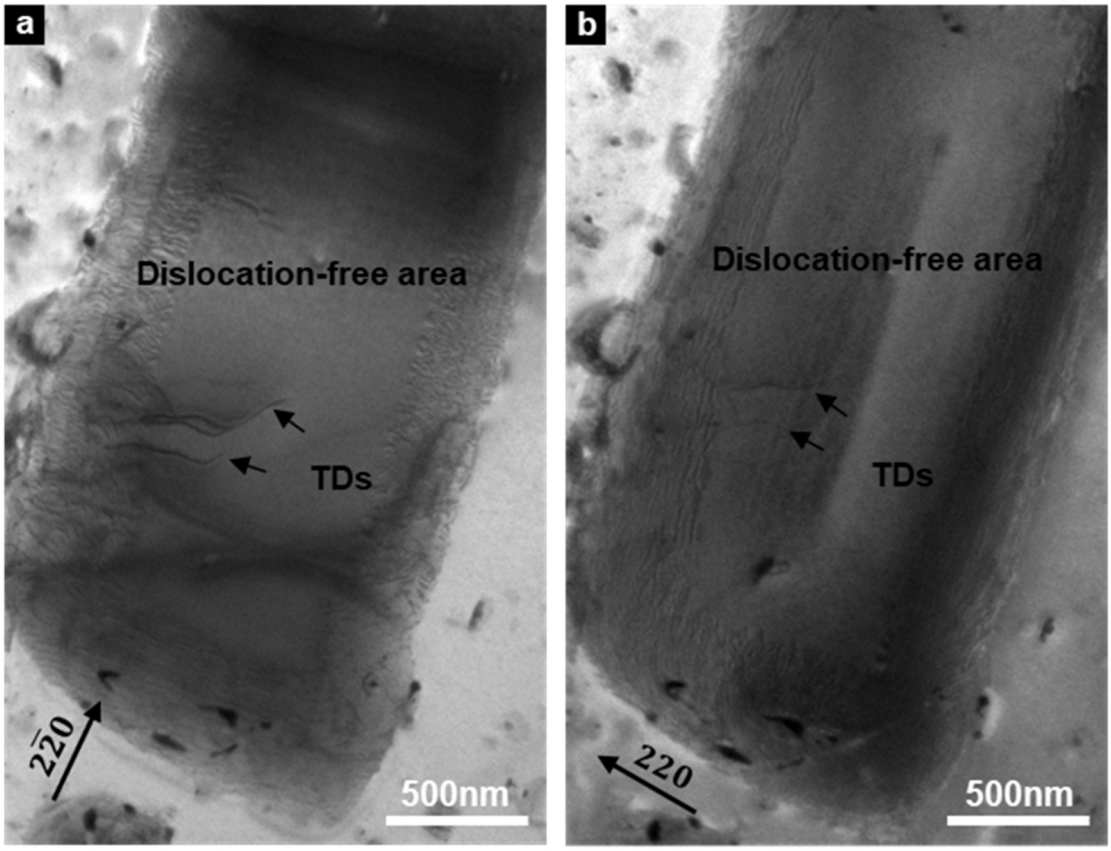

Figure 9-3. Plan-view TEM micrographs of a Ge(Si) thin film on Si under a g = <$2\bar{2}0$> beam (a) and g = <220> beam (b). The film was grown at 500 °C with a GeH_4 flow rate of 4 sccm for 60 min.

In order to access whether the films are relaxed or not, the composition and the strain states of the films were investigated. High-Resolution Transmission Electron Microscopy (HRTEM) was used to characterize the films at the atomic level (Figure 7-6). In HRTEM micrographs, MDs were observed at the interface to relax the films. Furthermore, we counted the number of the lattice planes on the both sides of the Ge(Si)/Si interface. An extra Si plane was found in every ~25 Si lattice planes (hundreds of lattice planes). It suggests that the lattice mismatch between the growth layer and the Si substrate is ~4% and relaxed by dislocations (the Si/Ge lattice mismatch is 4%).

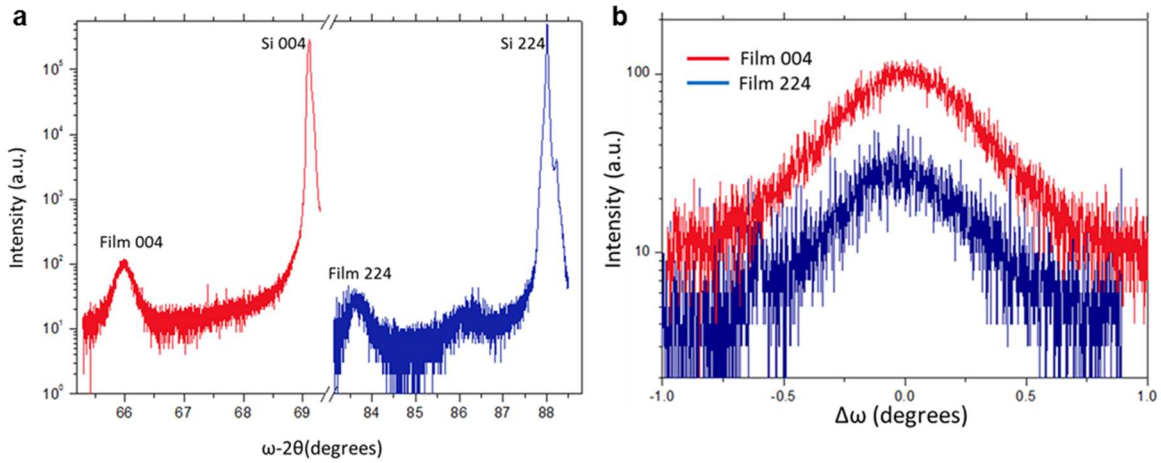

Figure 9-4. (a) (004) and (224) Omega-2Theta scan of the Ge(Si) films. (films grew at 375 °C with a GeH_4 flow rate of 5 sccm for 60 min). (b) 004 and 224 Rocking curves of the Ge(Si) films plotted versus relative omega values.

However, the results from HRTEM cannot provide global information with respect to the composition and strain states of the films. To accomplish this, XRD was employed to measure the Si/Ge (004) and (224) reflections from a sample. The XRD signals were collected from a ~1 cm^2 area and averaged over many lateral films to measure the lattice constants of the films. The X-ray beam was aligned to Si (004), Si (224), film (004), and film (224) diffraction conditions. Figure 9-4a demonstrates the Omega-2Theta scans around the Si (004) and Si (224) reflections. Afterwards, as shown in Figure 9-4b, rocking curves of the films were depicted around the film (004) and film (224) reflections (the relative omega values were calculated from the Si peak positions). A perpendicular lattice constant of 5.6587 Å and an in-plane lattice constant of 5.6565 Å can be calculated from the XRD results and are related to a Ge concentration of ~99.98% and a strain of ~-0.02%. The results therefore suggest that the grown films are essentially fully relaxed and pure Ge. Furthermore, there might be residual strain from thermal expansion mismatch between Ge and Si, which is estimated to be ~-0.1% for growth temperature at 375 °C. However, the thermal mismatch strain is fairly small compared to the 4% lattice mismatch.

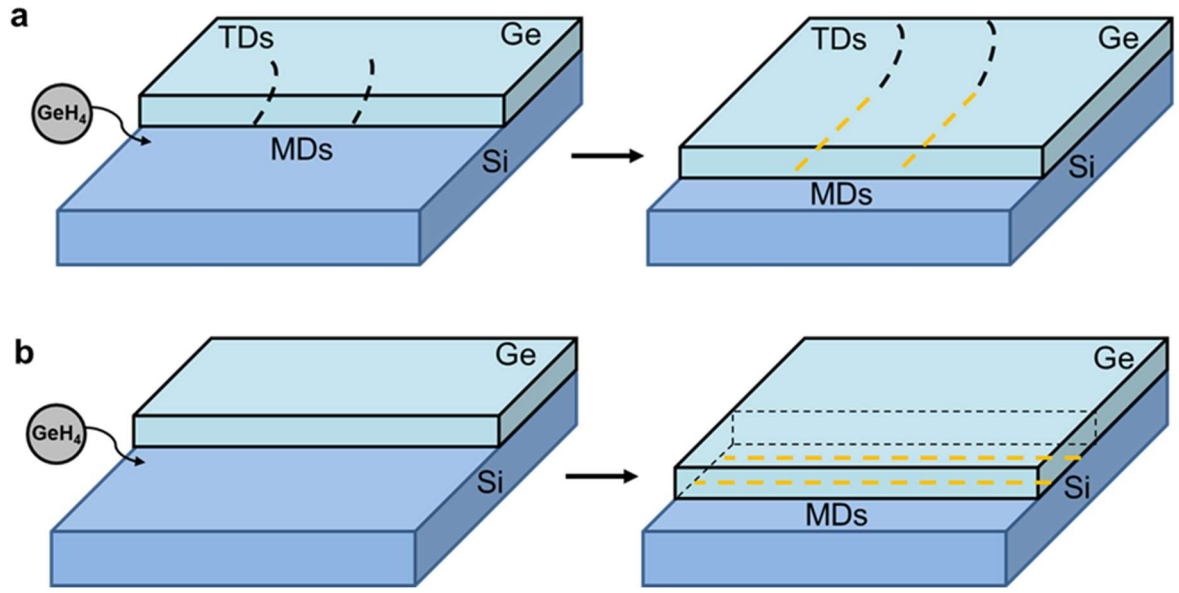

Figure 9-5. Schematic of the relaxation mechanism to suppress the generation of threading dislocations. (a) the preexisting misfit dislocations which are parallel to the growth direction are elongated to relax the films. (b) the growth front skips a lattice to nucleate misfit dislocations that perpendicular to the growth direction to relax the films.

In this study, there are two surprising results; first, the TEM micrographs show that lateral growth areas are of high-quality (low TDD) films and, second, the films are fully relaxed, both results occur despite the low growth temperature. Standard planar growth of Ge on Si involves the nucleation and glide of dislocations to relax the 4% lattice mismatch between the two materials; the nucleation of dislocations implies highly defective films, which is why the high-quality state of the lateral films is surprising. Dislocation glide is a thermally activated process and so, at these low temperatures (500 °C or less), dislocation glide is greatly impeded and should result in strained films[48], which is why the fully relaxed nature of our laterally grown Ge(Si) on Si is surprising. Given these surprising results we propose a new relaxation mechanism which can allow for the direct growth of high-quality, relaxed, lattice-mismatched semiconductors. We suggest that lattice-mismatch strain can be relaxed by extending preexisting misfit dislocations (Figure 9-5a) and that lateral growth can "build in" 90° dislocations as it grows (Figure 9-5b).

In the first stage of the lateral growth, Ge(Si) islands (e.g. the rectangle #1) are selectively grown on Si at a high growth rate since the Ge supersaturation provides a large driving force

to nucleate the first growth. Note that high-density TDs and MDs are generated in the initial films because of the large lattice mismatch between the growth layer and the substrate. From these islands, lateral growth occurs and can extend existing dislocations, as depicted in Figure 9-5a. This can relax the films in one direction and could result in uniaxially strained films. However, since the films seem to be completely relaxed by XRD, relaxation is also required in other direction as well. This can occur by a process depicted in Figure 9-5b where lattice planes can be skipped as the film grows laterally (the large strain concentration at the film's edge may allow Ge atoms to attach to wrong Si atoms by skipping a Si lattice to nucleate a misfit dislocation); it is equivalent to dislocations nucleating from the edge every ~25 atomic spacings in order to relax the 4% lattice mismatch between Si and Ge. The same mechanism was reported to relieve the strain at the edge of Ge islands on Si[100]. Due to the new relaxation mechanism, the lateral growth process can suppress the nucleation of TDs on the thin films' surfaces.

9.2. Conclusions

The purpose of chapter 9 is to investigate on the relaxation mechanism that is used to relax the Ge(Si) films grown laterally on Si. This study has shown that the first-to-nucleate areas of the films demonstrates a dislocation morphology similar to that of planar Ge film growth on Si (high TDD) whereas the lateral overgrowth areas show substantially reduced TDD. The second major finding is that the films are nearly fully relaxed and pure Ge in spite of being grown at low temperatures. These results suggest that there is a new relaxation mechanism other than the nucleation of dislocation loops to relax the films. We hypothesize that the laterally grown films can extend the preexisting misfit dislocations or introduce 90° dislocations at the growth front to relieve the strain caused by lattice mismatch. In this chapter, the TEM and XRD results have been demonstrated to support this hypothesis, suggesting that Ge films with reduced TDD can be grown on Si by using metal-catalyzed, lateral epitaxial growth technique. This finding has important implications for semiconductor material integration on Si, e.g. Ge based multi-junction solar cells or InP-based lasers and detectors on Si, since the laterally grown films provide high-quality (low TDD) surfaces where defect-sensitive devices can be fabricated.

Chapter 10

TEM Studies of Ge Films Grown Laterally on Si

This chapter presents an in-depth study of a Ge(Si) films grown laterally on Si by using a FEI Tecnai TF20 Transmission Electron Microscope. In chapter 9, the first-to-nucleate areas and the laterally overgrowth areas of the films could be differentiated in SEM because of the film thickness difference; the dislocations in these two regions were characterized by cross-sectional TEM via the preparation of FIB samples. Chapter 10 analyzed the composition of the films and found that the first-to-nucleate areas of the films are Si-rich. The outlines of the first-to-nucleate areas could thus be delineated by EDS in plan-view TEM. Afterwards, TDD in the first-to-nucleate areas and the lateral overgrowth areas were obtained for comparison.

10.1. Results and Discussion

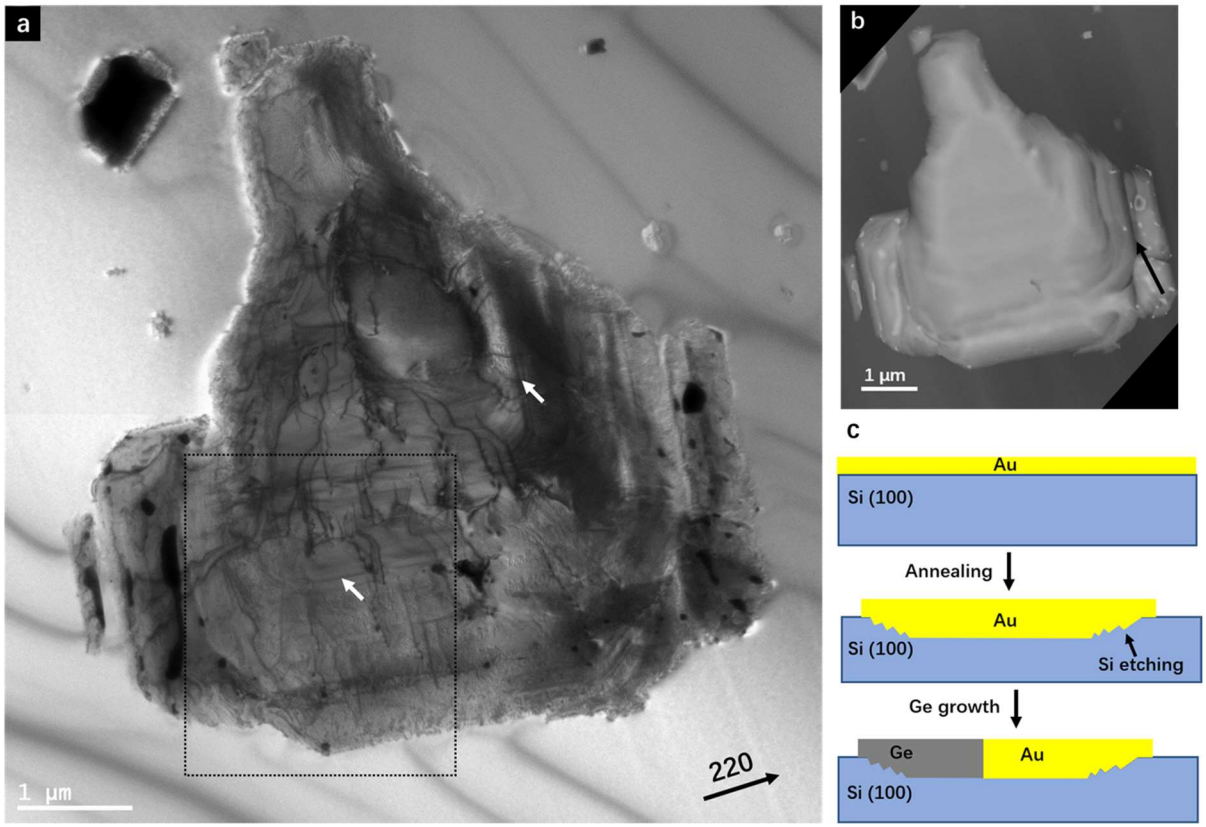

Figure 10-1. (a) Plan-view TEM micrograph of a laterally grown Ge(Si) thin film that was grown at 375°C under 220 diffraction condition. (b) HAADF image of the same film. (c) Schematic diagrams of the annealing process and the Ge CVD process in the side view. The schematics show the possible mechanism for the formation of sloping, rough Si-Ge(Si) interface.

Figure 10-1a shows a plan-view TEM micrograph showing the dislocation morphologies in a laterally grown Ge(Si) film under a 220 diffraction condition, while Figures 10-1b shows a high-angle annular dark-field (HAADF) image providing information on the composition and thickness of the film; a brighter contrast in the HAADF image is attributed to the presence of larger atomic number elements and/or it means that the local area is thicker (more atoms).It can be seen from the Figure 10-1b that the dark contrasts (highlighted by the black arrow) are visible near the edge of the film whereas the center of the film is more uniform and brighter. It is therefore suggested that there are composition or thickness variations near the dark-contrast areas.

From the HAADF image it is difficult to attribute meaning to this contrast, however, when

correlated with etching results (Figures 10-2b and 10-2c) we can attribute the primary origin of this contrast to be due to varying Ge(Si) thicknesses since the underlying Si substrate is etched (Si dissolved into Au during annealing process) and results in Ge(Si) film thickness variations schematically shown in Figure 10-1c. At a temperature higher than the Si-Au eutectic temperature, the Si substrate was etched by the Au liquid to form many etch pits (see chapter 8). For a large etch pit, its sidewalls are inclined with respect to the original Si substrate surface and consist of many small grooves due to the preferential etching along certain crystallographic orientations (Figure 10-1c and Figure 8-2c). Afterwards, Ge(Si) films were grown on these etch pits and the local thickness of the film varied according to the extent of the Si etching (deeper etching led to the thicker Ge(Si) film). Therefore, the dark contrast near the film's edge in Figure 10-1b may be attributed to the existence of Si while the Si in the center area was entirely etched by ion milling.

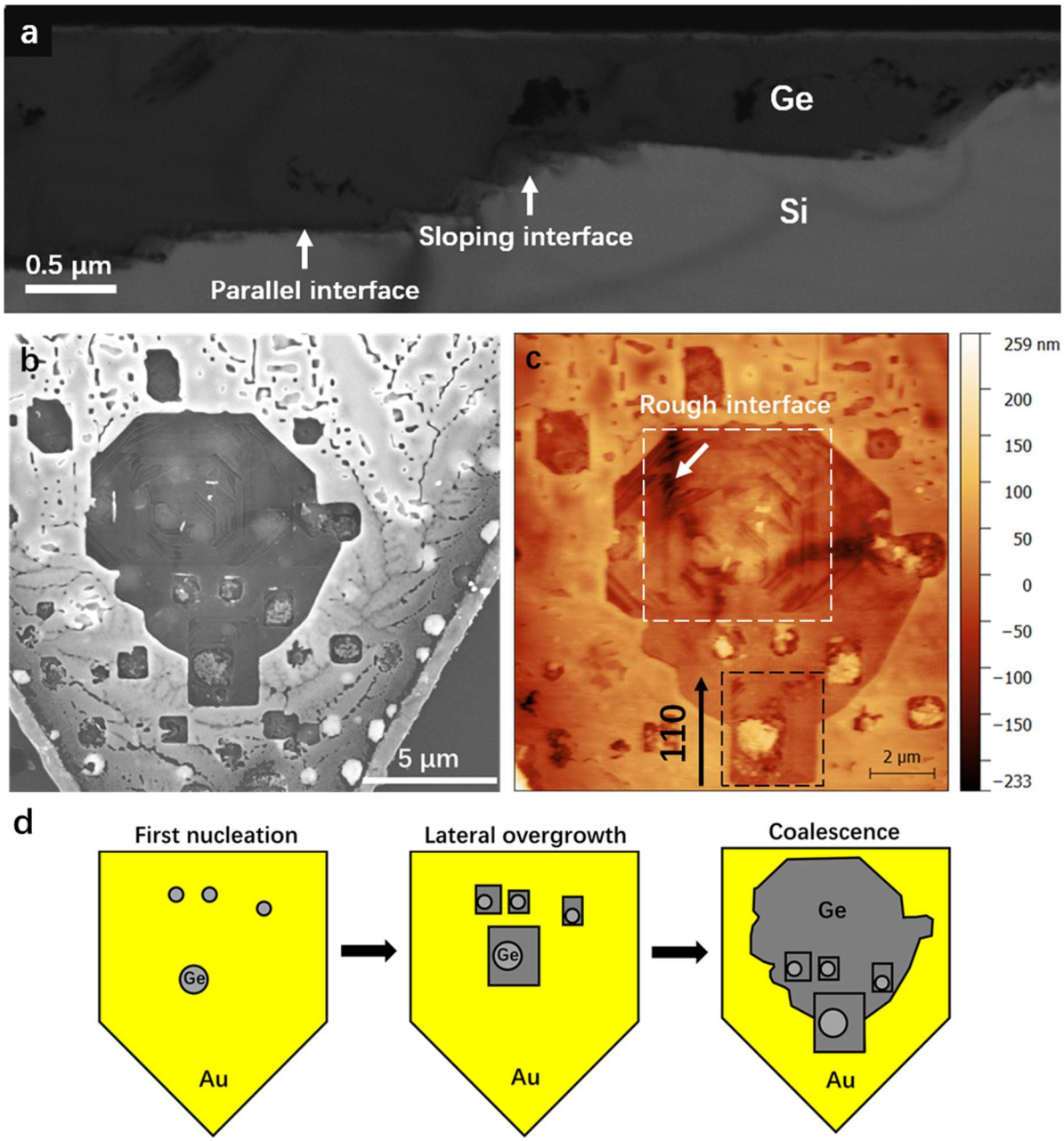

Figure 10-2. (a) Cross-sectional TEM micrograph showing the parallel interface and sloping interface underneath a laterally grown Ge(Si) film. (b) Plan-view SEM micrograph of a laterally grown Ge(Si) film after CrO_3-based wet etching. (c) AFM image of the area demonstrated in Figure 10-2b. The white arrow indicates the height variations possibly due to the steps in the sloping interface. The dashed-line box highlights a rectangular crystal that might be grown and extended from a first nucleation site.

Stronger evidences for the film thickness variations induced by the Si etching can be found in the cross-sectional TEM micrograph (Figure 10-2a) where rough and sloping interfaces are seen between the Ge(Si) film and the Si substrate. In addition, this micrograph shows how the interfaces change the local thickness of the film, which can generate contrasts in both HAADF and diffraction-contrast TEM micrographs. Furthermore, the flat interfaces that are parallel to

the original Si surface (in Figure 10-2a) are found to be connected to the sloping interfaces. Figure 10-2b shows a plan-view SEM image of a laterally grown Ge(Si) film after CrO_3-based wet etching; the chemical etching revealed an etching pattern within the film. This pattern could not be seen clearly in SEM, and the film was further characterized by AFM (Figure 10-2c). The white dashed box in Figure 10-2c highlights an area that may be a Si etch pit as a result of the dissolution of Si into Au. Furthermore, as indicated by the white arrow in Figure 10-2c, we observed black straight contrasts in the white dashed box that correspond to the etching pattern in Figure 10-2b. The darker contrasts in AFM suggest that the local areas are deeper and thus were etched more by the etchant. Since the CrO_3-based etchant is developed to selectively etch Ge or SiGe and less likely to etch the Si substrate, the observed contrasts in AFM suggest that the film thickness varies, especially near the edge of the Si etch pit (highlighted by the white dashed box in Figure 10-2c). The AFM results, therefore, provide additional evidence with respect to the rough Si-Ge(Si) interface. Interestingly, as highlighted by the white arrows in Figure 10-1a, contrasts with similar crystallographic orientations as that observed in AFM were observed in the diffraction-contrast TEM image as well. We believe that these fringes were also caused by the thickness variations of the film. Overall, these results support the view that rough Si-Ge(Si) interfaces can be present underneath the Ge(Si) film.

Besides, it should be noted that the composition of the film (Si and Ge contents) affects the chemical etching rate and also results in the height differences in AFM after the etching. As shown in Figure 10-2c, the dashed-line box highlights a rectangular crystal that is significantly thicker in the left center of the box area (brighter in AFM). In addition, three brighter-contrast spots can be observed above the rectangular crystal in Figure 10-2c, and the rest of the film demonstrates more uniform contrast. These contrasts are less likely to be caused by the film thickness variations. It can thus be suggested that there might be a few spots within the film that have a different chemical composition while the film composition is more uniform in the rest of the film. These spots are probably Si-rich since the CrO_3-based etchant was found to etch high Si content materials more slowly. Based on the AFM results, we hypothesize that the first crystal nucleus was Si-rich and grew laterally on Si with growth fronts parallel to <110> or $<1\bar{1}0>$ direction, and then coalesced with other first-to-nucleate areas to form the large film

(Figure 10-2d).

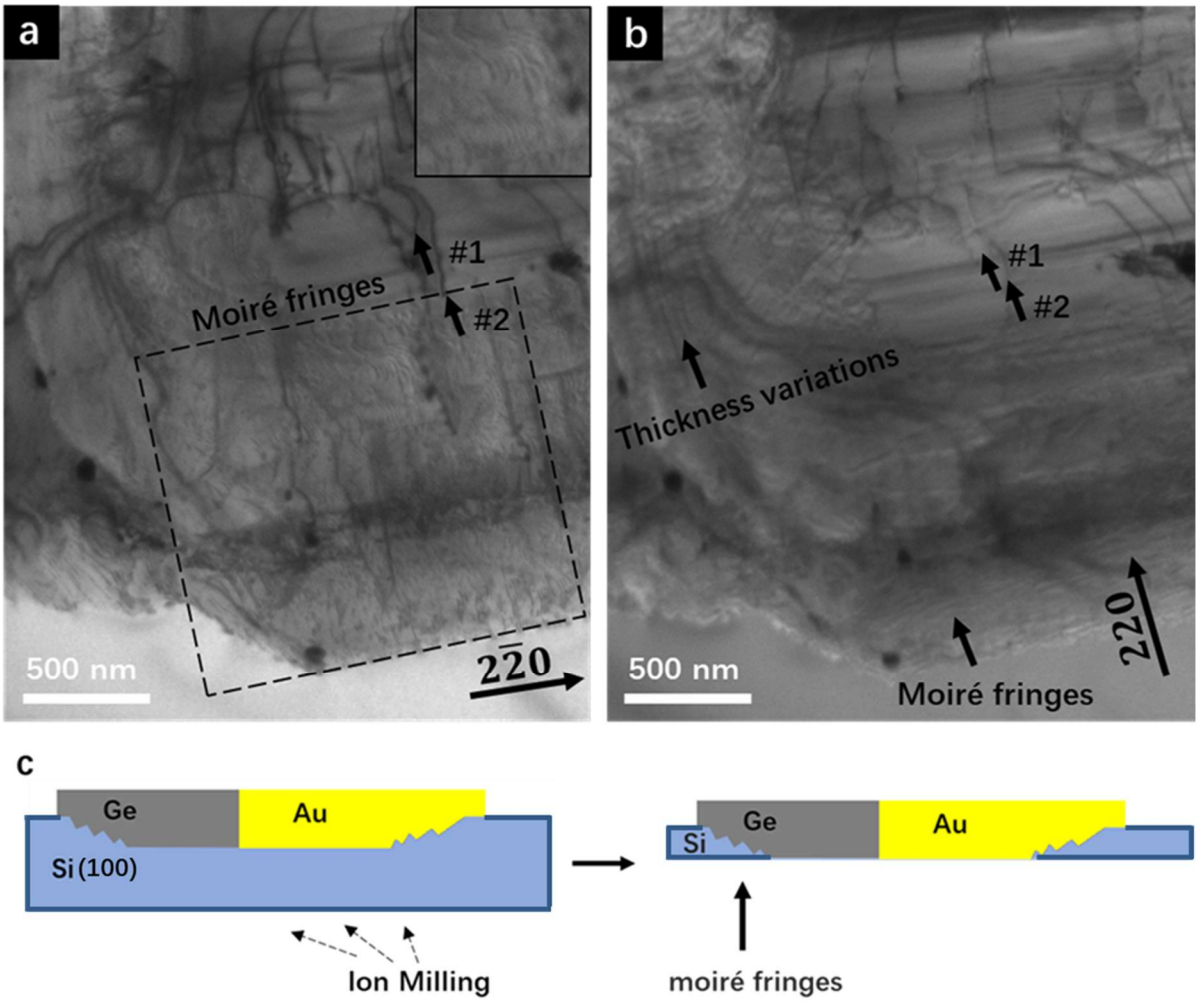

Figure 10-3. (a) and (b) Plan-view TEM micrograph of the area marked by the dashed-line box in Figure 10-1a under 2$\bar{2}$0 and 220 diffraction condition. The box in the top right corner of Figure 10-3a shows a magnified image of moiré fringes. (c) Schematic of the ion milling process and the overlap of Si and Ge(Si) that cause the moiré fringes.

Figures 10-3a and 10-3b show magnified TEM micrographs of the area marked by the dashed-line box in Figure 10-1a under a 2$\bar{2}$0 and 220 diffraction condition. In the upper part of these Figures, high-density dislocations can be seen, which may interact with each other to form dislocation pile-ups, located in the center of the film. In Figure 10-3a, two dislocations are highlighted by the black arrows and marked by #1 and #2 under 2-20 diffraction condition. In Figure 10-3b, dislocation #2 is still visible but shows a weaker contrast whereas dislocation #1 disappears under the 220 diffraction condition. It is probably due to the fact that dislocation #2 is a 60° dislocation and dislocation #1 is a 90° dislocation[101]. In Figure 10-3a, a dashed-line

box highlights an area where fine and tiny moiré fringes with a slightly curvy shape can be found; the moiré fringes are shown more clearly in a magnified image inset in the top right corner of Figure 10-3a. As demonstrated in Figure 10-3c, the formation of the moiré fringes can be attributed to the overlap of Si and Ge lattices in plan-view since the edge of the underlying Si substrate was not entirely etched in the ion milling process. Figure 10-3b shows that the moiré pattern can also be seen under 220 diffraction condition but are parallel to the <1$\bar{1}$0> direction as indicated by the black arrow in Figure 10-3b. On the contrary, the moiré fringes demonstrate a preferential orientation along the orthogonal <110> direction under 2$\bar{2}$0 diffraction condition. Furthermore, it should be noted that the straight fringes indicated by another black arrow in Figure 10-3b are likely to be caused by the film thickness variations and they are different from the curvy moiré pattern.

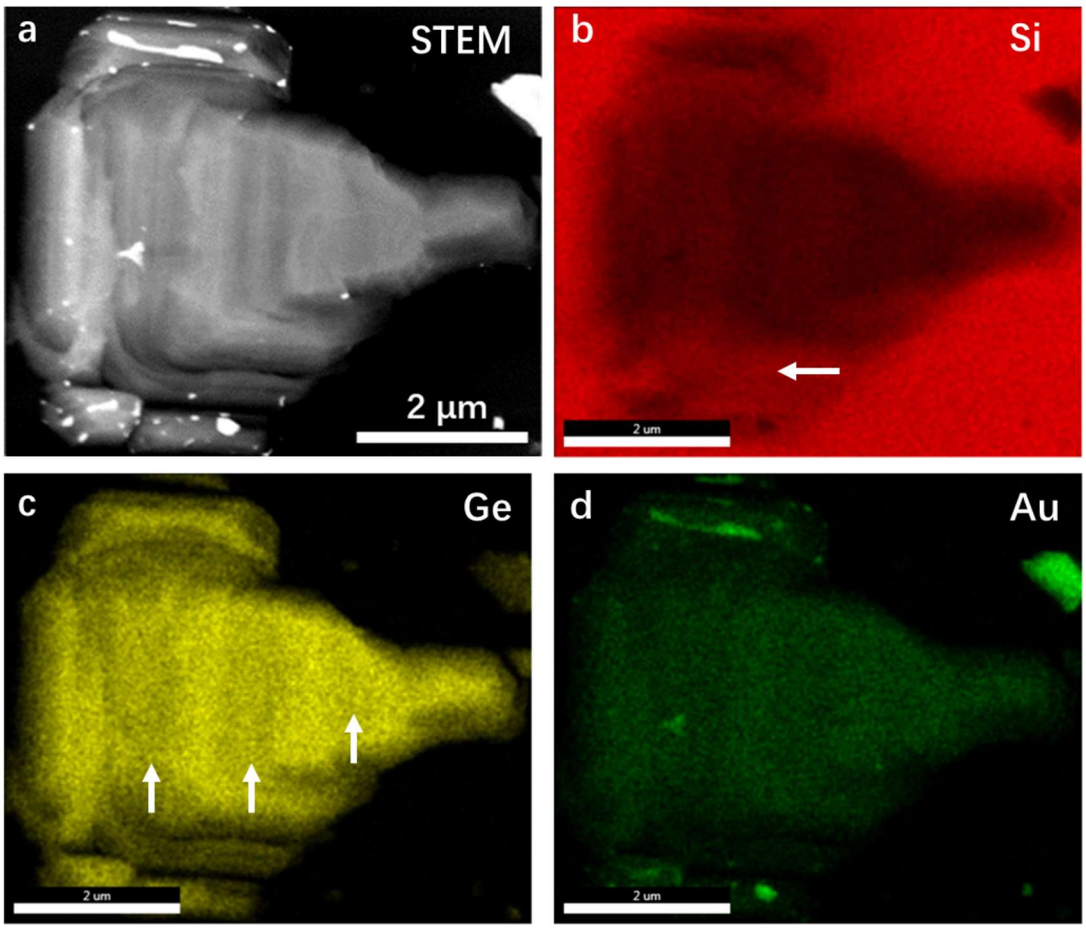

Figure 10-4. (a) Scanning transmission electron microscopy (STEM) image of the area shown in Figure 10-1a. (b-d) Energy-dispersive spectroscopy (EDS) mappings of elements Si, Ge, and Au, respectively.

Figures 10-4 b-d demonstrate the Energy-dispersive spectroscopy (EDS) maps of elements Si, Ge, and Au, within the film. These results must be interpreted carefully because the underlying Si substrate and the varying film thickness affects the elemental signals. As discussed above, it is thought that the Si substrate exists underneath areas with a moiré pattern (in general, the areas near the film's edge shown in Figure 10-3a). This theory is strengthened by the presence of areas showing high-intensity Si signals (indicated by the arrow in Figure 10-4b) in the Si map; most of these signals are likely to be collected from the Si substrate. However, we also observed slight Si intensity variations in the center of the film where no moiré pattern can be seen. This suggests composition variations in the center of the film since no signal from the Si substrate contributed to the intensity. Moreover, as highlight by the arrows in Figure 10-4c, the increased Si intensity areas in the Si EDS map correspond to the reduced Ge intensity areas in the Ge EDS map. It should be noted that we cannot determine whether the chemical composition is varied or not in these areas from solely the Si EDS map because the film thickness variations can lead to the same results. However, the opposite intensity variation trends from both the Si and Ge EDS maps, strongly suggested that the Si concentration is higher in these areas. The findings of the EDS maps correlate well with our earlier observations in AFM, which show the lower chemical etching rate in some local areas possibly due to higher Si content (Figure 10-2c).

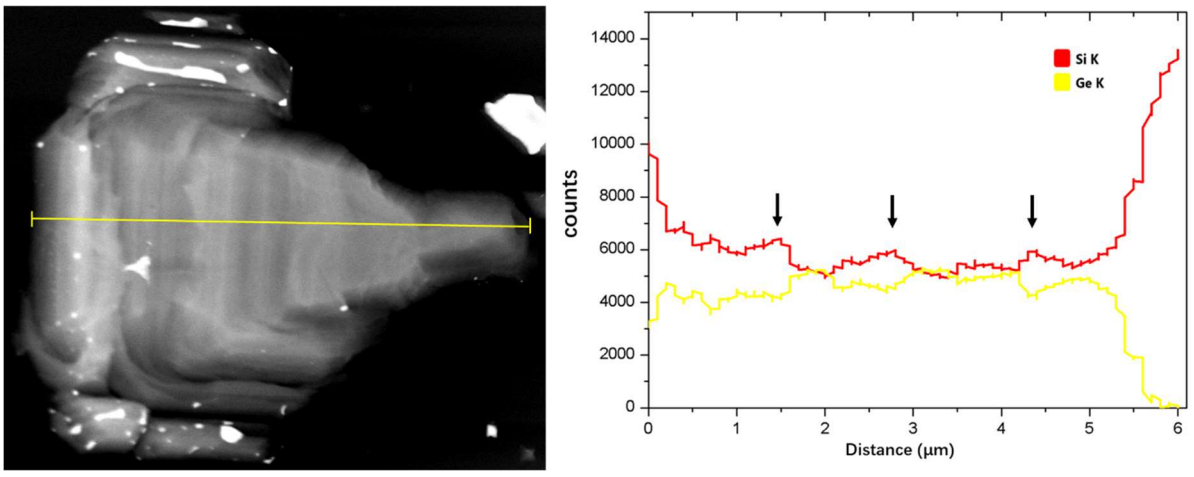

Figure 10-5. Plan-view TEM micrograph of the film (left) and EDS line scan (right) across the film along the yellow line in the left image. The arrows in the line scan indicate the Si count peaks.

The film composition can be further examined using the EDS line scan of the film in Figure 10-5 where three regions with Si content increased correspond to three reductions in Ge content.

It confirms our previous observations regarding the composition variations of the film. Additionally, the EDS line scan shows that the average Ge intensity along the line is slightly increasing from left to right, which can be attributed to the film thickness variations: the area near the edge (moiré pattern area) is thinner and the area in the center is thicker (Figure 10-3c).

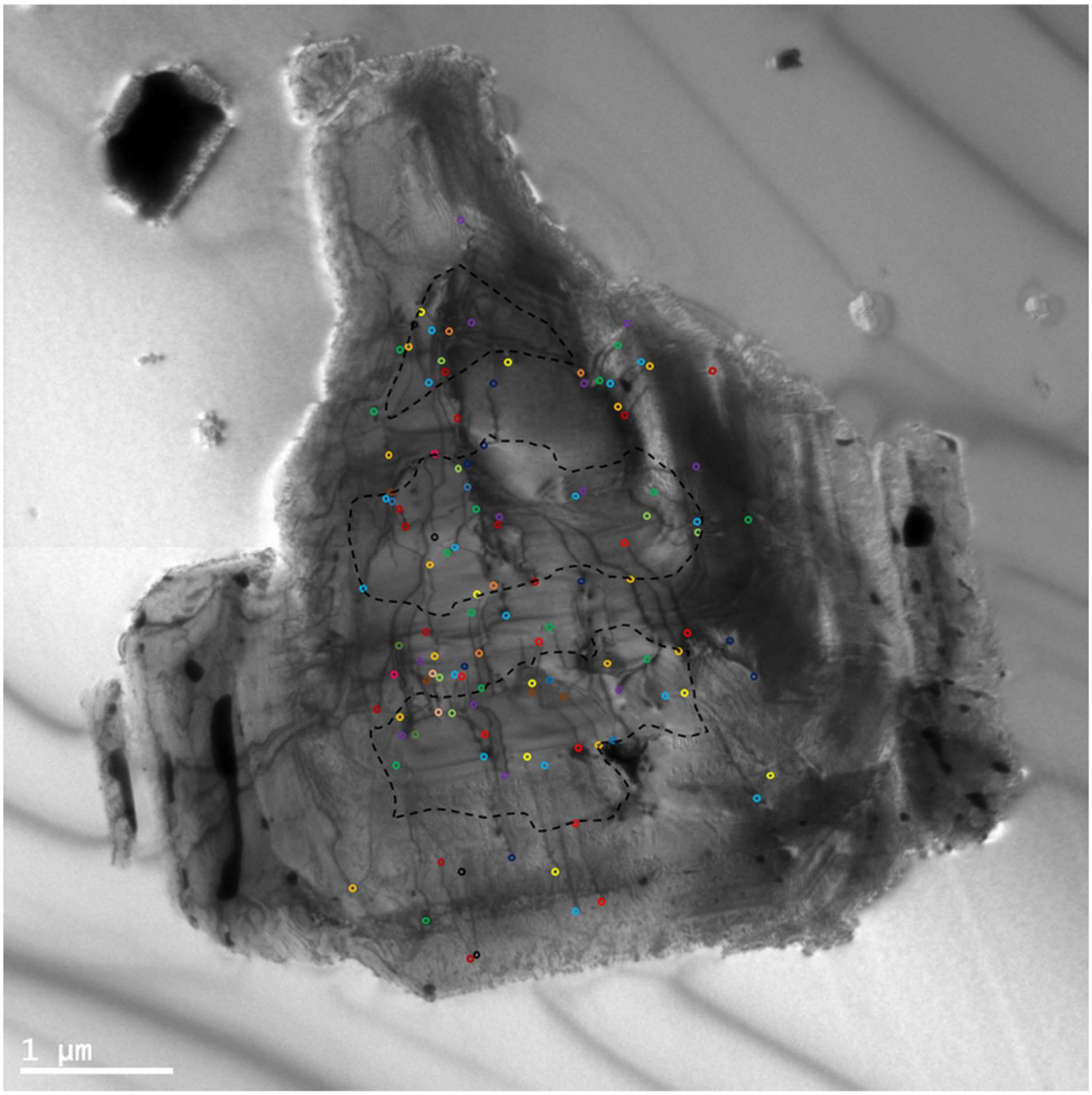

Figure 10-6. Different colored circles were used to denote the endpoints of the dislocations within the film shown in Figure 10-1a. In addition, three dashed-line areas highlight the Si-rich areas in the film based on the EDS mapping results.

In Figure 10-6, colored circles were used to denote the endpoints of the dislocations within the film to highlight the dislocation distribution. To simplify this study, every dislocation has two endpoints which are highlighted by the same color. One general observation is that the center

of the film has a higher dislocation density compared to the area near the film's edge. To help quantify this, the film was divided into 20 sections based on the distance from the geometrical center of the film to the edge of the film. As shown in Figure 10-7a, section #1 represents the smallest area which is in the center and section #20 represents the largest area at the most outer ring of the film. The other rings are labelled from the center to the edge of the film. In each section, we counted the number of the dislocations (1 dislocation endpoint signifies 0.5 dislocation) and plotted a dislocation density histogram in Figure 10-7b.

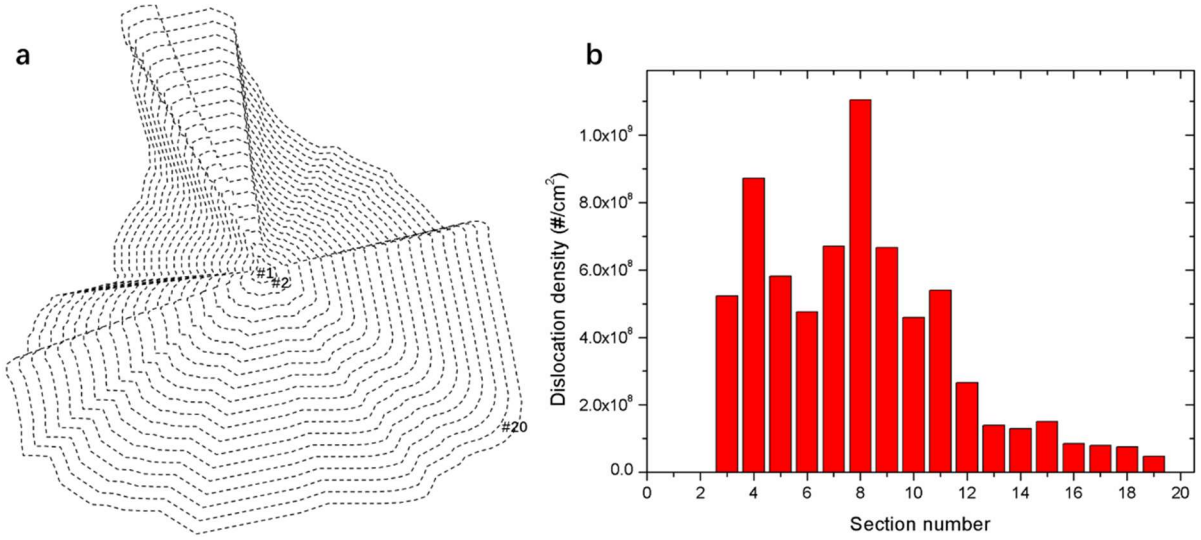

Figure 10-7. (a) The film shown in Figure 10-1a was uniformly divided into 20 sections based on the distance from the geometrical center to the edge of the film. (b) A histogram showing the dislocation density in each section.

As can be seen in Figure 10-7b, the dislocation density reached a peak in the section #8 (two magnitudes higher than that of the section #20) and decreased dramatically after the section number is larger than #12. To gain more insight into this observation, it is important to relate the dislocation distribution to the possible relaxation mechanisms discussed in chapter 9 that might occur to relieve the lattice-mismatched strain during the lateral growth process. At the beginning of the growth (nucleation), the lattice mismatch between Si and Ge is thought to be relaxed by the standard nucleation and glide of dislocations, which requires the generation of numerous threading dislocations. Once a first crystal nucleus was formed, the film could be grown laterally, and the strain might be relieved by the extension of the preexisting misfit dislocations or the nucleation of dislocations from the growth front. As a result, the generation of additional threading dislocations from the surface could be suppressed. Therefore, from the

view of relaxation mechanism, it is suggested that one or more first nucleation areas are located toward the center of the film and the other areas are the lateral overgrowth areas.

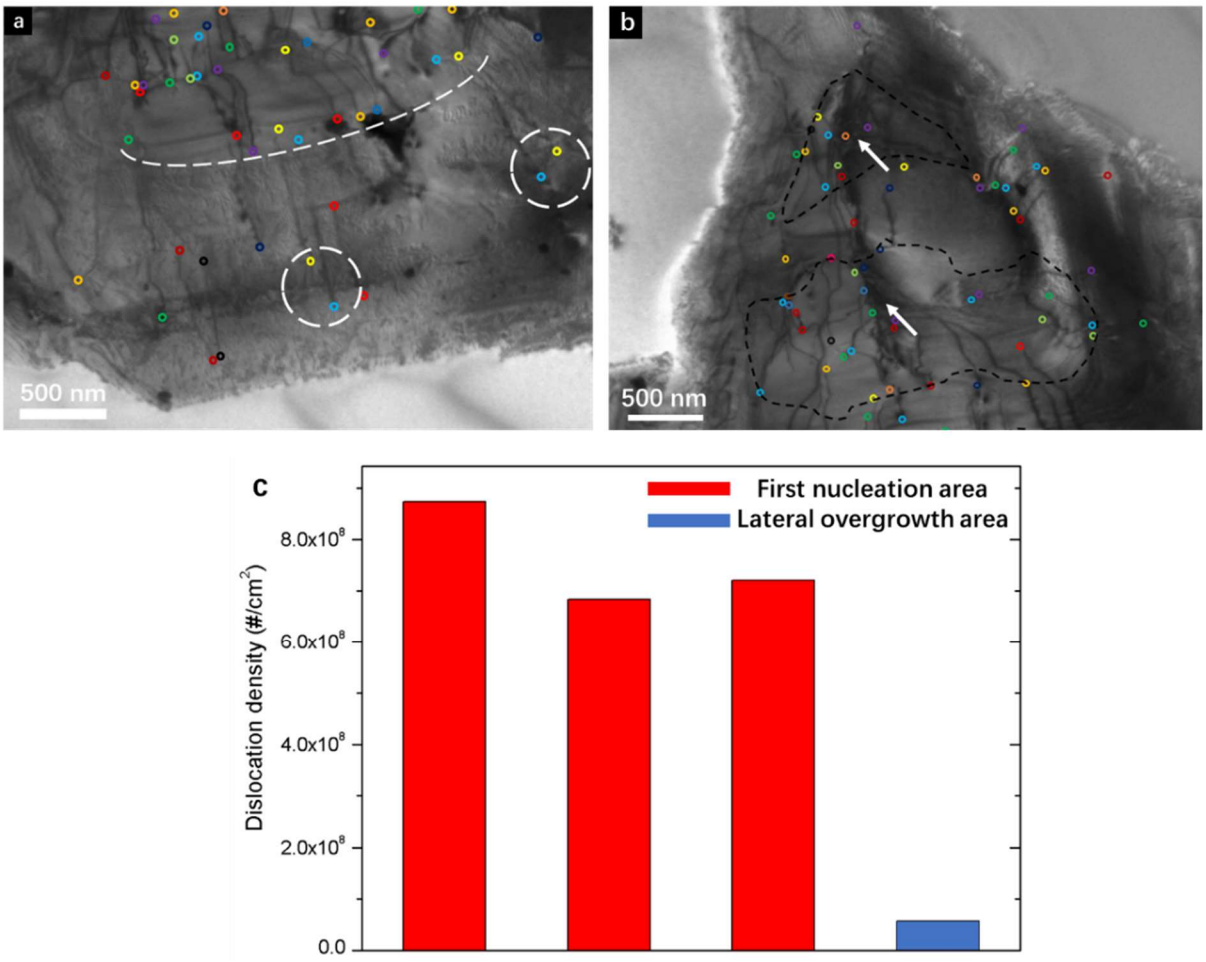

Figure 10-8. (a) and (b) Plan-view TEM micrographs showing how the dislocations glided to the film's edge and the dislocation plie-ups in the Si-rich areas. (c) Dislocation density histogram of the first growth areas and the lateral overgrowth area.

To further study the relationship between the dislocation density with the relaxation mechanism, we drew the approximate outlines of the Si-rich areas in Figure 10-6 based on the results from the Si EDS mapping. The determination of these Si-rich areas was further confirmed by several EDS line scans within the film (see Appendix B). These Si-rich areas are believed to be the first nucleation areas according to the report by Quitoriano[11] who found that for the metal-catalyzed, lateral growth of Ge nanowire on Si, Si was incorporated into the initial growth of the Ge nanowire. The reason for this is not clear but it may have something to with the Si component in the liquid. In the first nucleation process, it was likely that Ge and Si crystallized together to form the initial crystal nuclei because there was a certain amount of Si in the liquid

that could reach supersaturation. Afterwards, since the Si concentration in the liquid remained constant, there would be no driving force for the further crystallization of Si. Therefore, the subsequent film growth would be nearly pure Ge.

Importantly, it is found that a considerable number of dislocations originate from the Si-rich areas. As shown in Figure 10-8a, the curvy dashed-line reveals a narrow area inside a Si-rich area where a high-density dislocation of endpoints are found. In the same figure, the white circles indicated the endpoints at the other side of the dislocations showing how the dislocations gilded to the edge from the Si-rich, initial growth area. In Figure 10-8b, as shown by the arrows, dislocation pile-ups are found in the Si-rich areas possibly due to the interactions between dislocations, further supporting the existence of high-density threading dislocations in these Si rich-areas. Since many dislocations originated from the first-to-nucleate, Si-rich areas, we plotted the dislocation density histogram of the first growth areas and the lateral overgrowth area in Figure 10-8c. It was found that the dislocation density ($5.7\times 10^7/cm^2$) in the lateral overgrowth area is at least one order of magnitude lower than that of first-to-nucleate areas. It demonstrates the feasibility and potential of the lateral growth technique on growing high-quality, lattice-mismatched films on a substrate.

10.2. Conclusions

Chapter 10 provides a TEM study of the Ge(Si) film (Figure 10-1a) through an investigation on the morphology and composition of the film as well as the dislocations within the film. The Ge(Si) film was speculated to have thickness variations near the film's edge probably due to the rough Ge(Si)/Si interface. Such film thickness variations were visible as black straight lines in plan-view TEM. The existence of the rough Ge(Si)/Si interface was further confirmed by cross-sectional TEM and AFM. Moreover, the center of the film showed a brighter and uniform contrast in the HAADF image, suggesting that the center of the film is thicker with a more uniform thickness.

In chapter 10, the composition of the Ge(Si) films was preliminarily studied by using chemical

etching. It was found that a few spots within a Ge(Si) film had higher Si concentration since these areas were etched more slowly by a CrO_3-based etchant. More importantly, these Si-rich areas are probably the first-to-nucleate areas of the film as suggested by a previous Ge nanowire study. Then an EDS study was carried out to investigate on the composition of the film shown in Figure 10-1a in plan-view TEM and confirmed the existence of Si-rich areas. Based on the EDS results, the rough outlines of the Si-rich areas within the film were delineated in a diffraction-contrast TEM micrograph that highlights the dislocations. It is apparent from the micrograph that the Si-rich areas, which are probably the first-to-nucleate areas of the films, contain high-density of threading dislocations. In addition, these areas were found to be the nucleation sources for the lateral overgrowth areas. Most of the dislocations within the film originated from the Si-rich, first-to-nucleate areas; then these dislocations gilded to the film's edge and some of them were identified as 90° dislocations. On the other hand, the dislocation density in the lateral overgrowth area is at least one order of magnitude lower. The results in this chapter confirm the previous findings with respect to the reduction of defect density in the lateral overgrowth areas. Chapter 10, therefore, contributes additional evidence that the lateral growth technique is promising to grow high-quality, lattice-mismatched films.

Chapter 11

Conclusions and Future Work

11.1. Conclusions

The purpose of this thesis is to develop a metal-catalyzed, lateral epitaxial growth technique to grow high-quality, lattice-mismatched Ge films on Si. Initial nucleation of small Ge(Si) crystals on Si is the first step in the lateral growth process; the first-to-nucleate films are generally grown within the Au catalysts. This is followed by Ge(Si) film lateral overgrowths extended from these first-to-nucleate crystals and guided by the Au catalysts. In this thesis, it has been found that there are two major differences between the first-to-nucleate areas and the lateral overgrowth areas. First, within some micro-crucibles, the lateral overgrowth areas of the films

are thicker because the capping layers were deformed after the initial nucleation. Second, the first-to-nucleate areas have higher Si concentration compared to the lateral overgrowth areas because Si might also saturate the liquid in the first nucleation process. These two findings help us to identify where the first nucleation occurred in a Ge(Si) film; then the dislocation morphologies in the first-to-nucleate areas and the lateral overgrowth areas of the films were characterized by TEM. The TEM results show that the first-to-nucleate areas contain high density TDs while the lateral overgrowth areas demonstrate substantially reduced TDD or even defect-free areas. Moreover, most areas of the films (mainly the lateral overgrowth areas) are nearly fully relaxed and pure Ge as calculated from the film peak position in XRD. Additionally, there is a small peak between the film peak and the substrate peak in XRD, which is probably attributed to the presence of the Si-rich, first-to-nucleate areas of the films. What is surprising from the TEM and XRD results is that the laterally grown films are pure Ge films and fully relaxed on Si with low TDD.

To explain this result, a discussion should be provided from the view of relaxation mechanism. This thesis has argued that the initial film growth was vertical growth and might be relaxed by the nucleation of dislocation loops from the surface and the glide of dislocations, which is the traditional mechanism to relax planar Ge film grown on Si and introduces numerous additional TDs. In contrast, the laterally grown films might be relaxed by new relaxation mechanism since the lateral overgrowth areas of the films have lower TDD and are fully relaxed. We therefore proposed new relaxation mechanism that allows for high-quality, latticed-mismatched growth. We hypothesized that the strain induced by the lattice mismatch between Si and Ge can be relaxed by extending the preexisting misfit dislocations from the first-to-nucleate areas and that lateral growth can nucleate 90° dislocations in the growth front as it grows laterally. This study has demonstrated, for the first time, that the lateral epitaxial growth technique is promising to grow low TDD, lattice-mismatched films on substrates by using new relaxation mechanism.

The ideal way to laterally grow Ge film on Si is to nucleate single first Ge(Si) crystal within a Au catalyst and then laterally grow the film as large as possible. Note that multiple nucleation is not desired not only because the first-to-nucleate areas of the film contain high-density TDs

but also because multiple nucleation poses a challenge to control the growths. In general, a relatively low growth rate helps to realize single nucleation since it allows Ge atoms to diffuse the predefined growth sites before they crystallize in the liquid. Furthermore, a low growth rate can also suppress the uncatalyzed Ge growth on Si or capping layers; however, longer growth time is necessary to grow large films at low growth rate. As mentioned above, growing large-size films is important as well since device fabrication requires large defect-free surface. In this thesis, a model is proposed to predict the final film size within a micro-crucible by taking into account the size and shape of the Au catalyst. As suggested by the model, the Au catalyst should be designed to have a large vapor-liquid interface to absorb more Ge to enhance the film size. Besides, in order to grow a larger film, the Au catalyst should have a relatively small volume since Ge can saturate a smaller Au catalyst more rapidly. Nevertheless, it should be noted that a very small Au catalyst with a large vapor-liquid interface may lead to many nucleation points in the liquid, which is not desirable.

11.2. Future Work

The most interesting finding of this thesis is that there is a difference between the first-to-nucleate area and the lateral overgrowth area in terms of dislocation density and morphology. TDD was found to be largely reduced in the lateral overgrowth area, which means that this technique can be used to grow high-quality, lattice-mismatched film on a substrate. However, in order to use this technique in semiconductor industry, such lateral growth process must be well-controlled, for example, the engineering of the initial nucleation and the growth direction. Additionally, it is desirable to grow the films as large as possible to meet the broadest range of application requirements. Therefore, further research should be done to design a micro-crucible that can enable single, predefined first nucleation as well as unidirectional, large-size film growth. This will not be easy since large-size film growth requires a relatively high growth rate, and a high growth rate tends to result in multiple nucleation points and uncatalyzed growth.

Moreover, further work is required to develop the use of other metal catalysts since Au is well known as a deep level impurity in Ge[102], which is harmful for semiconductor devices. The other

material alternatives include indium (In), gallium (Ga), aluminum (Al), etc. It should be noted that In and Ga have poorer catalytic performance compared to Au, and the Al-Si eutectic temperature is quite high (577 ℃[103]) for Ge VLS growth, which can lead to large amounts of uncatalyzed growth. Since each catalyst has its own advantages and drawbacks, there is abundant room for further progress in determining the optimal metal catalyst.

Future studies on the effects of substrate orientation are recommended as well since Si (100) wafers are the only substrates used in this thesis. Therefore, it is of interest to grow Ge films laterally on Si wafer with a different orientation, e.g. Si (111), to compare results.

In addition, several questions in this thesis remain unanswered at present. Figure 9-4 provides the XRD results obtained from all the films on a substrate showing the global information with respect to the composition and relaxation of the films. It was found that most areas of the films are nearly fully relaxed and pure Ge. Nevertheless, the strain distributions in the Ge(Si) films are unknown (the composition distributions in the films can be roughly extracted from EDS mapping). Research questions that could be asked include whether the first-to-nucleate areas are fully relaxed or not? A further study with more focus on the relaxation and composition distributions in the films is therefore suggested, which requires a characterization instrument that has a high space resolution, e.g., scanning X-ray diffraction microscopy[104]. Such study can provide more information for us to fully understand the lateral growth process. Besides, even though we hypothesized two relaxation mechanisms to explain the observed reduction of TDD, more research on film's relaxation needs to be undertaken before the growth process is more clearly understood.

Appendix A – Equation 2 in chapter 8

For the micro-crucibles studied in chapter 8, they have a triangular shape before annealing. However, during annealing Au agglomerated on Si which changed the catalyst shape (as shown below).

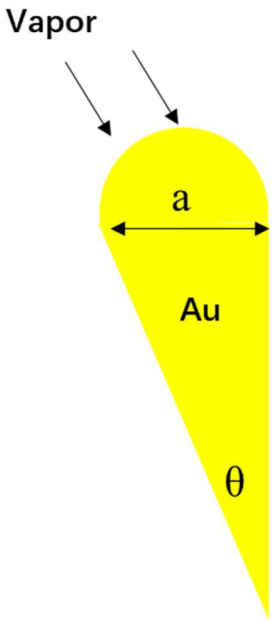

The area of liquid-vapor interface: $A_{Liquid-Vapor} = \frac{1}{2}\pi ah$

The volume of Au: $V_{Au} = (\frac{1}{2tan\theta} + \frac{1}{8}\pi) \cdot a^2 h$

$$A_{Liquid-Vapor} = \frac{\pi}{2}\sqrt{(1/(\frac{1}{2tan\theta} + \frac{1}{8}\pi) \cdot \sqrt{h} \cdot \sqrt{V_{Au}}}$$

h is Au or film thickness.

Appendix B – EDS line scans across the film shown in Figure 10-1a

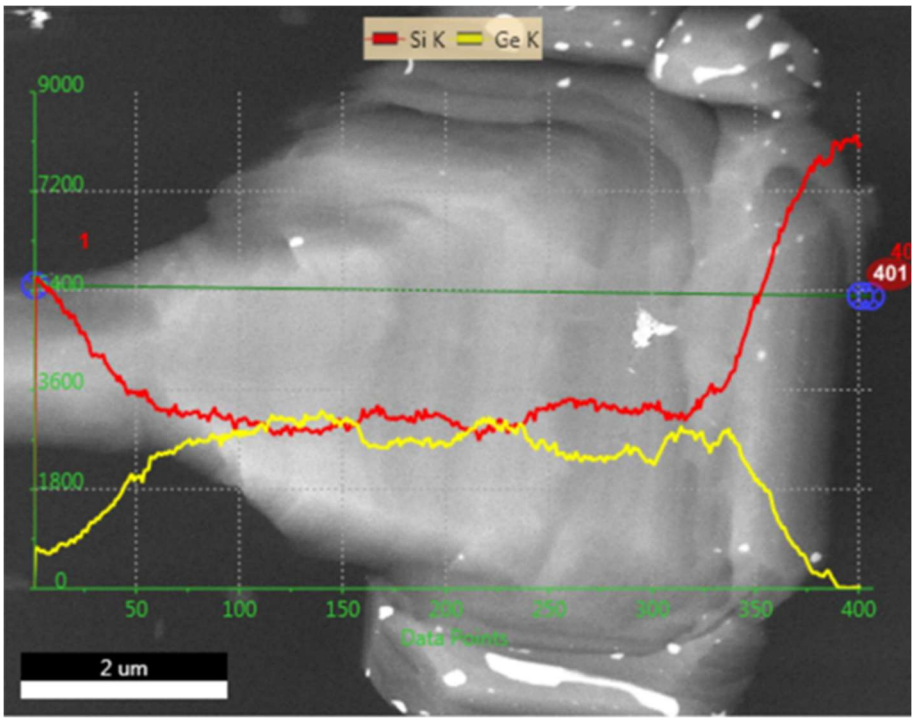

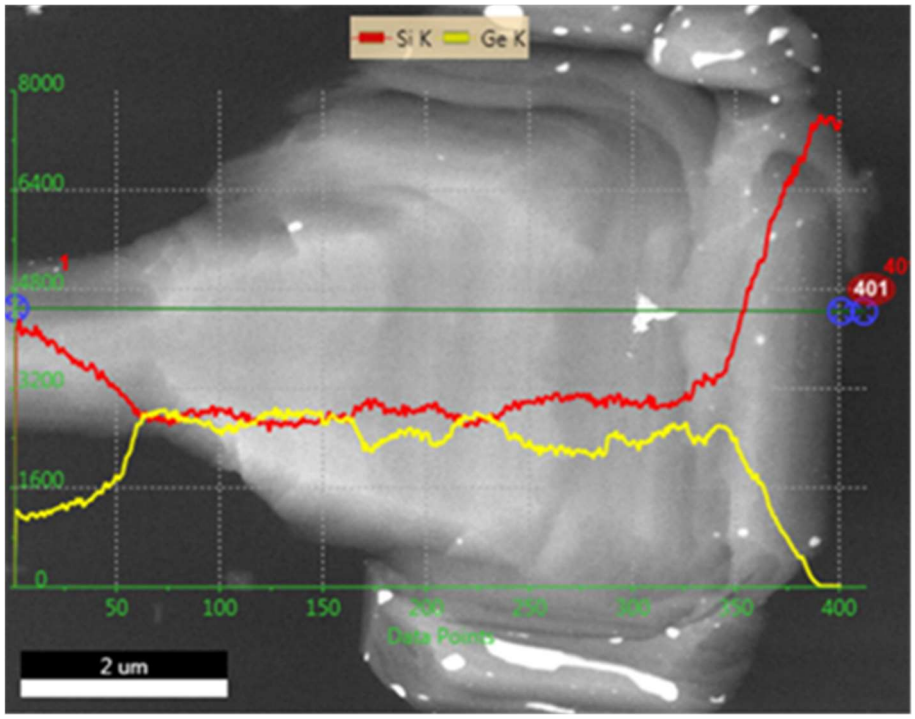

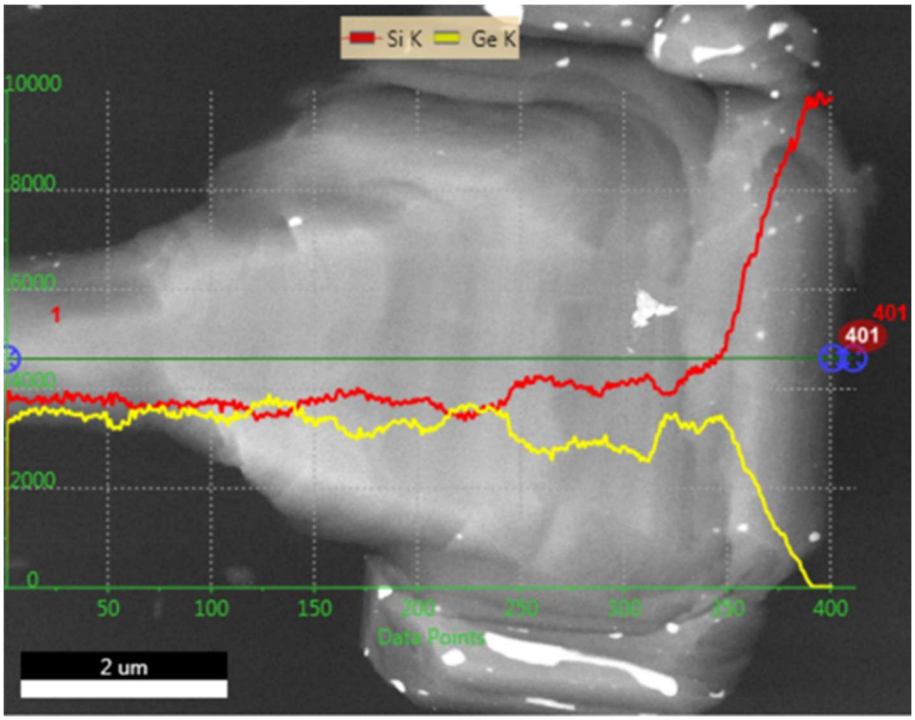
Si K
Ge K
10000
8000
6000
4000
2000
0
1
401
401
50
100
150
200
250
300
350
400
Data Points
2 um

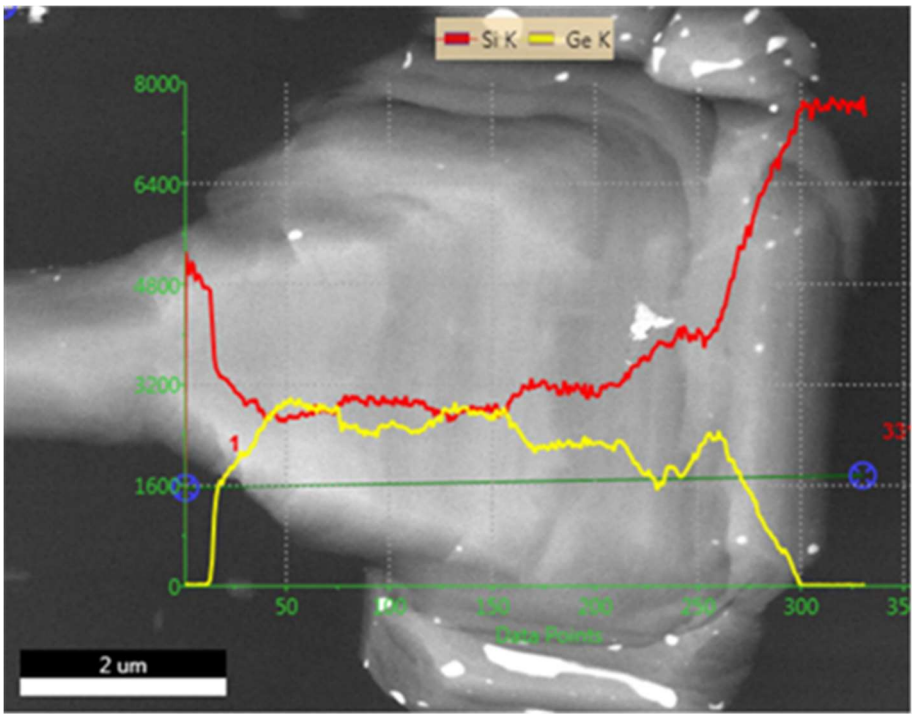
Si K
Ge K
8000
6400
4800
3200
1600
0
1
50
150
300
Data Points
2 um

References

1. King, R. R., Law, D. C., Edmondson, K. M., Fetzer, C. M., Kinsey, G. S., & Yoon, H., et al. (2007). 40% efficient metamorphic GaInp⁄GaInAs⁄Ge multijunction solar cells. *Applied Physics Letters, 90*(18), 510.

2. Ahn, J. H., Kim, H. S., Lee, K. J., Jeon, S., Kang, S. J., & Sun, Y., et al. (2006). Heterogeneous three-dimensional electronics by use of printed semiconductor nanomaterials. *Science, 314*(5806), 1754-1757.

3. Xiang, J., Lu, W., Hu, Y., Wu, Y., Yan, H., & Lieber, C. M. (2006). Xiang, j. et al. ge/si nanowire heterostructures as high-performance field-effect transistors. nature 441, 489-493. *Nature, 441*(7092), 489-93.

4. Michel, J., Liu, J., & Kimerling, L. C. (2000). High-performance Ge-on-Si photodetectors. *Nature Photonics, 4*(8), 527-534.

5. Fitzgerald, E. A. (1991). Dislocations in strained-layer epitaxy: theory, experiment, and applications. Materials Science Reports, 7(3), 87-142.

6. Roelkens, G., Brouckaert, J., Taillaert, D., Dumon, P., Bogaerts, W., & Van, T. D., et al. (2005). Integration of Inp/InGaAsp photodetectors onto silicon-on-insulator waveguide circuits. *Optics Express, 13*(25), 10102-8.

7. Currie, M. T., Samavedam, S. B., Langdo, T. A., Leitz, C. W., & Fitzgerald, E. A. (1998). Controlling threading dislocation densities in Ge on Si using graded SiGe layers and chemical-mechanical polishing. *Applied Physics Letters, 72*(14), 1718-1720.

8. Luan, H. C., Lim, D. R., Lee, K. K., Chen, K. M., Sandland, J. G., & Wada, K., et al. (1999). High-quality Ge epilayers on Si with low threading-dislocation densities. *Applied Physics Letters, 75*(19), 2909-2911.

9. Park, J. S., Bai, J., Curtin, M., Adekore, B., Cheng, Z., & Carroll, M., et al. (2007). Defect reduction and its mechanism of selective Ge epitaxy in trenches on Si(001) substrates using aspect ratio trapping. *Applied Physics Letters, 90*(5), 3344.

10. Quitoriano, N. J., & Kamins, T. I. (2008). Integratable nanowire transistors. *Nano Letters, 8*(12), 4410.

11. Quitoriano, N. J., Wu, W., & Kamins, T. I. (2009). Guiding vapor-liquid-solid nanowire growth using SiO_2. *Nanotechnology, 20*(14), 145303.

12. Quitoriano, N. J. (2010). Lateral, high-quality, metal-catalyzed semiconductor growth on amorphous and lattice-mismatched substrates for photovoltaics. *Applied Physics Letters, 97*(13), 123505-2792.

13. Plummer, J. D. (2009). *Silicon VLSI technology: fundamentals, practice and modeling.* Pearson Education India.

14. Meindl, J. D., Chen, Q., & Davis, J. A. (2001). Limits on silicon nanoelectronics for terascale integration. *Science*, 293(5537), 2044-2049.

15. Saraswat, K., Chui, C. O., Krishnamohan, T., Kim, D., Nayfeh, A., & Pethe, A. (2006). High performance germanium MOSFETs. *Materials Science and Engineering: B*, 135(3), 242-249.

16. Schaller, R. R. (1997). Moore's law: past, present and future. *IEEE spectrum*, 34(6), 52-59.

17. Green, M. A. (2006). *Third generation photovoltaics: advanced solar energy conversion* (Vol. 12). Springer Science & Business Media.

18. Petrova-Koch, V., Hezel, R., & Goetzberger, A. (Eds.). (2008). *High-efficient low-cost photovoltaics: recent developments* (Vol. 140). Springer.

19. Lewis, N. S. (2007). Toward cost-effective solar energy use. *science*, 315(5813), 798-801.

20. Saraswat, K. C., Chui, C. O., Krishnamohan, T., Nayfeh, A., & McIntyre, P. (2005). Ge based high performance nanoscale MOSFETs. *Microelectronic Engineering*, 80, 15-21.

21. Kamata, Y. (2008). High-k/Ge MOSFETs for future nanoelectronics. *Materials today*, 11(1), 30-38.

22. Michel, J., Liu, J., & Kimerling, L. C. (2010). High-performance Ge-on-Si photodetectors. *Nature Photonics*, 4(8), 527-534.

23. Beals, M., Michel, J., Liu, J. F., Ahn, D. H., Sparacin, D., Sun, R., ... & Beattie, J. (2008, February). *Process flow innovations for photonic device integration in CMOS*. In Silicon Photonics III (Vol. 6898, p. 689804). International Society for Optics and Photonics.

24. Ahn, D., Hong, C. Y., Liu, J., Giziewicz, W., Beals, M., Kimerling, L. C., ... & Kärtner, F. X. (2007). High performance, waveguide integrated Ge photodetectors. *Optics express*, 15(7), 3916-3921.

25. McEvoy, A. J., Castaner, L., & Markvart, T. (2012). *Solar cells: materials, manufacture and operation*. Academic Press.

26. Soref, R. (2010). Silicon photonics: a review of recent literature. *Silicon*, 2(1), 1-6.

27. Chen, X., Huo, Y., Cho, S., Park, B. G., & Harris, J. S. (2014). Surface Treatment of Ge Grown Epitaxially on Si by Ex-Situ Annealing for Optical Computing by Ge Technology. *IEIE Transactions on Smart Processing & Computing*, 3(5), 331-337.

28. Deen, M. J., & Basu, P. K. (2012). *Silicon Photonics: Fundamentals and Devices* (p. 454). New York, NY, USA:: Wiley.

29. Ahn, D., Hong, C. Y., Liu, J., Giziewicz, W., Beals, M., Kimerling, L. C., ... & Kärtner, F. X. (2007). High performance, waveguide integrated Ge photodetectors. *Optics express*, 15(7), 3916-3921.

30. Keiser, G. (2003). *Optical fiber communications*. John Wiley & Sons, Inc..

31. Held, G. (2016). *Introduction to light emitting diode technology and applications*. CRC press.

32. Chaisakul, P., Marris-Morini, D., Frigerio, J., Chrastina, D., Rouifed, M. S., Cecchi, S., ... & Vivien, L. (2014). Integrated germanium optical interconnects on silicon substrates. *Nature Photonics*, 8(6), 482.

33. Assefa, S., Xia, F., & Vlasov, Y. A. (2010). Reinventing germanium avalanche photodetector for nanophotonic on-chip optical interconnects. *Nature*, 464(7285), 80.

34. Hagen, W., & Strunk, H. (1978). A new type of source generating misfit dislocations. *Applied physics*, 17(1), 85-87.

35. Matthews, J. W., Blakeslee, A. E., & Mader, S. (1976). Use of misfit strain to remove dislocations from epitaxial thin films. *Thin Solid Films*, 33(2), 253-266.

36. People, R., & Bean, J. C. (1985). Calculation of critical layer thickness versus lattice mismatch for $Ge_x Si_{1-x}$/Si strained-layer heterostructures. *Applied Physics Letters*, 47(3), 322-324.

37. Fitzgerald, E. A. (1989). The effect of substrate growth area on misfit and threading dislocation densities in mismatched heterostructures. *Journal of Vacuum Science & Technology B*, 7(4), 782-788.

38. Andre, C. L., D. M. Wilt, A. Pitera, M. L. Lee, E. A. Fitzgerald, & S. A. Ringel. (2005) Impact of dislocation densities on n+/p and p+/n junction GaAs diodes and solar cells on SiGe virtual substrates. *Journal of applied physics* 98(1), 014502-014502-5.

39. Nayfeh, A., Chui, C. O., Saraswat, K. C., & Yonehara, T. (2004). Effects of hydrogen annealing on heteroepitaxial-Ge layers on Si: Surface roughness and electrical quality. *Applied physics letters*, 85(14), 2815-2817.

40. Eaglesham, D. J., & Cerullo, M. (1990). Dislocation-free stranski-krastanow growth of Ge on Si (100). *Physical review letters*, 64(16), 1943.

41. Ross, F. M., Tromp, R. M., & Reuter, M. C. (1999). Transition states between pyramids and domes during Ge/Si island growth. *Science*, 286(5446), 1931-1934.

42. Mo, Y. W., Savage, D. E., Swartzentruber, B. S., & Lagally, M. G. (1990). Kinetic pathway in Stranski-Krastanov growth of Ge on Si (001). *Physical Review Letters*, 65(8), 1020.

43. Colace, L., Masini, G., Galluzzi, F., Assanto, G., Capellini, G., Di Gaspare, L., & Evangelisti, F. (1997). Ge/Si (001) photodetector for near infrared light. *Solid State Phenomena*, 54, 55-58.

44. Shah, V. A., Dobbie, A., Myronov, M., & Leadley, D. R. (2011). Effect of layer thickness on structural quality of Ge epilayers grown directly on Si (001). *Thin Solid Films*, 519(22), 7911-7917.

45. Larsen, A. N. (2006). Epitaxial growth of Ge and SiGe on Si substrates. *Materials Science in Semiconductor Processing, 9*(4), 454-459.

46. Choi, D., Ge, Y., Harris, J. S., Cagnon, J., & Stemmer, S. (2008). Low surface roughness and threading dislocation density Ge growth on Si (001). *Journal of Crystal Growth*, 310(18), 4273-4279.

47. Terzieva, V., Souriau, L., Caymax, M., Brunco, D. P., Moussa, A., Van Elshocht, S., ... & Meuris, M. (2008). Benefits and side effects of high temperature anneal used to reduce threading dislocation defects in epitaxial Ge layers on Si substrates. *Thin Solid Films*, 517(1), 172-177.

48. Lee, M. L., Fitzgerald, E. A., Bulsara, M. T., Currie, M. T., & Lochtefeld, A. (2005). Strained Si, SiGe, and Ge channels for high-mobility metal-oxide-semiconductor field-effect transistors. *Journal of Applied Physics*, 97(1), 1.

49. Samavedam, S. B., Currie, M. T., Langdo, T. A., & Fitzgerald, E. A. (1998). High-quality germanium photodiodes integrated on silicon substrates using optimized relaxed graded buffers. *Applied physics letters*, 73(15), 2125-2127.

50. Chen, H., Guo, L. W., Cui, Q., Hu, Q., Huang, Q., & Zhou, J. M. (1996). Low-temperature buffer layer for growth of a low-dislocation-density SiGe layer on Si by molecular-beam epitaxy. *Journal of applied physics*, 79(2), 1167-1169.

51. Langdo, T. A., Leitz, C. W., Currie, M. T., Fitzgerald, E. A., Lochtefeld, A., & Antoniadis, D. A. (2000). High quality Ge on Si by epitaxial necking. *Applied Physics Letters*, 76(25), 3700-3702.

52. Bai, J., Park, J. S., Cheng, Z., Curtin, M., Adekore, B., Carroll, M., ... & Dudley, M. (2007). Study of the defect elimination mechanisms in aspect ratio trapping Ge growth. *Applied Physics Letters*, 90(10), 101902.

53. Yu, H. Y., Ishibashi, M., Park, J. H., Kobayashi, M., & Saraswat, K. C. (2009). p-Channel Ge MOSFET by selectively heteroepitaxially grown Ge on Si. *Electron Device Letters*, IEEE, 30(6), 675-677.

54. Yu, H. Y., Cheng, S. L., Park, J. H., Okyay, A. K., Onbaşlı, M. C., Ercan, B., ... & Saraswat, K. C. (2010). High quality single-crystal germanium-on-insulator on bulk Si substrates based on multistep lateral over-growth with hydrogen annealing. *Applied Physics Letters*, 97(6), 063503.

55. Yu, H. Y., Park, J. H., Okyay, A. K., & Saraswat, K. C. (2012). Selective-Area High-Quality Germanium Growth for Monolithic Integrated Optoelectronics. *Electron Device Letters*, IEEE, 33(4), 579-581.

56. Tsaur, B. Y., McClelland, R. W., Fan, J. C., Gale, R. P., Salerno, J. P., Vojak, B. A., & Bozler, C. O. (1982). Low-dislocation-density GaAs epilayers grown on Ge-coated Si substrates by means of lateral epitaxial overgrowth. *Applied Physics Letters*, 41(4), 347-349.

57. LeBoeuf, J. L., & Quitoriano, N. J. (2014). Nucleation and solidification of laterally grown silicon micro-films on amorphous substrates using the VLS mechanism. *Journal of Crystal Growth*, 391, 1-6.

58. Wagner, R. S., & Ellis, W. C. (1964). Vapor-liquid-solid mechanism of single crystal growth. *Applied Physics Letters*, 89-90.

59. Jones, A. C., & Hitchman, M. L. (2008). Overview of chemical vapour deposition. *Chemical Vapour Deposition: Precursors, Processes and Applications*, 1-36.

60. Barns, R. L., & Ellis, W. C. (1965). Whisker crystals of gallium arsenide and gallium phosphide grown by the vapor—liquid—solid mechanism. *Journal of Applied Physics*, 36(7), 2296-2301.

61. Wagner, R. S. (1967). Defects in silicon crystals grown by the VLS technique. *Journal of Applied Physics*, 38(4), 1554-1560.

62. Wagner, R. S. "VLS mechanism of crystal growth." *Whisker Technology* (1970): 47-119.

63. Kawano, T., Kato, Y., Futagawa, M., Takao, H., Sawada, K., & Ishida, M. (2002). Fabrication and properties of ultrasmall Si wire arrays with circuits by vapor–liquid–solid growth. *Sensors and Actuators A: Physical*, 97, 709-715.

64. Bootsma, G. A., & Gassen, H. J. (1971). A quantitative study on the growth of silicon whiskers from silane and germanium whiskers from germane. *Journal of Crystal Growth,* 10(3), 223-234.

65. Givargizov, E. I. (1975). Fundamental aspects of VLS growth. *Journal of Crystal Growth*, 31, 20-30.

66. Givargizov, E. I., & Chernov, A. (1973). Rate of whisker growth by the vapor-liquid-crystal mechanism and the role of surface energy. *Sov. Phys. Cryst.*, 18(1), 89-92.

67. Nebol'sin, V. A., Shchetinin, A. A., Dolgachev, A. A., & Korneeva, V. V. (2005). Effect of the nature of the metal solvent on the vapor-liquid-solid growth rate of silicon whiskers. *Inorganic materials*, 41(12), 1256-1259.

68. Kodambaka, S., Tersoff, J., Reuter, M. C., & Ross, F. M. (2006). Diameter-independent kinetics in the vapor-liquid-solid growth of Si nanowires. *Physical review letters*, 96(9), 096105.

69. Pinion, C. W., Nenon, D. P., Christesen, J. D., & Cahoon, J. F. (2014). Identifying Crystallization-and Incorporation-Limited Regimes during Vapor–Liquid–Solid Growth of Si Nanowires. *ACS nano*, 8(6), 6081-6088.

70. Ross, F. M. (2010). Controlling nanowire structures through real time growth studies. *Reports on Progress in Physics*, 73(11), 114501.

71. Kim, B. J., Tersoff, J., Kodambaka, S., Reuter, M. C., Stach, E. A., & Ross, F. M. (2008). Kinetics of individual nucleation events observed in nanoscale vapor-liquid-solid growth. *Science*, 322(5904), 1070-1073.

72. Kim, B. J., Wen, C. Y., Tersoff, J., Reuter, M. C., Stach, E. A., & Ross, F. M. (2012). Growth pathways in ultralow temperature Ge nucleation from Au. *Nano letters*, 12(11), 5867-5872.

73. Kalache, B., i Cabarrocas, P. R., & i Morral, A. F. (2006). Observation of incubation times in the nucleation of silicon nanowires obtained by the vapor–liquid–solid method. *Japanese journal of applied physics*, 45(2L), L190.

74. Schmidt, V., Wittemann, J. V., & Gosele, U. (2010). Growth, thermodynamics, and electrical properties of silicon nanowires†. *Chemical reviews*, 110(1), 361-388.

75. Wang, D., & Dai, H. (2002). Low-Temperature Synthesis of Single-Crystal Germanium Nanowires by Chemical Vapor Deposition. *Angewandte Chemie*, 114(24), 4977-4980.

76. Park, H. D., Gaillot, A. C., Prokes, S. M., & Cammarata, R. C. (2006). Observation of size dependent liquidus depression in the growth of InAs nanowires. *Journal of crystal growth*, 296(2), 159-164.

77. Kamins, T. I., Stanley Williams, R., Basile, D. P., Hesjedal, T., & Harris, J. S. (2001). Ti-catalyzed Si nanowires by chemical vapor deposition: Microscopy and growth mechanisms. *Journal of Applied Physics*, 89(2), 1008-1016.

78. Kodambaka, S. R. M. C., Tersoff, J., Reuter, M. C., & Ross, F. M. (2007). Germanium nanowire growth below the eutectic temperature. *Science*, 316(5825), 729-732.

79. Kamins, T. I., Li, X., Williams, R. S., & Liu, X. (2004). Growth and structure of chemically vapor deposited Ge nanowires on Si substrates. *Nano Letters*, 4(3), 503-506.

80. Cho, H. S., & Kamins, T. I. (2010). In situ control of Au-catalyzed chemical vapor deposited (CVD) Ge nanocone morphology by growth temperature variation. *Journal of Crystal Growth*, 312(16), 2494-2497.

81. Taraci, J. L., Dailey, J. W., Clement, T., Smith, D., Drucker, J., & Picraux, S. T. (2004). Nanopillar growth mode by vapor-liquid-solid epitaxy. *Applied physics letters*, 84(26), 5302-5304.

82. Dailey, J. W., Taraci, J., Clement, T., Smith, D., Drucker, J., & Picraux, S. T. (2004). Vapor-liquid-solid growth of germanium nanostructures on silicon. *Journal of applied physics*, 96(12), 7556-7567.

83. Adhikari, H., Marshall, A. F., Chidsey, C. E., & McIntyre, P. C. (2006). Germanium nanowire epitaxy: Shape and orientation control. *Nano letters*, 6(2), 318-323.

84. Biswas, S., Singha, A., Morris, M. A., & Holmes, J. D. (2012). Inherent Control of Growth, Morphology, and Defect Formation in Germanium Nanowires. *Nano letters*, 12(11), 5654-5663.

85. Lew, K. K., & Redwing, J. M. (2003). Growth characteristics of silicon nanowires synthesized by vapor–liquid–solid growth in nanoporous alumina templates. *Journal of Crystal Growth*, 254(1), 14-22.

86. Buttard, D., David, T., Gentile, P., Dhalluin, F., & Baron, T. (2009). High-density guided growth of silicon nanowires in nanoporous alumina on Si (100) substrate: Estimation of activation energy. *physica status solidi (RRL)-Rapid Research Letters*, 3(1), 19-21.

87. Lecestre, A., Dubois, E., Villaret, A., Coronel, P., Skotnicki, T., Delille, D., ... & Troadec, D. (2009,

November). *Confined and guided catalytic growth of crystalline silicon films on a dielectric substrate*. In IOP Conference Series: Materials Science and Engineering (Vol. 6, No. 1, p. 012022). IOP Publishing.

88. Pevzner, A., Engel, Y., Elnathan, R., Tsukernik, A., Barkay, Z., & Patolsky, F. (2011). Confinement-guided shaping of semiconductor nanowires and nanoribbons:"Writing with nanowires". *Nano letters*, 12(1), 7-12.

89. LeBoeuf, J. L., Brodusch, N., Gauvin, R., & Quitoriano, N. J. (2014). Preferred orientations of laterally grown silicon films over amorphous substrates using the vapor–liquid–solid technique. *Journal of Applied Physics*, 116(24), 244308.

90. Cammilleri, V. D., Yam, V., Fossard, F., Renard, C., Bouchier, D., Fazzini, P. F., & Hÿtch, M. (2009). Growth kinetics of Ge crystals on silicon oxide by nanoscale silicon seed induced lateral epitaxy. *Journal of Applied Physics*, 106(9), 093512.

91. Cammilleri, V. D., Yam, V., Fossard, F., Renard, C., Bouchier, D., Fazzini, P. F., ... & Hÿtch, M. (2008). Lateral epitaxial growth of germanium on silicon oxide. *Applied Physics Letters*, 93(4), 043110.

92. McComber, K. A., Duan, X., Liu, J., Michel, J., & Kimerling, L. C. (2012). Single-Crystal Germanium Growth on Amorphous Silicon. *Advanced Functional Materials*, 22(5), 1049-1057.

93. Sadoh, T., Kurosawa, M., Toko, K., & Miyao, M. (2014). Coherent lateral-growth of Ge over insulating film by rapid-melting-crystallization. *Thin Solid Films*, 557, 135-138.

94. Yougui Liao, *Dependence of Emission Coefficient of Secondary Electrons on Atomic Number and Accelerating Voltage of Incident Beam*. Available from: http://www.globalsino.com/EM/page4803.html

95. Williams, D. B., & Carter, C. B. (2009). *The Transmission electron microscope*. In Transmission Electron Microscopy (pp. 3-22). Springer US.

96. Fultz, B., & Howe, J. M. (2007). *Transmission electron microscopy and diffractometry of materials*. Springer Science & Business Media.

97. Marchionna, S., Virtuani, A., Acciarri, M., Isella, G., & Kaenel, H. V. (2006). Defect imaging of SiGe strain relaxed buffers grown by LEPECVD. *Materials science in semiconductor processing*, 9.4-5: 802-805.

98. Leboeuf, J. L., Brodusch, N., Gauvin, R., & Quitoriano, N. J. (2014). Low-temperature, vapor-liquid-solid, laterally grown silicon films using alloyed catalysts. *Materials Research Express, 1*(4), 046411.
.

99. Langdo, Thomas Andrew. Selective SiGe Nanostructures. Diss. Massachusetts Institute of Technology, 2001.

100. Chen, Y., & Washburn, J. (1996). Structural transition in large-lattice-mismatch heteroepitaxy. *Physical Review Letters, 77*(19), 4046.

101. Quitoriano, N. J., & Fitzgerald, E. A. (2007). Alternative slip system activation in lattice-mismatched InP/InGaAs interfaces. *Journal of applied physics*, 101(7), 073509.

102. Tyler, W. W. (1959). Deep level impurities in germanium. *Journal of Physics and Chemistry of Solids*, 8, 59-65.

103. Wang, Y., Schmidt, V., Senz, S., & Gösele, U. (2006). Epitaxial growth of silicon nanowires using an aluminium catalyst. *Nature nanotechnology*, 1(3), 186.

104. Zoellner, M. H., Richard, M. I., Chahine, G. A., Zaumseil, P., Reich, C., Capellini, G., ... & Häberlen,

M. (2015). Imaging structure and composition homogeneity of 300 mm SiGe virtual substrates for advanced CMOS applications by scanning X-ray diffraction microscopy. *ACS applied materials & interfaces*, 7(17), 9031-9037.